



School of
Mineral
Resources
Engineering

Technical University of Crete

POST-GRADUATE PROGRAMME GEOTECHNOLOGY AND ENVIRONMENT

THESIS SUBMITTED FOR THE DEGREE MASTER OF SCIENCE

<<Diagenesis of phyllosilicates in the sedimentary Fe-Ni deposits of Central Euboea,
Greece and mobilization of critical metals>>

SPYRIDON CHELIOTIS-CHATZIDIMITRIOU

2019029004

schatzidimitriou@isc.tuc.gr

SUPERVISOR: GEORGIOS E. CHRISTIDIS PROFESSOR, TUC

EXAMINATION COMITEE

GEORGIOS E. CHRISTIDIS PROFESSOR, TUC, School of Mineral Resources
Engineering

IOANNIS MARANTOS, Hellenic Survey of Geology and Mineral Exploration

LAURENT CANER, Université de Poitiers, Institut de Chimie des Milieux et Matériaux de
Poitier

Abstract

The sedimentary Fe-Ni deposits of Central Euboea were formed from lateritic weathering of ultrabasic-basic rocks of Jurassic ophiolites. After the formation of lateritic mantles, followed erosion, transportation and deposition in shallow marine/lagoonal environment in the Upper Cretaceous, over Triassic limestones or ophiolites or rarely, chert-schist stones. The deposits have been studied extensively in the past and their mineralogy has been relatively well established regarding the ore minerals and the hosts of Ni. Therefore, it is widely accepted that the main hosts of Ni are phyllosilicates, mainly chlorite, serpentine and talc, whereas Fe-oxides and Fe-oxyhydroxides are of minor importance. Moreover, about smectite's presence and its role in the deposits, there are contradictory reports. In this study we report on the phyllosilicate mineralogy of the deposits of Katsikiza, Pagondas, Koutos, Platani, Vrysakia, Rekavetsi and Zygos, Central Euboea, and examine its significance on the evolution of the deposits during diagenesis.

The deposits are characterized by both pisolitic and pelitic textures. They consist of complex (peloids, scarce pisoids) and individual grains of hematite with variable sphericity (angular to rounded) as basic component. They also contain angular to rounded quartz, calcite and accessory chromite fragments, as well as, pyrite in certain sectors. The shape of grains and the texture of the main phases designate limited transportation from the source rocks. The bulk mineralogy was determined by PRXD, while for clay mineralogy was carried out clay fraction separation and ethylene-glycol solvation, before PXRD analysis. Mineral texture characterization and semi-quantitative analysis were conducted with SEM-EDS. Complex peaks from diffraction patterns were analyzed into individual mineral phases with Fityk software. The main phases of the phyllosilicate mineralogy are randomly ordered(R0) mixed layered chlorite-smectite (Chl/Sme) with 10-20% smectite layers and discrete chlorite. Talc (kerolite-pimelite) is minor phase in all deposits, being a main phase locally in the Vrysakia deposit, while serpentine is present in most of the samples, but in small amounts. Corrensite (Corr), the perfectly ordered(R1) mixed layered chlorite-smectite (50% chlorite-50% smectite), is present in Vrysakia and Platani deposits. Discrete smectite(Sme) was identified as major phase in sectors of the Vrysakia deposit, and discrete illite in Katsikiza and Rekavetsi deposits. Finally, a (La, Ce, Nd)-rich phosphate, monazite-like mineral phase have been identified in Vrysakia deposit, fact that suggests a rather diverse origin of the lateritic material in the Fe-Ni sedimentary deposits of Central Euboea, not only ultramafic ophiolitic rocks.

The coexistence of R0 mixed layer chlorite-sme, corrensite, discrete smectite and discrete chlorite, as well as, the limited abundance or lack of serpentine suggest a) a smectite to chlorite conversion during diagenesis of the ore, b) lack of equilibrium in the smectite-to-chlorite transformation and c) dissolution of serpentine during diagenesis. Also, the occurrence of abundant talc layers might be attributed to the transformation of stevensite(Mg-Ni-rich trioctahedral smectite), which probably existed in the primary lateritic mantle, to talc during diagenesis. Therefore, chlorite, R0 mixed layered Chl/Sme and Corr phases are probably products of diagenetic processes and were not formed during lateritization. This is the first report for chloritization of Fe-rich dioctahedral smectite during diagenesis. It is suggested that the smectite to chlorite transformation, the dissolution of serpentine and the transformation of stevensite to talc are related to the mobilization of Ni and other critical elements, such as Co. The reaction paths for corrensite, R0 mixed layered Chl/Sme, discrete chlorite and data from literature may be used for us to suggest a burial temperature of sediments between 70-100°C. Additional work would be necessary in order to confirm the exact reaction paths of phyllosilicates and the mobilization of Ni and critical metals during diagenesis.

Table of Contents

1. Introduction.....	3
1.1 Critical metals in Fe-Ni laterites.....	7
1.2 The sedimentary Fe-Ni deposits of Euboea.....	8
1.2.1 Geological Setting.....	11
Pelagonian zone.....	13
1.3 General characteristics of the ore.....	18
2. Materials and Methods.....	23
2.1 Clay fraction separation.....	24
2.2 Scanning Electron Microscopy with Energy Dispersive Spectroscopy (SEM-EDS).....	25
2.3 Geochemical analyses.....	25
3. Results.....	26
3.1 Minerological and Textural Characteristics.....	27
3.1.1 Bulk Mineralogy.....	28
3.1.2 Clay mineralogy.....	35
3.2 SEM-EDS analyses.....	36
3.3 Chemical analyses.....	38
3.4 Relation of geochemical to mineralogical data.....	43
3.5 REE Mineralogy.....	46
4. Discussion.....	49
5. Conclusions.....	53
Acknowledgments.....	53
References.....	54
APPENDIX.....	63

1. Introduction

The term 'laterite' was presented for first time by British East India Company's surgeon Francis Buchanan in 1807 during an exploration expedition through the western part of Peninsular India. He discovered a brittle reddish brown rock that was extracted with steel tools and used for the manufacture of bricks, which after drying in the sun remained firm ([5]Aleva, 1994; [53]Ghosh and Guchhait, 2020).

Schellmann[105] (1982) made the following important definition: 'Laterites are products of intense sub-aerial weathering whose Fe and/or Al content is higher and Si content is lower than in merely kaolinized parent rock'. The major constituents of laterites are goethite, hematite, Al-hydroxides, kaolinite minerals, and quartz ([53]Ghosh and Guchhait, 2020).

Laterites are generated by geochemical processes during which, the parent rocks undergo external dissolution and erosion under tropical humid climate. This, results to the removal of dissolved in fluids silica, lime, magnesia, soda, potash and in the residual accumulation of a hydrated mixture of Fe, Al, Mn—oxides and hydroxides, through the processes of replacement, capillary action and separation ([53]Ghosh and Guchhait, 2020).

Some of the major factors that control the genesis of laterites through weathering and erosion are presented below:

- The average rainfall of an area
- The type of mineral that undergoes weathering, since each mineral's resistance differ from species to species. In most cases, minerals due to erosion transform to new assemblages or dissolve. Crystal structure and chemical composition are responsible for the mineral's reaction.
- The mechanical stress of the mother rock, since cracks, fissures and faults allow water to penetrate and dissolve minerals.
- The alteration of physical-chemical characteristics of the fluids that interact with the parent rocks , such as pH, during time.
- The relief, which plays important role in the precipitation
- The size and the shape of the pores of the rock or the weathered material ([109]Skarpelis, 2002).

Also, another definition by ([52]Ghosh and Guchhait, 2015) suggests that laterite is reddish-brown product of intense weathering and erosion under tropical climate, made up by mineral assemblages which consist of Fe or Al oxides, oxyhydroxides or hydroxides, kaolinite, and quartz, while exposure to drying can cause the material to harden up. Moreover, the $\text{SiO}_2:\text{Al}_2\text{O}_3+\text{Fe}_2\text{O}_3$ ratio is used for their characterization ([7]Alexander and Cady, 1962; [73]Maignien, 1966; [78]McFarlane, 1976; [112]Tardy, 1992; [20]Bland and Rolls, 1998; [52]Ghosh and Guchhait, 2015). More precisely, laterites that have a $\text{Fe}_2\text{O}_3:\text{Al}_2\text{O}_3 >1$ ratio and $\text{SiO}_2:\text{Fe}_2\text{O}_3 <1.33$ ratio, are being characterized as "ferruginous laterites", while those with $\text{Fe}_2\text{O}_3:\text{Al}_2\text{O}_3$ ratio less than 1 and $\text{SiO}_2:\text{Fe}_2\text{O}_3$ less than 1.33, can be named "aluminous laterites" ([61]Karunakaran and Sinha Roy, 1981; [52]Ghosh and Guchhait, 2015).

Laterites, can be distinguished also, according to their origin. If they are products that come from the weathering of mafic-basic igneous rocks, such as basalt, dolerite, gabbro, which are poor in Si (45-53 % wt) and contain minerals like olivine, pyroxene, feldspar, hornblende, can be characterized as bauxitic laterites. If laterites are derived from ultramafic-ultrabasic rocks such as,

ophiolites, which contain low silica content (<45%), >18% MgO, high FeO, low K and more than 90 % mafic, dark colored minerals, they are named after Fe-Ni laterites. Moreover, laterites form deposits that contain significant quantities of base metals, like Al in bauxites and Fe, Ni, Co in ferronickel type laterites. These kind of deposits are hosted either in situ within the parent rocks (basic and ultrabasic rocks) and called autochthonous, or have been transferred at distance and precipitated in rocks irrelevant with the parent ones, like karstic landforms in limestones, and are called allochthonous. Therefore, we categorize the secondary, transferred deposits as karst bauxites and sedimentary Fe-Ni deposits, respectively.

In this study, we examine sedimentary Fe-Ni deposits, hosted either in ultrabasic rocks or in karstic limestones (karstic nickel). The lateritic material was transported over an important distance through debris flow and other transportation ways and precipitated within a sedimentary basin in the form of lens, layers or enclaves with irregular shape.

Weathering of rocks results to the creation of a lateritic crust, which replaces the upper part of the rock near the surface. This crust doesn't necessarily cover the entire surface of the parent rock, because of differences in thickness or due to weathering. A lateritic crust, regardless of the parent rock, typically consists of 3 layers:

- Saprolite layer: It grows gradually through replacement of the parent rock's minerals from new phyllosilicates and oxides. The porosity increases and coherence decreases from bottom to top inside the layer.
- Clay layer: Rich in clay minerals and considered as transition zone.
- Pisolitic layer: Consists of oxides and hydroxides of Al and Fe with pisolitic texture and oolites, peloids and pisoids particles ([109]Skarpelis, 2002).

Fe-Ni laterites

Under extreme weathering conditions primary minerals in Ni-bearing parent rocks (ophiolites, serpentinites etc) disintegrate and chemical elements like Fe, Ni and Co dissolve in the groundwater. Through this, they can either reprecipitate in already present minerals or integrate in new, stable ones.

Lateritic profiles typically present a structure consisting of the following horizons (from bottom to top): saprock, saprolite, plasmic zone, mottled zone, ferruginous and/or aluminous duricrust or gravels, and soil ([40]Eggleton, 2001; [26]Butt and Cluzel, 2013). Also, some other researchers have presented an alternative, more simplified version of a Fe-Ni laterite profile, which includes from the base ([47]Francké and Nobes, 2000; [1]Aiglsperger et al., 2015):

- The parent rock or protolith, characterized by unweathered magmatic minerals .
- Saprolite, dominated by secondary Si and Mg rich minerals. The alteration of rock to saprolite moves forward as the leaching process removes silica from the matrix without affecting the volume. Saprolite has low porosity, firm and clay-like character with high water content and residual structures.

- Limonite, mostly made up of residual Fe and Al bearing minerals. In the very near surface, the limonite may have been mobilized in surface acid conditions and recrystallized in the form of ferricrete, which can form a hard surface layer .

Saprolitic horizons can be distinguished from the overlying limonitic layer by the Mg discontinuity, which reflects a decrease of MgO content from about 20% to less than 2% ([26]Butt and Cluzel, 2013, [1]Aiglsperger et al., 2015).

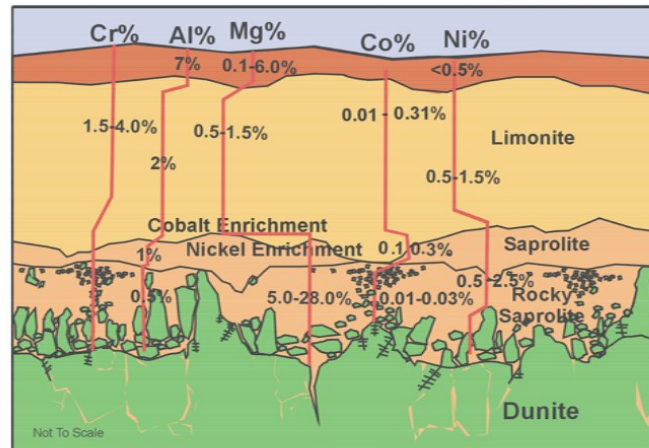


Fig.1: Typical Fe-Ni laterite weathering profile and elements concentrations (courtesy L.D. Queen), (Francké and Nobes, 2000)

Three general ore types are distinguishable, based on the dominant Ni-minerals: (i) oxide type, (ii) hydrous Mg silicate type and (iii) clay silicates type ([103]Samama, 1986; [23]Brand et al., 1998; [55]Gleeson et al., 2003; [48]Freyssinet et al., 2005; [54]Golightly, 2010; [26]Butt and Cluzel, 2013; [91]Proenza, 2015; [1]Aiglsperger et al., 2015).

Oxide type

Oxide Ni laterites, also known as limonitic ores, mainly consist of Fe oxyhydroxides, usually goethite which is the main Ni bearing mineral, located in the upper saprolite up to the plasmic zone. Mn oxides, like asbolane, are also abundant and are enriched in Co and Ni. Oxide ores dispose have average Ni content 1.0-1.6 wt% and represent about 60% of total Ni laterite resources. The upper plasmic horizon and ferruginous duricrust are leached, with usually less than 0.03 % Ni ([26]Butt and Cluzel, 2013; [1]Aiglsperger et al., 2015).

Hydrous Mg Silicate type

This type of lateritic ore forms in the middle to lower saprolite, with minerals enriched in Ni such as serpentine, talc, chlorite and sepiolite. This type of deposits are also known as 'garnierite-type',

due to the above mineralogical mixture. Ni concentrates in newly formed silicate minerals, which form veins following shares or joints and fill open spaces between saprolite blocks. They develop on serpentinized ophiolites and they account for the 32 % of total Ni laterite resources, with an average Ni content of 1.44 wt% ([26]Butt and Cluzel, 2013; [1]Aiglsperger et al., 2015).

Clay silicate type

Clay silicate or smectite-type Ni laterite ores have grades of 1-1.5 wt% Ni and represent 8% of the total Fe-Ni laterite resources. The major minerals are Ni rich saponite and smectite in the middle to upper saprolite up to the middle plasmic zone, which corresponds to the Mg-discontinuity. Upward follows a goethitic horizon and a hematitic duricrust (Butt and Cluzel, 2013; Gleeson et al., 2003; Aiglsperger, 2015).

As a fact, genesis of the three ore subtypes is affected from the tectonics and the paleo-environment, as oxide-type and smectite-type occur from a continuous lateritization process in stable basins, while in garnierite-type ores, lateritization depends on the fall of the groundwater table, on the leaching level within the weathering profile and in the presence of cracks and spaces in the saprolite ([31]Cluzel and Vigier, 2008; [26]Butt and Cluzel, 2013, and references therein; [115]Villanova-de-Benavent et al., 2014; [92]Putzolu, 2021).

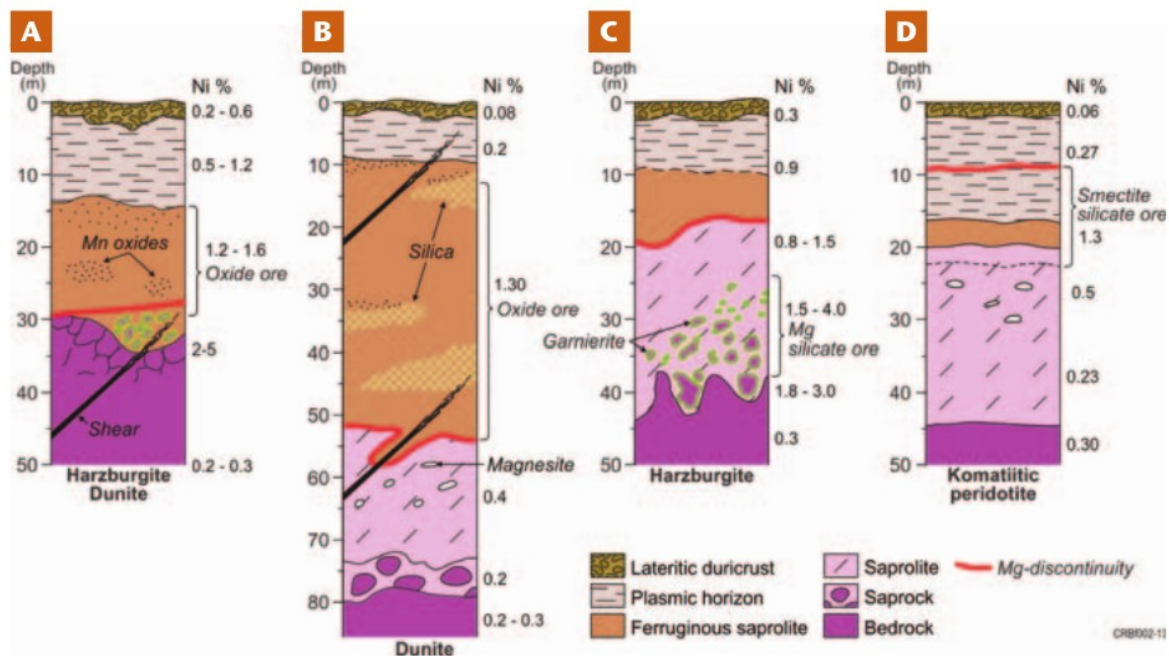


Fig.2: Lateritic profiles developed on serpentized ultramafic rocks showing the principal nickel laterite ore types: (A) oxide (B) partly silicified oxide (C) hydrous Mg silicate (D) Clay silicate (Butt and Cluzel, 2013)

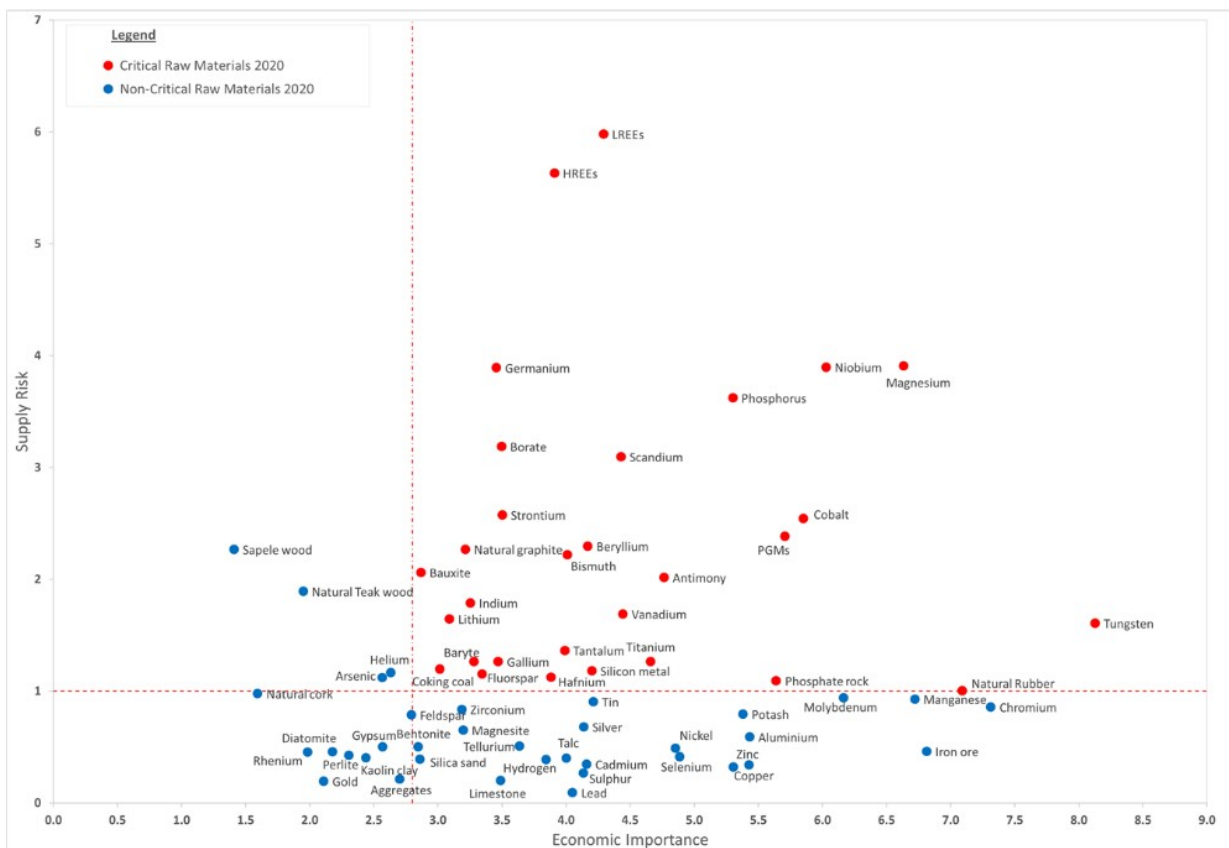
1.1 Critical metals in Fe-Ni laterites

Critical minerals, metals and raw materials are considered those that have significant economic impact in key sectors of the economy, present a supply risk, and have no commercially available substitutes (Ministère de l'Énergie et des Ressources naturelles of Québec Canada, 2017). These metals are essential to renewable energy and green technologies, medical devices, electronics, aeronautics, telecommunications, transportation electrification, agricultural production and modern household devices.

Fe-Ni laterites constitute a potential resource for critical metals such as Co, PGEs, REEs, Sc, Ti, Nb and V. Critical metals tend to concentrate in laterites for several reasons, such as:

- Intense weathering, which results to residual enrichment.
- Mobilization of critical metals within the lateritic profile due to variable pH and Eh conditions, which causes elements to precipitate at certain geochemical barriers.
- Neof ormation processes which result from interactions between limonitic soils and the biosphere in the upper laterite, such as the formation of secondary PGE-bearing mineral phases.

Total content of critical metals in most Fe-Ni laterites is relatively low, compared to conventional magmatic ore deposits, but still is of economic significance as critical metals should be handled as low-cost by-products during the Ni (+Co) recovery. Original and progressive extraction methods, which are currently under development will boost the significance of Ni laterites as future unconventional critical metals deposits ([1]Aiglsperger et al., 2015).



1.2 The sedimentary Fe-Ni deposits of Euboea

The ferro-nickeliferous ores of Attica-Boetia, Lokris, Euboea and Skyros, were firstly described by Ktenas[70] (1930). He characterized them as a result of erosion and partial transportation from magmatic assemblances within the peridotites, in the form of magnetite, Ni- and Cr- hematite. W. Petrascheck[89] (1954) divided the Fe-Ni ores of Lokris to erosion products (hosted in ophiolites) and sedimentary formations (hosted in limestones). Maratos[76] (1960) used the same definition and classified the two groups as autochthonous and allochthonous ores, respectively. Augustithis[14] (1962) discovered limonitic pissoliths in the Ag. Ioannis deposit Larymna, and observed the diagenetic and meta-diagenetic formation of hematite, lepidocrocite, martite, malachite, covellite and other minerals. Kurzwell[71] (1966) in the same area, observed that Ni exists in colloid form inside the ore and participates in antigorite and chlorite. Albandakis[3] (1974) mentioned that the Ni bearing minerals in Larymna are antigorite, talc and montmorillonite. He, also, [4](1980) discovered that the first type of deposits (in situ formations), are of restricted abundance, while the second type (secondary-sedimentary) comprise the majority of the known Ni-Fe lateritic deposits of Greece.

Independent studies showed that: Ni-ores have been transported onto peridotites or onto karstified Jurassic limestone and have been overlain by Lower Cretaceous limestones. The multistage transportation and redeposition of the metalliferous sediments, can be confirmed by the presence of a conglomerate, composed of rounded-elongated saprolite and silified saprolite blocks of various sizes, within a matrix of pisolitic laterite and calcite, at the contact between the laterite body and the limestone basement ([6]Alevizos, 1997; [108]Skarpelis, 1997; [41]Eliopoulos and Economou-Eliopoulos, 2000; [59]Kalatha and Economou-Eliopoulos, 2015; [114]Valeton et al., 1987; [43]Economou-Eliopoulos et al., 2017).

In the central part of Euboea island, the presence of lateritic deposits is known since the mid of 50's ([11]Aronis G., 1954; [110]Spiliadis Th., 1958; [62]Katsikatsos et al., 1969). Advanced studies have been made by Larco S.A. mining company, which is currently mining the deposits. However, most research results are unpublished reports, including detailed mapping of the outcrops, evaluation of the deposits based on drilling programmes, detailed description of cores, chemical analyses etc. There is also, many published work from scientists of the company and other workers.

Katsikatsos ([62]1969, [63]1975, [65]1980) described the mineralogy, texture and geochemistry of the ores from Kimi, Attali and Nea Artaki areas and reported on the origin of the ore and the genetic relations between bauxite and Fe-Ni ore deposits. The Fe-Ni deposits originated from the laterization of the ophiolitic rocks of the Eohellenic tectonic nappe. The Kalogeros mine in Nea Artaki, Euboea has average Ni $\leq 1\%$ and almost uniformly distributed in the ore. The Co content varies between 90 and 1200ppm in close relation to the Ni content. The Cr content varies between 0.14-2.28% without any particular distribution pattern. The ore consists of quartz, hematite, goethite, antigorite, garnierite, talc and magnetite.

Albandakis[3] (1974) described the interchange between the massive and pissoitic ore, pyritic fossils that are related to shallow marine environment, and the presence of marcasite (sedimentary origin).

[114]Valeton et al. (1987) and Rosenberg[101] (1984) related the deposits of central Euboea with ultrabasic parent rocks and mentioned that the major minerals include hematite, goethite, quartz, chrome spinel and chlorite accompanied by minor dispersed illite.

[9]Andoniades and Vgenopoulos (1989) presented data from the Pissona and Katsikiza mines, and confirmed the origin of the Fe-Ni deposits from alteration of ultrabasic rocks. In addition, they suggested alkaline pH conditions for their formation, reported absence of Mg in the ore and showed that the Ni bearing phases in the ore are: garnierite, nimite and willemseite (talc group). Quartz, hematite, goethite, corrensite, chlorite, antigorite, saponite, chromite and calcite compile the paragenesis.

[84]Mposkos et al. 1996, examined the deposits of Triada and Katsikiza and concluded that the Ni bearing mineral of the laterites (77% of Ni) is chlorite and in minor degree hematite, illite and last chromite. Hematite, the dominant mineral phase, contributes only 18% of Ni to the ore, while he forms pissoiliths which contain inclusions of quartz, chromite, chlorite and illite.

[43]Economou-Eliopoulos et al., 2017, presented geochemical data about samples from Central Evia's Fe-Ni laterites characterized by significant Ni, Cr, Co, Mn and V contents, while investigation with SEM-EDS showed the presence of goethite, in the form of rounded fragments and in matrix, as a dominant component, with a wide range of high-Cr to high-Al impurities.

[104]Samouhos et al. 2018 published data on the nanomineralogy and geochemistry of Fe-Ni laterite samples from the Triada deposit Central Euboea and showed that the ore contains chlorite group phyllosilicate minerals, chlorite group/illite mixture, illite and a hematite-like phase. TEM-EDS analyses showed that Ni-phyllosilicates and hematite-like phases in Evia samples are rich in Ti-Cr-Mn-Ca, except for Ni. From discrimination diagrams (e.g. Th/Sc vs. Zr/Sc and Ce/Ce* vs. Eu/Eu*) Samouhos et al. 2018 suggested that the studied Fe-Ni-ores have a rather diverse origin, not only from ultrabasic ophiolitic rocks, as is commonly considered.

The scope of this study is to investigate the processes that took place during diagenesis of lateritic Fe-Ni deposits of Euboea, and how they affected the clay mineralogy. Moreover, a detailed geochemical analysis both on major and trace elements was carried out, which shed light on the complex characteristics and the origin of Euboea's deposits, additional to previous workers.

1.2.1 Geological Setting

Geologically, Greece, can be divided to several isopic or geotectonic zones, according to the paleogeographic, stratigraphic and tectonic evolution (Fig.4). Mountrakis ([80]1985; [83]2010) described these zones supporting the theory of gradual rifting of various continental fragments from Gondwana hyper-continent at the beginning of Mesozoic and their independent motion towards Eurasia. This gradual movement created new oceanic crust to the rear through rifting, and resulted to the final collision with the Eurasia at the end of the Mesozoic

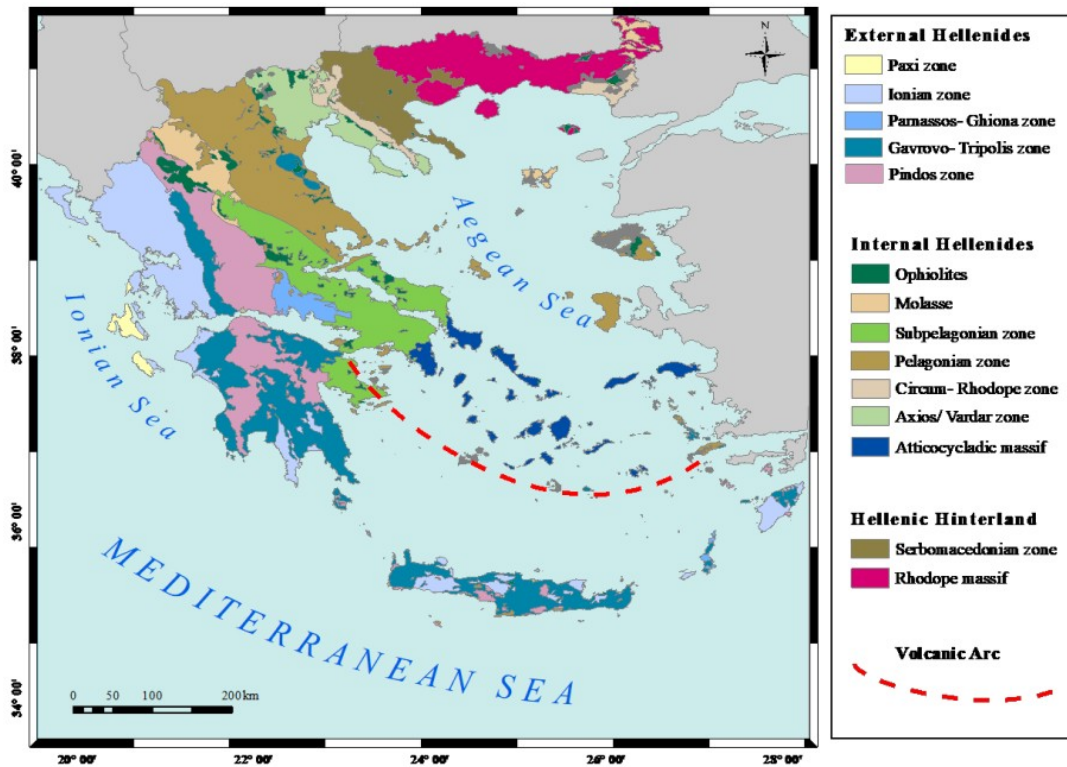


Fig.4: Structural zones of the Hellenides after Mountrakis (1986)

Central Euboea can be considered as a sedimentary succession consisting of Paleozoic slates and limestones, Triassic and Jurassic limestones and ophiolites. This succession is covered by transgressive Cenomanian limestone followed by thin bedded Late Campanian limestone, which progressively passes to flysch (Maastrichtian to Paleocene) ([10]Argyriadis, 1966; [13]Aubouin, 1977; [37]Deprat, 1904; [56]Guernet, 1971; [96]Renz, 1940). The central parts of Evia island tectonically belong to the westernmost unit of the internal Hellenides, the non-meta-morphic, western part of the Pelagonian Zone (Fig.5) ([51]Gartzos et al., 2009). The ophiolites of Central Evia probably belong to the eastern belt and come from the Vardar/Axios oceanic basin ([87]Papanikolaou D., 2009).

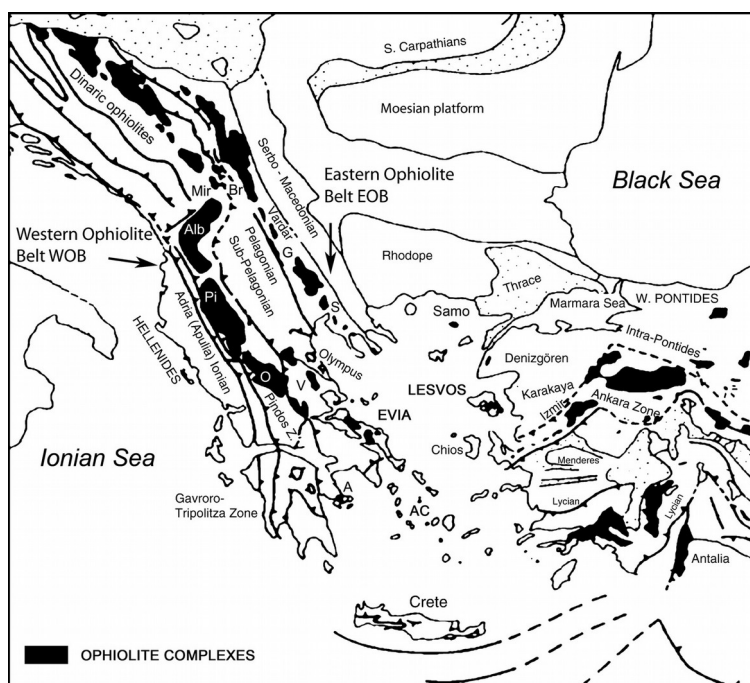


Fig.5: Distribution of ophiolite complexes in the Dinarides, Hellenides and Taurides of western Turkey. The tectonic sketch map is modified after Robertson and Shallo (2000). WOB =Western Ophiolite Belt, EOB = Eastern Ophiolite Belt, Ophiolite complexes: A = Argolis, AC = Attico-Cyclades, Alb = Albanian, BR = Brezovica, EVIA, G = Guevgueli, Mir = Mirdita, LESVOS, O = Othris, Pi = Pindos, S = Sithonia, Samo = Samothraki, V = Vourinos

Pelagonian zone

The term Pelagonian zone was firstly presented by [12]Aubuin, 1959 and included: a) metamorphic rocks of Western Macedonia, East Thessaly, Euboea, Attica and Cyclades islands, b) the overlain sedimentary basin of Upper Palaeozoic-Mesozoic age, which represents the pelagonian ridge between the ocean of Axios (Vardar) in the east and Pindos sillon in the west. Aubuin(1959) also named Sub-pelagonian zone the western edge of the Pelagonian zone, which was the transition zone of the Pelagonian micro-continent to the Pindos trench. This area is characterized by the presence of big ophiolitic masses.

J. Brunn, 1956, named the Pelagonian zone as “Pelagonic mass with sediments” and Sub-Pelagonian zone as “Transition Zone”.

[96]Renz (1940), named “Pelagonian terrane” all the metamorphic rocks in the area of West Macedonia, East Thessalia, north Euboea and north Sporades. He also named the unmetamorphosed parts of this zone (Othrys, Central Euboea, Boeotia, Attica) as the zone of Eastern Greece, which was characterized by the presence of a formation called “slate-chertstone with ophiolitic bodies” and Middle-Upper Cretaceous sediments.

Nowadays the two former zones (Pelagonian and Sub-Pelagonian) consider as one Pelagonian zone divided in the metamorphosed part (Pelagonian terrane, Renz) and the unmetamorphosed part (Sub-Pelagonian).

Late Paleozoic-Early Triassic rifting during the break-up of Pangea and subsequent Early-Middle Triassic spreading led to the formation of a passive margin facing the Neotethys/Vardar ocean within the Pelagonian realm (e.g., [22]Bortolotti & Principi, 2005; [111]Stampfli & Borel, 2002). Rifting and marine invasion was reflected in the deposition of Permian and Early Triassic synrift and postrift sediments on top of the Variscan basement, and extensive deposition of carbonate platform sediments from Middle Triassic to Middle Jurassic times (e.g., [35]De Bono, 1998; [36]De Bono et al., 2001; [107]Scherreiks et al., 2010). Upper Paleozoic-Early Triassic clastic deposits together with thick Pelagonian carbonates of Triassic and Jurassic age characterize a significant part of the Pelagonian zone. Deep water sediments and volcanic-sedimentary mélange successions of similar age are also present. The Pelagonian carbonate platforms drowned in the Middle-Late Jurassic as marked by deposits of reef debris carbonates intercalated with nodular cherty carbonates. Late Jurassic radiolarites and greywackes are present in the upper members of the deepening sequence ([33]Danelian & Robertson, 2001; [99]Robertson, 1991; [106]Scherreiks, 2000; [90]Porkolab et al., 2019).

The Permian-Jurassic sedimentary succession of the Pelagonian zone is overlain by obducted ophiolitic rocks that originated in the Neotethys ocean. The ophiolites probably formed in a suprasubduction zone setting following intraoceanic subduction initiation ([15]Barth et al., 2008; [30]Clift & Dixon, 1998; [72]Maffione et al., 2015). Intraoceanic obduction was followed by the emplacement of the ophiolitic thrust sheet(s) onto the Pelagonian passive margin leading to deformation and metamorphism in the Pelagonian zone ([90]Porkolab et al., 2019). The subducting trench collided with the passive margin and the already submerged Pelagonian carbonate platform

evolved into a folded foreland basin, in which siliciclastic turbidites, debris flows, and limestone olistoliths accumulated. During suturing of the Vardar ocean, the already thrust assembled accretionary complex was thrust westwards over the Pelagonian microcontinent, accompanied by large-scale recumbent folding and thrusting of Late Cretaceous Pelagonian carbonate platform slope units ([98]Robertson, 1990).

The burial of the Pelagonian margin was followed by exhumation and the formation of a regional Late Jurassic-Early Cretaceous erosional discontinuity in the Evia-Pelion-Sporades region ([58]Jacobshagen & Wallbrecher, 1984; [35]De Bono, 1998). Karstification of the Pelagonian carbonates is associated with the genesis of bauxites and laterites (e.g., [58]Jacobshagen & Wallbrecher, 1984; [99]Robertson, 1991; [90]Porkolab et al., 2019).

Both the ophiolitic nappe and the platform carbonates, during the Alpine orogenesis were gradually covered by upper Cretaceous (Cenomanian-Turonian) shallow-water limestones ([57]Guernet, 1975; [69]Katsikatsos et al., 1986; [97]Richter et al. 1996; [36]De Bono et al., 2001). Deposition of Albian-Turonian transgressive conglomerates, carbonates, and finally Turonian-Paleogene flysch marks Late Cretaceous transgression and the formation of a foredeep basin, which probably signifies the final closure of the Neotethys/Vardar ocean between Pelagonia and Eurasia ([58]Jacobshagen & Wallbrecher, 1984; [90]Porkolab et al., 2019).

For some researchers, all the formations above the Upper Cretaceous unconformity construct a different zone called Zone of Eastern Greece. This zone typically includes: 1. Flysch (Danian-Eocene) 2. Pelagic limestones with *Globotruncana* (Maastrichtian) 3. Limestones with rudists (Campanian-Maastrichtian) 4. Turbidites (Cenomanian-Turonian) 5. Neritic limestones (Cenomanian-Turonian) 6. Conglomerates and sandstone limestones (Cenomanian). This zone is considered only for the period Upper Cretaceous-Eocene and has undergone only the Alpine orogenic phase of Eocene-Oligocene. All formations that are older and belong to zones under the unconformity have been affected by two orogenic phases: one in Upper Jurassic-Lower Cretaceous and the Alpine tectonism ([88]Papanikolaou, 2015).

A major Ocean, that lasted for about 70 My from the Middle Triassic to the Middle Jurassic, was the "Maliac Ocean". The Maliac Ocean, located between the Pelagonian (W) and the Serbo-Macedonian (E) continental blocks, is considered as the main Tethyan Ocean branch from which produced the Hellenic Ophiolites obducted during the Middle-Late Jurassic, over the Pelagonian domain ([45]Ferriere et al., 2016).

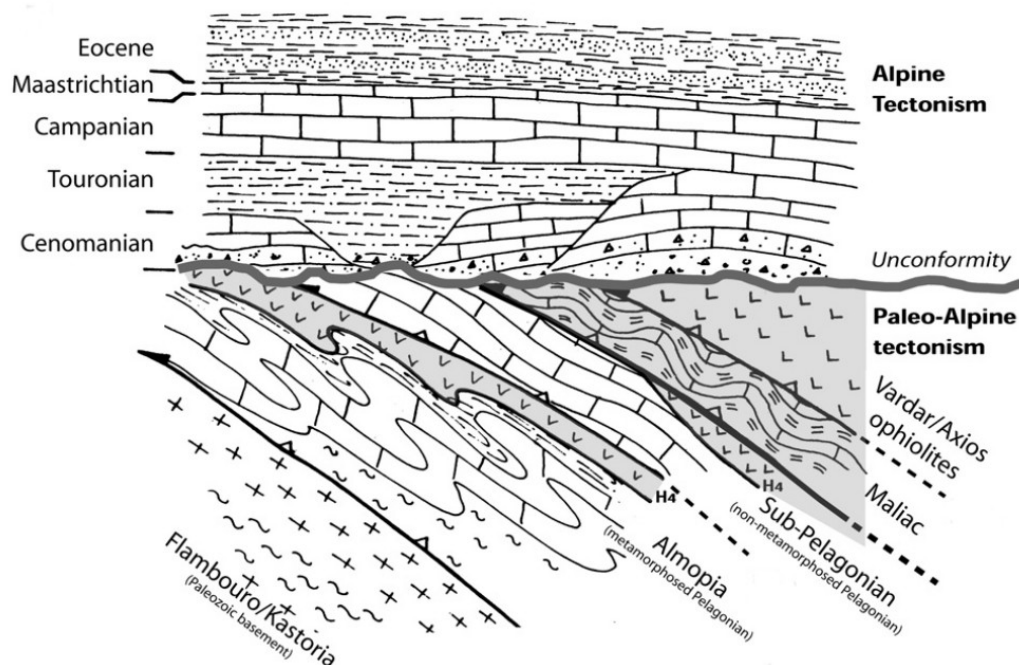


Fig.6: Schematic representation of the upper Cretaceous transgression over the internal Hellenides, showing the timing of tectonic emplacement of the ophiolites and related pelagic sequences of the Maliac unit over the units of the internal carbonate platform in late Jurassic–early Cretaceous (after Papanikolaou, 1986a, modified). The Sub-Pelagonian unit is not metamorphosed whereas the Almopia unit is metamorphosed together with the Paleozoic basement of the Flambouron and Kastoria units.

According to [65]Katsikatsos et al., (1980) and [66](1981), the geological regime of central Euboea is characterized by a thick sequence of formations which consists of a Permian pre-alpine clastic metamorphic substrate at their bottom. This sequence is overlain by intercalations of Triassic–Jurassic dolostones, dolomitic limestones and limestones, which progressively turn into silicified limestones, followed by an Upper Jurassic tectonometamorphic complex (mélange) of schists and mudstones often containing serpentized ophiolitic olistoliths from the overlying parent ophiolitic rocks.

The Alpine units in the area are ([64]Katsikatsos, 1977; [69]Katsikatsos et al.,1986; [50]Gartzos, 1986):

1. A crystalline basement: mainly composed of muscovitic and biotitic gneisses, gneiss-schists and schists.

2. Upper Paleozoic formations: which overlie transgressively on the crystalline basement, and they are mainly composed of clastic rocks with intercalations of limestones.

3. Formations of Lower and Middle Triassic: that are mainly composed of clayey-sandy deposits, basic igneous rocks and generally sea shallow limestones.

4. Triassic–Upper Jurassic neritic limestones and dolomites: usually more than 1000 m thick. This unit passes upwards into a transitional unit of coarse, turbiditic limestones and fine-grained, pelagic sediments, with radiolarian mudstones of Berriasian to Valanginian age ([16]Baumgartner and Bernoulli, 1976).

5. Eohellenic tectonic nappe: This nappe has been divided by [64]Katsikatsos (1977) into two subunits according to their lithological composition, origin and inferred tectonic emplacement: a) the volcano-sedimentary subunit which is overlain with tectonic contacts by slices of the amphibolite sole (defined as “Mesozoic carbonate and clastic sequence”); b) up to 500 m masses of ultramafic to mafic rocks; overlain by upper Cretaceous transgressive limestones which pass in the uppermost part into flysch sediments of Maastrichtian age.

According to [44]Ferriere et al. (1988) and [99]Robertson (1991), the volcano-sedimentary subunit is an up to 3 km-thick polygenetic mélange, known as the “Pagondas complex”, which comprises late Triassic shallow-water limestone and calciturbidites, radiolarites, Triassic to Jurassic tholeiitic and alkaline basalts as well as minor andesites. This complex has been interpreted as the remnant of a Triassic–Jurassic oceanic basin, the Pindos ocean basin linked to the western extension of the Neotethys.

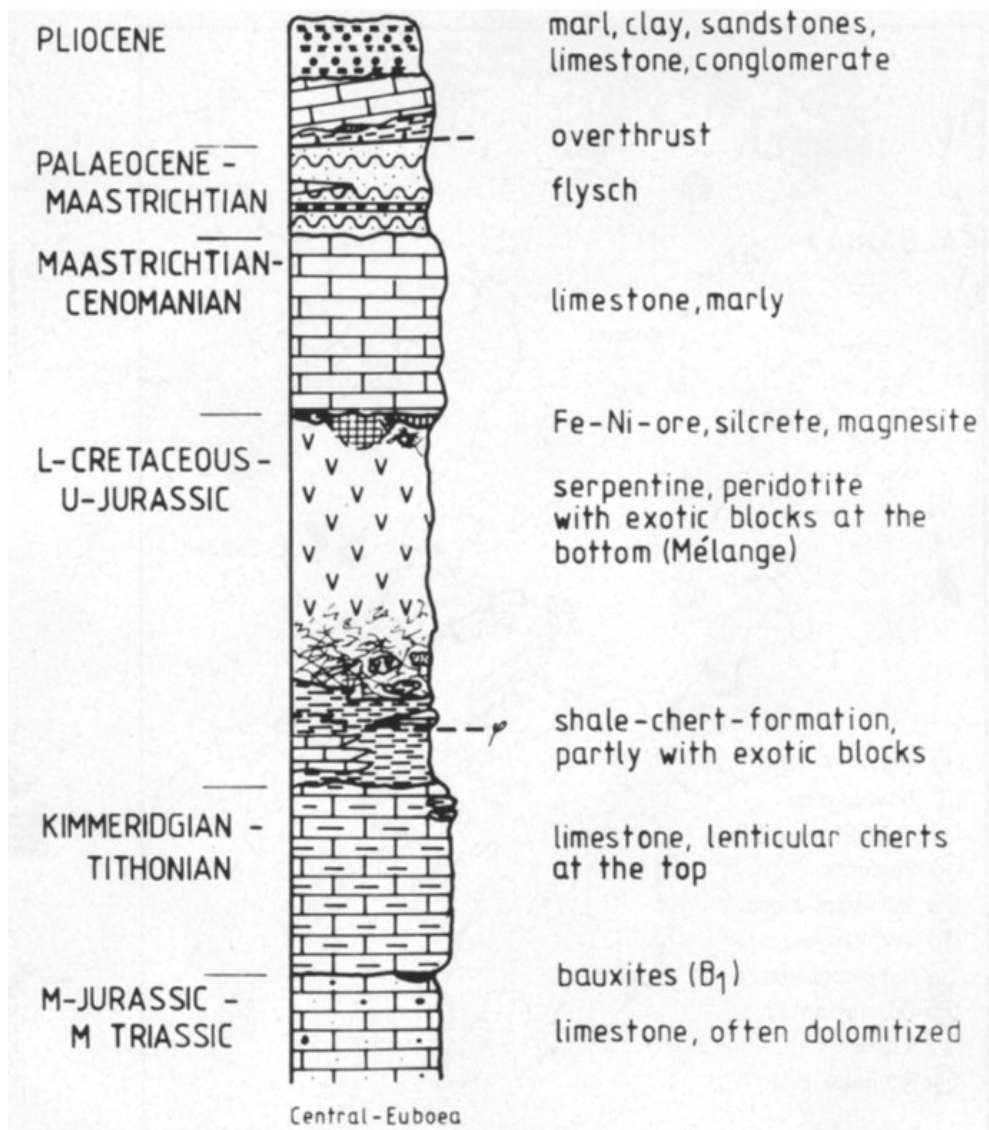


Fig.7: Stratigraphic succession in Central Euboea region (after Reche, 1983)

In summary, central (and northern) Euboea comprises a basement of Precambrian ('Hercynian') crystalline basement, above which lies, transgressively, a thick sequence of Late Palaeozoic (? Late Permian) metasedimentary rocks, mainly terrigenous clastics and carbonates ([69]Katsikatsos et al., 1986). These units are, in turn overlain by Mid-Triassic volcanics and sediments related to rifting of Neotethys, followed by a Late Triassic-Early Cretaceous carbonate platform, correlated with the traditional Pelagonian Zone. During the Late Jurassic-Early Cretaceous the continental margin sequence was overthrust by ophiolites and related melange (traditional Diabase-Chert Formation) (e.g. [16]Baumgartner and Bernoulli, 1976), collectively dated as Triassic to Early Cretaceous. Ophiolite emplacement was followed by tropical weathering and deep erosion, leading to the accumulation of iron-nickel and bauxite deposits. These sediments were, in turn, transgressed by up to 270 m of Late Cretaceous (Cenomanian-?Turonian) shallow-water carbonates, that passed up into 20-50 m of Maastrichtian Globotruncana-bearing hemipelagic carbonates ([57]Guernet, 1975; Katsikatsos et al., [66]1981; [69]1986). This was followed by deposition of terrigenous and calcareous flysch of Palaeocene-Eocene (Ypresian) age, with a structural thickness of 500 m ([19]Bignot et al., 1973; Katsikatsos, 1981[67]a,[68]b). The flysch comprises siliciclastic sediments, including conglomerates, redeposited limestone, and

detached limestone blocks, as well as slices of serpentinite, mafic lava ('diabase') and pelagic limestone of Maastrichtian age. Following erosion, Neogene sedimentation commenced with conglomerates, which passed up into Aquitanian (Early Miocene) lacustrine limestones ([57]Guernet, 1975; [68]Katsikatsos et al., 1981b, [98]Robertson et al., 1990).

1.3 General characteristics of the ore

The Fe-Ni sedimentary deposits of Euboea occur Upper Jurassic limestones or overthrust ophiolites or rarely schist-chertstone formations.

Jurassic limestones host the ore in the form of layers or bedded lenses with anomalous floor, as the lateritic filled the karstic cavities. The floor, moreover, presents the weathered, textured surface, which developed in the pro-Cenomanian period due to regression and erosion, which was followed by sea transgression and ore sedimentation. When hosted in ultrabasic bodies, the ore is usually in the form of lenses.

The thickness of the deposits varies from some centimeters to 30 meters. The transition of the ferronickeliferous ore to the overlying Upper Cretaceous limestones is usually concordant ([65]Katsikatsos et al., 1980).

The texture of the ore is either pisolitic or massive, and all the intermediate variations between. It also contains ultrabasic pebbles, mostly together with pisolites, which originate from the nearby peridotites and constitute weathering products of the pre-Upper Cretaceous period. Generally, the pisolitic ore tends to occur in the lower sectors of deposits, whereas massive ore occupies the upper sectors of the deposits. Moreover, the interchange of the two types of ore is common, both laterally and vertically, in a small distance throughout the deposit. Finally, sandstone forms of ore are also common, accompanied by ophiolitic fractions and flint pebbles, due to colloidal SiO₂ sedimentation ([3]Albandakis, 1974).

The formation of pisolithic structures, according to Albandakis, occurred due to surface tension, which affected the colloidal particles of Fe, during sedimentation in a epi-continental basin. More precisely, waves and sea currents contributed to maintain pisolith particles as an emulsion in the seawater, grow in size and precipitate after. From the interchange of pisolithic and solid texture within the deposit, we can assume that the ore precipitated in the form of chemical sediment, and pisoliths emerged through initial sedimentation and paleo-environment conditions, and not through diagenesis.

In some areas of Central Euboea, such as the Platani mine, rocks from the schist-chertstone formation underlay the Fe-Ni ore. They are solid, stiff bodies mostly made of opal, chalcedony, Fe oxides and microcrystals of quartz. Their thickness can reach up to 30 meters maximum, while their sedimentation occurred during the Upper Cretaceous sea level rise, right before or simultaneously with the ferronickeliferous ore. The presence of flint fragments and veins is abundant in the ore.

In the region of Attali-Triada mine [3]Albandakis (1974) reported Miliolidae, Cuneolina, Nezzazata microfossils in the chertstones. This micro-fauna is representative of Cenomanian age and relatively shallow sea paleoenvironment. The same fossils have been spotted in the overlying Upper Cretaceous limestones, above the ore. This fact leads to the conclusion that there was both chemical and clastic, marine sedimentation the Upper Cretaceous, since, in a basement of

ultrabasic rocks or Jurassic limestone precipitated silica sediments, Fe-Ni ore and finally, carbonates.

Vrysakia Deposit

The ore is hosted in a large cavity of Jurassic limestones, forming a lens. The overlying Upper Cretaceous limestones have been stripped during excavation. The ore and Cretaceous limestones, since they are in concordance, present the same layering W-E 50°.

We collected 16 representative samples from this mine, trying to investigate the ore in 2 cross-cut sections inside the lens. 12 samples were taken from the horizontal direction and 4 samples vertically. The standard distance between horizontal samples was 2.5 meters, with some exceptions, for example sample 5A was collected 0.5 m from sample 5B.



Fig.8: The Fe-Ni ore of Vrysakia deposit, forming a lens

Sample	Colour	Lusture	Fracture	Texture	Form
EB-1	Reddish-brown	Dull	Irregular	Cataclastic	rocky with microveins
EB-2	Reddish-brown	Dull	Irregular	Pelitic/cataclastic	rocky
EB-3	Reddish-brown	Semi-metallic	Irregular	Clastic/Pisolithic	rocky
EB-4	Reddish-brown	Semi-metallic	Irregular	Pelitic	earthy
EB-5A	Reddish-brown	Dull	Conchoidal	Pelitic	waxy
EB-5B	Steel-gray	Dull	Irregular	Pelitic	earthy
EB-6	Reddish-brown	Dull	Irregular	Clastic	earthy
EB-7	Reddish-brown	Metallic	Irregular	Pelitic	rocky
EB-8	Reddish-brown	Semi-metallic	Irregular	Pelitic	rocky
EB-9	Light gray/ashy	Metallic	Irregular	Pelitic	earthy
EB-10	Reddish-brown	Semi-metallic	Irregular	Filmed/layered	rocky
EB-11	Reddish-brown	Dull	Irregular	Pelitic	rocky/grainy
EB-12	Reddish-brown	Semi-metallic	Irregular	Pelitic	rocky/grainy
EB-13	Reddish-brown	Semi-metallic	Irregular	Pelitic	rocky/phylloid
EB-14	Reddish-brown	Metallic	Irregular	Pelitic	rocky/grainy
EB-15	Reddish-brown	Dull	Conchoidal	Pelitic/sandy	waxy
EB-16	Dark-chocolate	Semi-metallic	Irregular	Pisolithic/sandy	earthy/grainy
EB-17	Reddish-brown	Dull	Irregular	Pisolithic/sandy	rocky/schist
EB-18A	Reddish-brown	Dull	Irregular	Filmed/layered	schist
EB-18B	Dark olive	Dull	Irregular	Pelitic	rocky
EB-19	Reddish-brown	Dull	Irregular	Pisolithic/clastic	earthy, brittle
EB-20	Dark-chocolate	Dull	Conchoidal	Pelitic	rocky
EB-21	Reddish-brown	Dull	Irregular	Filmed/bedded	rocky, brittle
EB-22	Dark-chocolate	Dull	Irregular	Cataclastic/Pisolithic	earthy, brittle
EB-23	Dark-chocolate	Dull	Irregular	Pelitic	rocky

Table 1: Macro-scopical characterization of samples

Sample	Description
EB-1	Grains of massive Fe ore in a reddish groundmass, with microveins and minor hematite
EB-2	Compact, cataclastic texture, with groundmass of clastic Fe ore particles
EB-3	Angular and rounded micaceous, platy hematite crystals with pisoliths
EB-4	Inside the matrix stand out angular and rounded Fe oxyhydroxide, oxide grains occasionally with high density
EB-5A	Waxy touch, dense, compact groundmass with minor light-colored mineral assemblages
EB-5B	Earthy, weathered groundmass micro-crypto crystalline
EB-6	Angular particles of compact Fe ore in earthy groundmass
EB-7	Angular, rounded hematite and angular goethite grains in dense distribution
EB-8	Mostly rounded particles of Fe ore, may contain hematite inclusions
EB-9	Earthy form with shiny, platy metallic crystals, probably sulfides
EB-10	Angular and rounded grains of hematite and goethite, bedded formation of pale colored minerals
EB-11	Irregular Fe ore particles of various size, bedded like structure
EB-12	Grainy angular and rounded hematite particles in residual matrix
EB-13	Angular and rounded grains of hematite in amorphous mass
EB-14	Angular and rounded grains of hematite in high distribution in the Fe oxy-hydro-oxide groundmass
EB-15	Bedded structure, with waxy touch and crypto crystalline mass
EB-16	Angular and rounded ore particles with pisoliths and sandy touch
EB-17	Pisolithic particles occasionally, mostly made of hematite
EB-18A	Sample from the schist-chert stone formation
EB-18B	Ophiolitic, serpetinized fragmented from schist-chert stone formation
EB-19	Earthy, pisolithic and brittle, white minerals sporadically
EB-20	Hardened, conchoidal crypto crystalline mass
EB-21	Layered structure with white minerals laminates
EB-22	Cataclastic, pisolithic structure with clastic hematite grains at least 5mm
EB-23	Clastic ore particles and angular, rounded hematite grains

Table 1 (continued): Brief description of samples macroscopically



Fig.9: Vrysakia open pit mine Central Euboea (April, 2021)

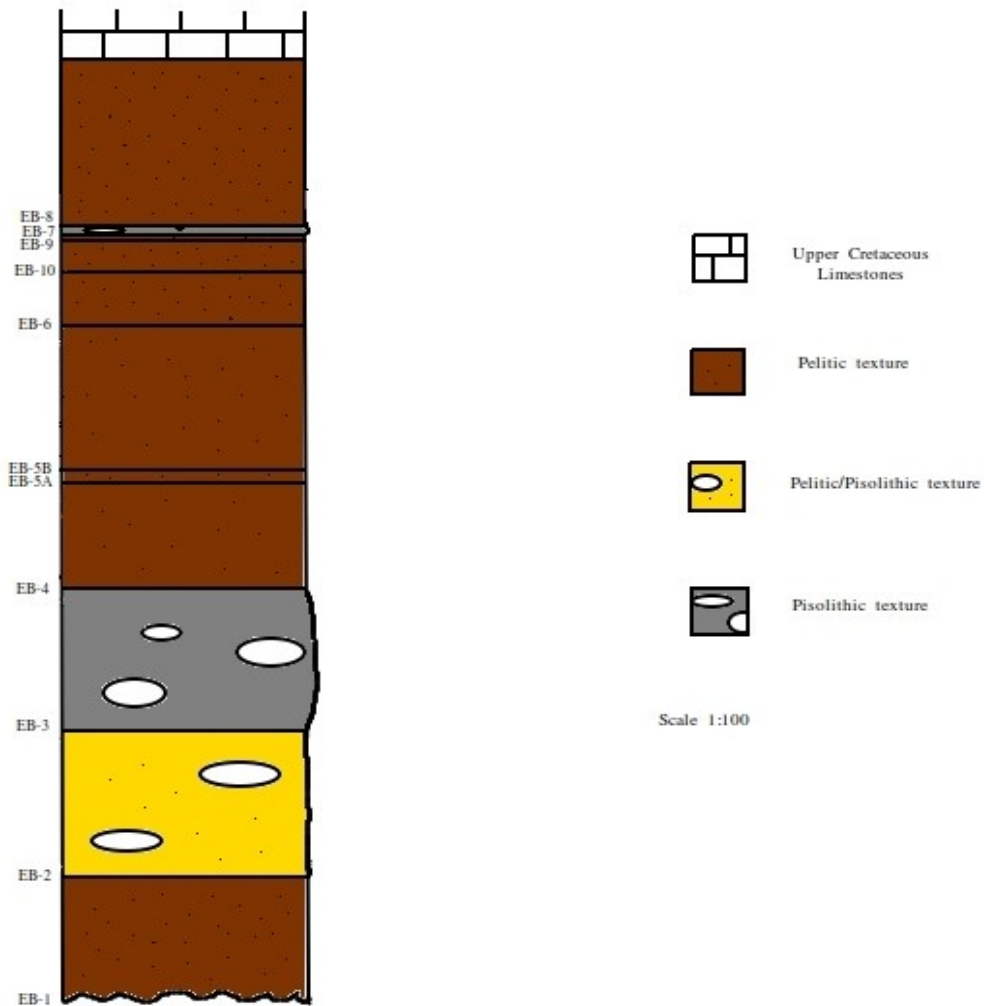


Fig.10: Stratigraphic column of Vrysakia deposit with sample positions

- The deposit develops unconformably over Triassic limestone and is overlain conformably by Cenomanian limestone.
- 16 samples were collected from the Vrysakia deposit along one vertical and one horizontal profile
- The deposits are characterized both by pisolitic and pelitic textures

2. Materials and Methods

Analytical Methods

27 samples have been collected from the mines: Katsikiza, Pagondas, Koutos, Platani, Vrysakia, Rekavetsi and Zygos. In Vrysakia mine we carried out a profile sampling of 16 samples along the vertical and horizontal direction, with 4 and 12 samples respectively. The remaining samples were collected randomly from the other deposits. Mineralogical analyses were conducted through powder XRD diffraction (P-XRD), metallographic microscope and scanning electron microscopy (SEM), equipped with energy dispersive spectroscopy (EDS).

The samples were dried overnight at 105 °C and ground in an agate pestle and mortar to pass through 63 µm sieve. The PXR D measurements were carried out in bulk samples, clay fraction samples (in glasses) air dried and ethylene-glycol solvated.

Bulk Mineralogy

The samples were examined on a Bruker D8 Advance Diffractometer equipped with a Lynx Eye strip silicon detector, using Ni-filtered CuK α radiation (35 kV, 35 mA). Data were collected in the range 4–70° 2 θ with a step size of 0.02° and counting time 1 s per strip step (total time 63.6 s per step). The XRD traces were analyzed and interpreted with the Diffract Plus software package from Bruker and the Powder Diffraction File (PDF).

Quantitative analysis was performed with AutoQuan software, which uses the RIETVELD method. This method, creates a theoretical model which adjusts to the original diffraction pattern, using the least square method, instrumental and structural model parameters (Young, 2002). For the fitting calculations Gauss, Lorentz, Pseudo-Voigt and Pearson VII equations are used. The calculated peak intensity in every step scan point can be described by:

$$Y_{i(c)} = S \cdot \sum_{hkl} L_{hkl} \cdot |F_{hkl}|^2 \cdot \Phi(2\theta_i - 2\theta_{hkl}) \cdot P_{hkl} \cdot A \cdot \rho_{hkl} + Y_{bi}$$

S= Scale Factor

F_{hkl} = Structure factor

L_{hkl} = Lorentz factor

P_{hkl} = Layer frequency factor

ρ_{hkl} = Orientation factor

A = Absorption factor

Y_{bi} = Background intensity

Φ = Profile Shape Function

The calculation of the percentage of each crystalline phase can be described by:

$$W_i = S_i(ZMV)_i / \sum S_n(ZMV)_n$$

W_i = The content of phase i in the sample

S_i = Adjustment factor for phase i

Z_i = The number of molecules for each phase i cell

M_i = Molecular weight

V_i = Cell volume

n= Number of crystalline phases

Clay Mineralogy

The clay mineralogy was determined from sediments dispersed in distilled water using an ultrasonic probe (30 seconds). The less than 2 μm fractions were separated by settling, dried on glass slides at room temperature and then were solvated with ethylene-glycol vapour at 60°C overnight to ensure maximum saturation. In XRD traces of the clay fractions, both air dried (AD) and after ethylene glycol (EG) solvation, we collected data in the range 2–35° 2 θ with a step size of 0.02° and counting time 0.5 s per strip step (total time 31.8 s per step).

Complex diffraction maxima were deconvolved into the individual mineral phases peaks with the Fytik software [13]. The individual peak components were modeled with the Voigt function after subtraction of the background.

2.1 Clay fraction separation

The separation of clay fraction in samples was performed through the pipet method in order to identify and study the clay mineralogy. The method can be summarized in the following steps:

1. After crushing in sand size a representative part of each sample we add the material in plastic beaker of 250ml capacity, and we add 150-200 ml of distilled water.
2. Afterwards, we stir the suspension, disperse it with an ultrasonic probe for 30-60 secs and leave it to rest for an hour. If the floating particles flocculate, we remove the translucent water layer with a 25ml pipette, and we add distilled water. When the solution stabilizes, we disperse it again, and spread it with a dropper in two different glass slides.
3. After the evaporation, the clay fraction remains on the glass slides, and is used for mineral phases identification, thermal and glycol tests. In addition, we extract 25 mL from the surface layer of the solution (up to 1 cm deep), via a 25mL pipet, and we place this quantity into a 50mL test tube.
4. The next procedure, includes centrifugation at 8000 rpm for 10 minutes. Before this process, tubes in pairs are being weighed in precise weighing scale in order to be perfectly balanced, and after that, we are ready to place in the centrifuge. If the number of tubes is odd, we place a water tube instead opposite of our sample, after we weigh it, in order to be balanced.
5. Finally, the separated clay fraction is segregate on the tube walls, the supernatant is decanted and the clay fraction is dried, for further use.

2.2 Scanning Electron Microscopy with Energy Dispersive Spectroscopy (SEM-EDS)

Mineral textures and semiquantitative chemical composition of the clay minerals were determined with Scanning Electron Microscopy (SEM) from back-scattered electron (BSE) images.

Polished sections, of 14 samples collected from the profile in the Vrysakia deposit, were prepared in the E.A.G.M.E. laboratories.

The SEM-EDS analyses were carried out at the Faculty of Geology and Geoenvironment, National and Kapodistrian University of Athens (NKUA), using a JEOL JSM 5600 scanning electron microscope (Tokyo, Japan), equipped with ISIS 300 OXFORD automated EDS analysis system (Oxford shire, UK). Analytical conditions were 20 kV accelerating voltage, 0.5 nA beam current, ~3 µm beam diameter and 50 s counting times. Pure Co metal standard was used for calibration. The sections were coated with graphite film before the SEM study.

2.3 Geochemical analyses

Whole rock chemical analyses were conducted by ALS Global Geochemistry Laboratories by ICP-AES and ICP-MS methods.

ICP-AES was preferred for the major and minor elements, while ICP-MS technique was used for trace elements. The procedure that was followed involves lithium borate fusion prior to acid dissolution, that solubilizes most mineral species and provides a sufficient analysis approach for a broad suite of elements ([8]ALS Geochemistry Service Schedule, 2013).

Major and minor elements oxides are presented in wt (%) and trace elements in ppm. Nickel is presented here as oxide (%), but it was analyzed as trace element with special method (Ni-OG62), suitable for nickel laterite components. The Loss On Ignition (LOI) was calculated using a Thermo Gravimetric Analyzer (TGA).

3.Results

In order to present successfully mineralogical data and proceed to accurate observations we combined both PXRD and SEM-EDS analyses in bulk and clay mineralogy. Geochemical analyses were used mostly for determination of Ni and other critical metals content, and secondly for confirmation of mineralogical results.

3.1 Mineralogical and Textural Characteristics

Representative micrographs of polished blocks from Vrysakia deposit that were studied are shown in Fig.11.

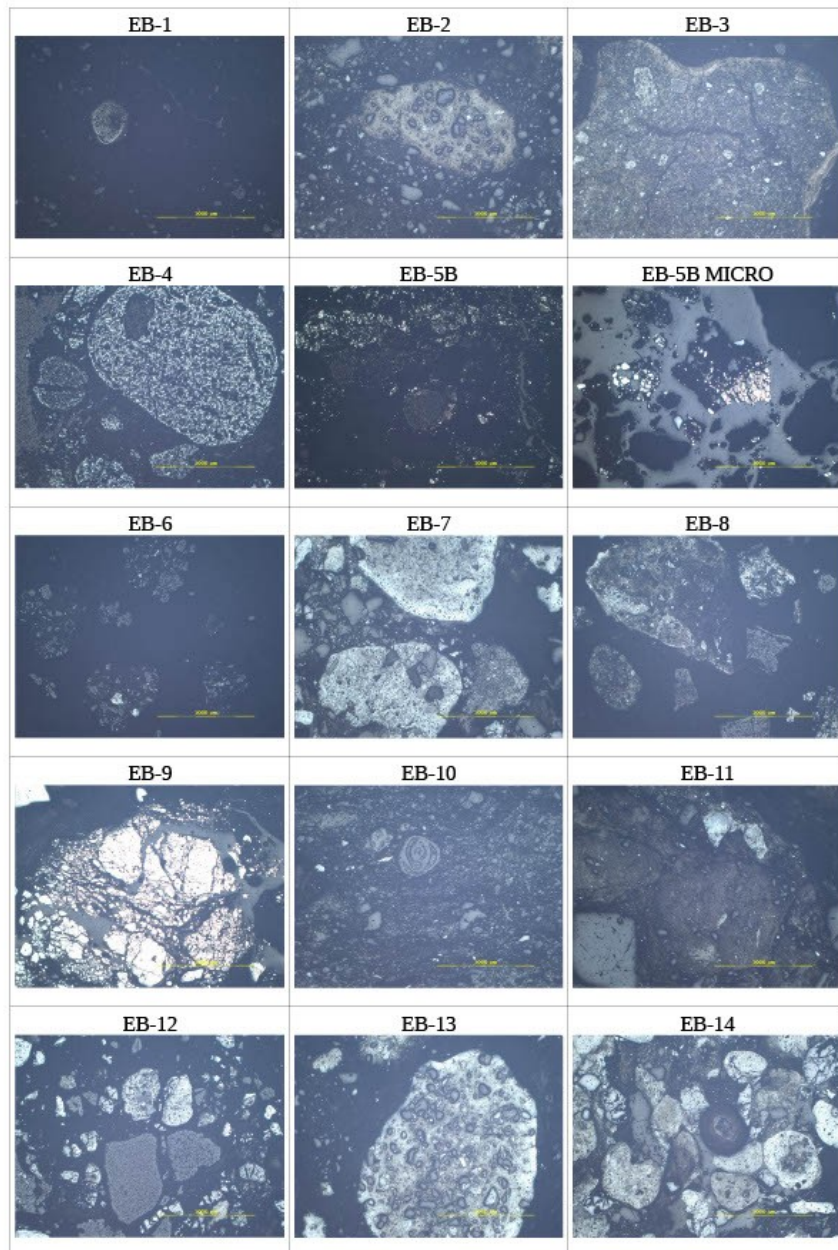


Fig.11: Micrographs from studied polished sections under metallographic microscope of the samples from Vrysakia deposit.

Description: EB-1: dense crypto-crystallic with a peloidal grain of hematite, EB-2: a weathered, peloidal grain of hematite with entrapped crystals of quartz, EB-3: complex grain of weathered hematite with inclusions of newly formed hematite and quartz, some crystals are peculiar, EB-4: a weathered, rounded grain of hematite, EB-5: micro-krypto krystallic mass with residuent structure, EB-5 MICRO: sulfides, disintegrated, inside a quartz grain (same sample with EB-5 in smaller grain size), EB-6: quartz grains, disintegrated, weathered with minor hematite, EB-7: hematite grains with angular and rounded fragments of quartz, EB-8: angular and rounded grains of goethite and hematite peloids, EB-9: disintegrated crystals with intense reflectiveness wich represent

sulfides, growth of quartz microveins, EB-10: mylonitic-like, disintegrated texture with possible fossil of quartz composition, EB-11: grain of chromite (almost idiomorphic), hematite peloid with fragments of quartz, EB-12: angular grains of hematite and goethite, EB-13: rounded grain of hematite with quartz fragments in hive texture, EB-14: pissolithic-oolithic rounded grains of hematite

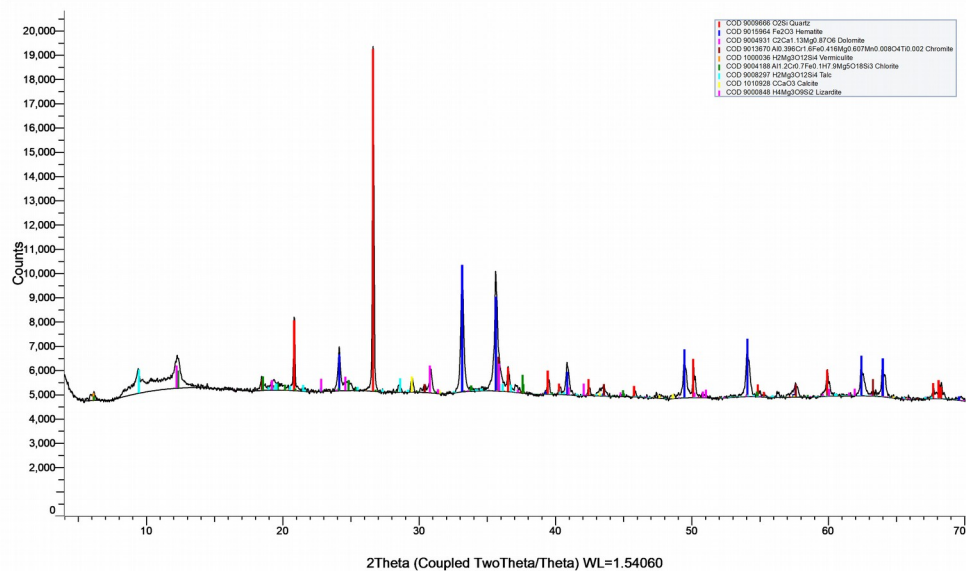
The samples consist of complex grains (peloids, pisolites) and individual grains of hematite as a basic component. They also contain quartz, goethite and a few grains of chromite. Angular and rounded grains, especially of quartz or hematite, coexist in many samples suggesting that the ore has been transported at a short distance from the parent rock or that there are other sources that supply the ore with grains (which are angular), except the parent rock. Due to the presence of pisolites/oolites, we can also assume that the paleoenvironment of ore's formation, at least at some point, was a shallow sea water basin. The texture is often characterized by signs of erosion, fragmentation and substitution.

3.1.1 Bulk Mineralogy

The deposits are characterized both by pisolitic and pelitic textures. They consist of complex (peloids, scarce pisoids) and individual grains of hematite with variable sphericity (angular to rounded) as basic component, embedded in a groundmass of clay minerals and Fe-oxides/oxyhydroxides. They also contain angular to rounded quartz and calcite, magnetite, accessory chromite fragments and trace pyrite. The texture of the main phases indicates limited transportation from the sources.

The bulk phyllosilicate mineralogy is comparable in all deposits, regardless of the ore texture. The main phases are a 14 Å phase with a broad diffraction maximum centered at $\sim 6^\circ 2\theta$. A second weaker maximum occurs at $\sim 12.5^\circ 2\theta$. These features are indicative of a chlorite-bearing phase. Talc (kerolite-pimelite) is a minor phase in many samples, being a major phase in sectors of the Vrysakia deposit (EB-8, EB-10). Smectite was identified as a major phase in sectors of the Vrysakia, Platani, Pagondas and Rekavetsi deposits, while discrete illite was identified in one sample from Vrysakia (EB-9) and on Katzikiza and Rekavetsi deposits (EB-21, EB-26, EB-27A, EB-27B). The d_{060} of smectite varies between 1.506 and 1.513 suggesting a Fe-rich dioctahedral variety, similar to the smectite in Lokris ([29]Christidis & Skarpelis, 2010). The $d_{(060)}$ values depend on the composition of the octahedral sheet, the amount of Al in the tetrahedral coordination and the degree of tetrahedral tilt ([86]Moore & Reynolds, 1989). Serpentine is present as a minor phase or traces in almost all samples from Vrysakia and Platani deposits.

EB5A Bulk (Coupled TwoTheta/Theta)



EB26 Bulk (Coupled TwoTheta/Theta)

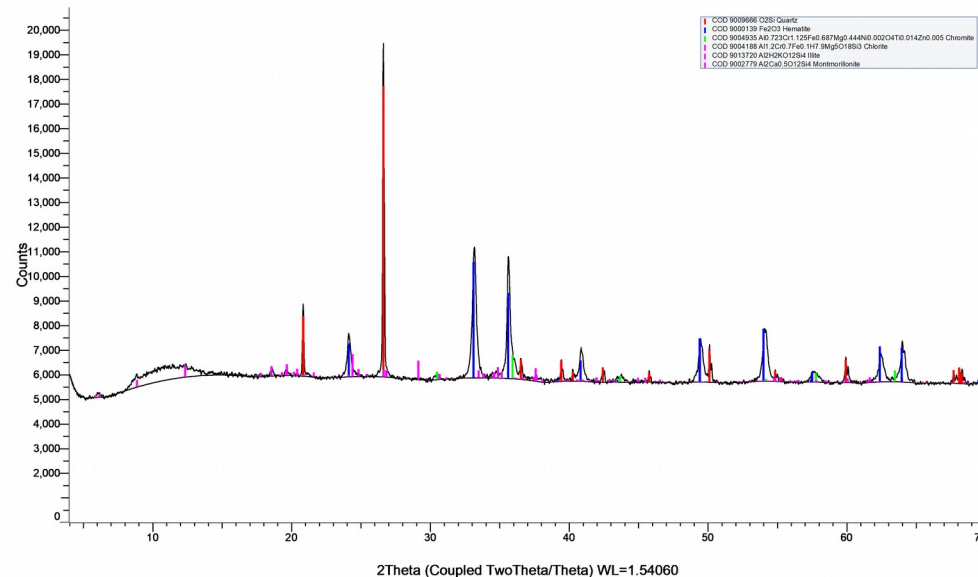


Fig.12: 2 PXR D patterns showing occurrence of talc and discrete illite together with chlorite, quartz, hematite, chromite in samples of Vrysakia and Rekavetsi, respectively

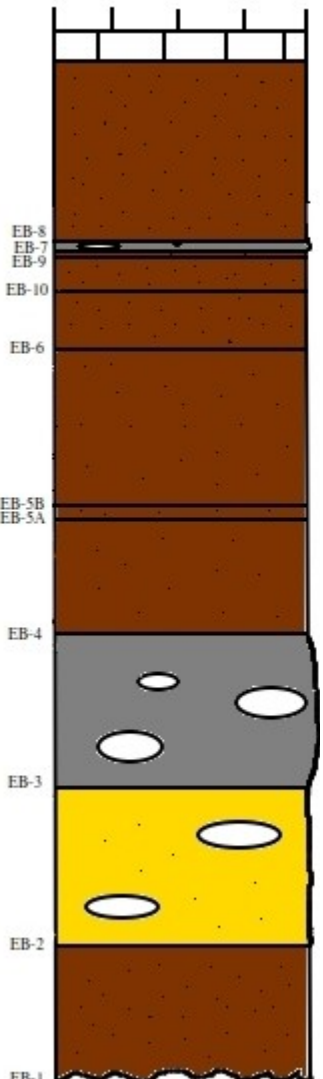
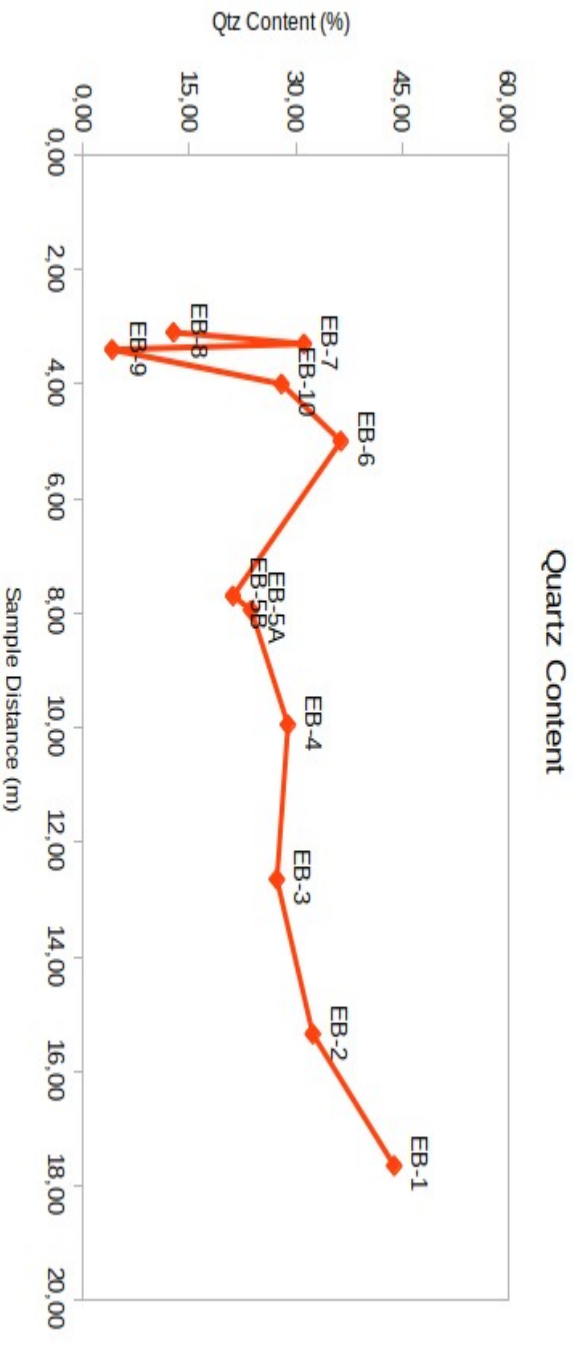
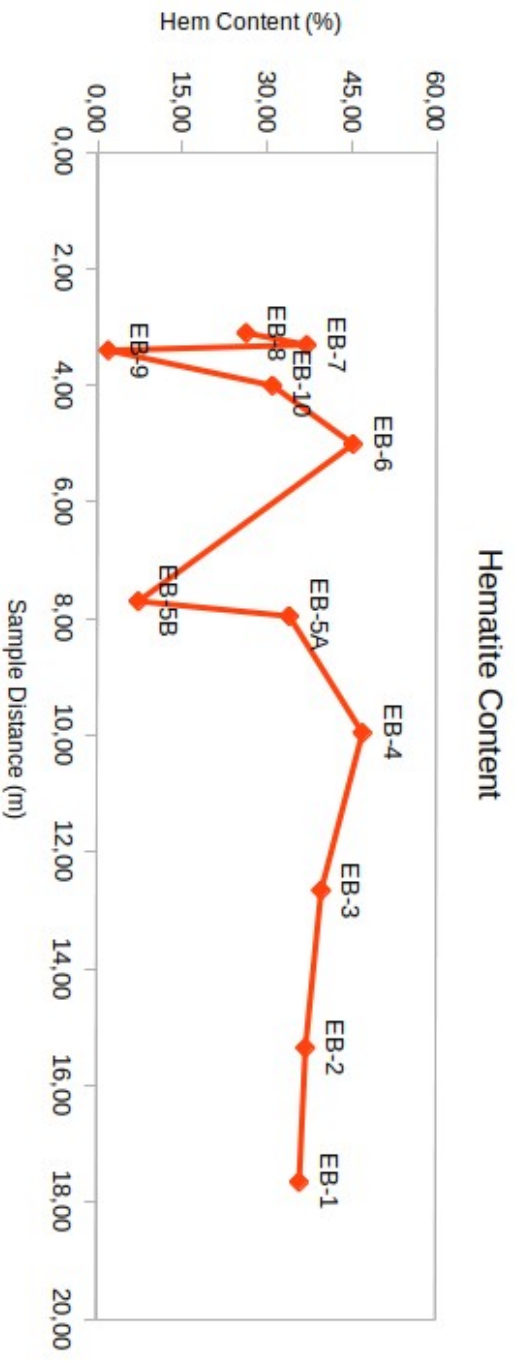
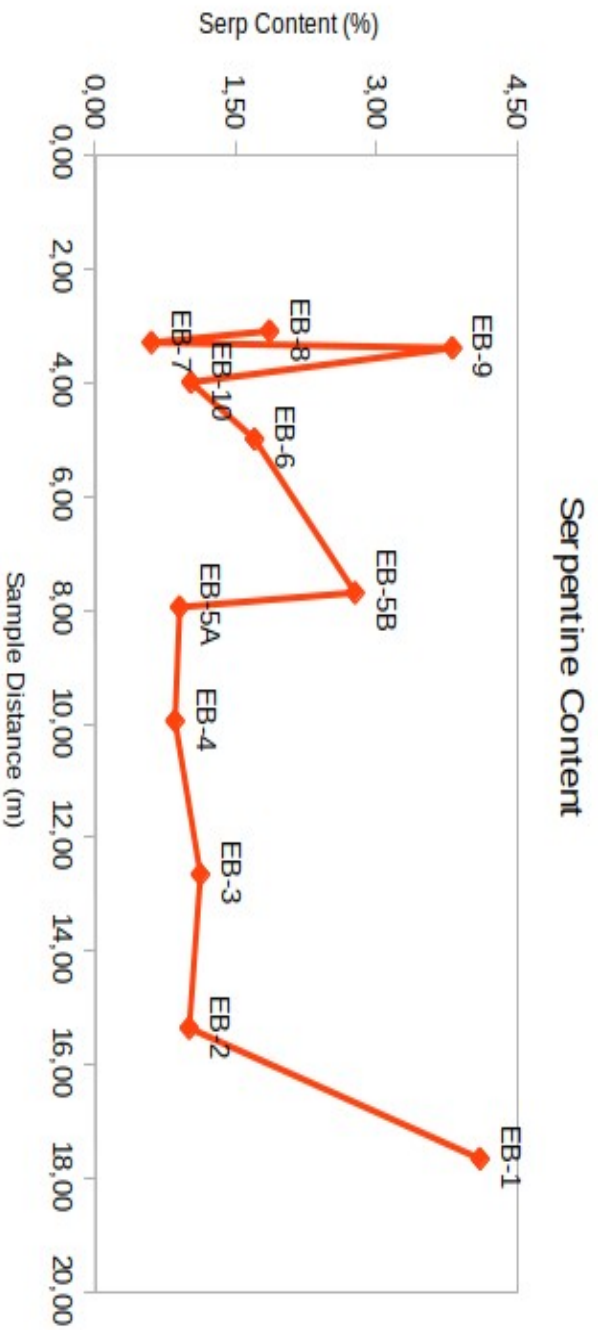
The PXR D patterns also, show the presence of minor phases and trace minerals such as spinel, amphibole, rutile, kaolinite, dolomite, possible todorokite, gypsum and anhydrite together with major pyrite (EB-5B).

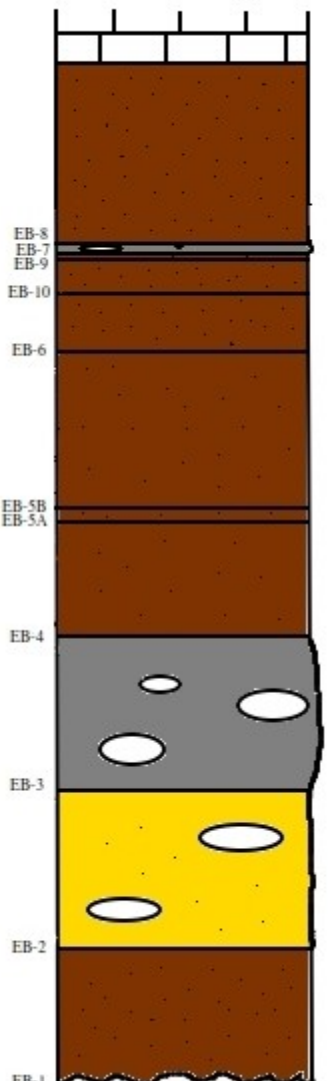
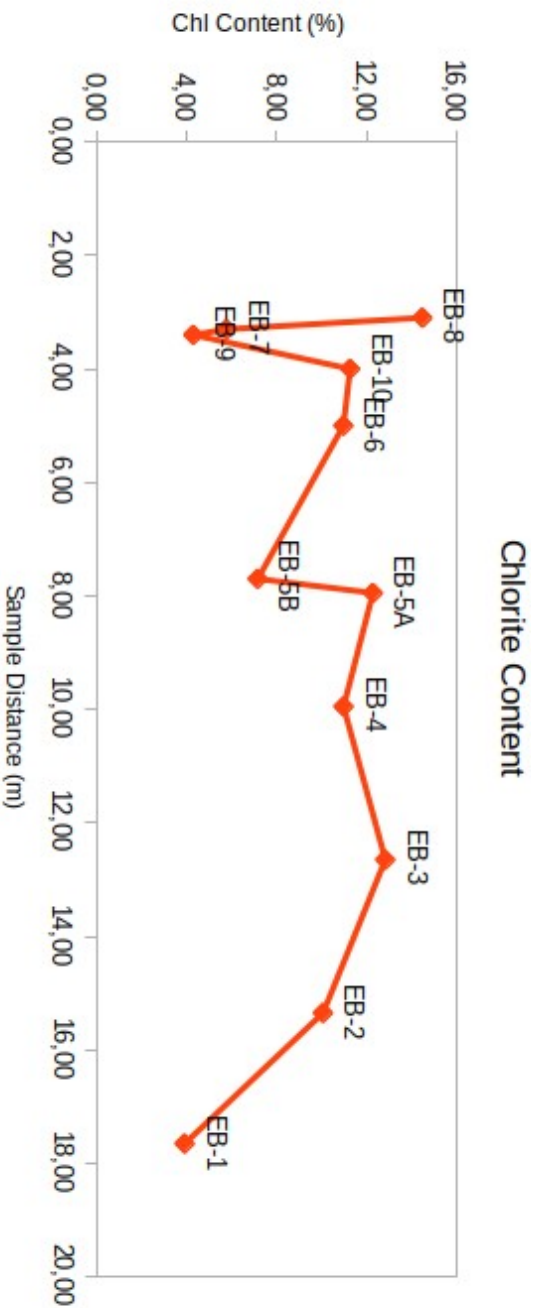
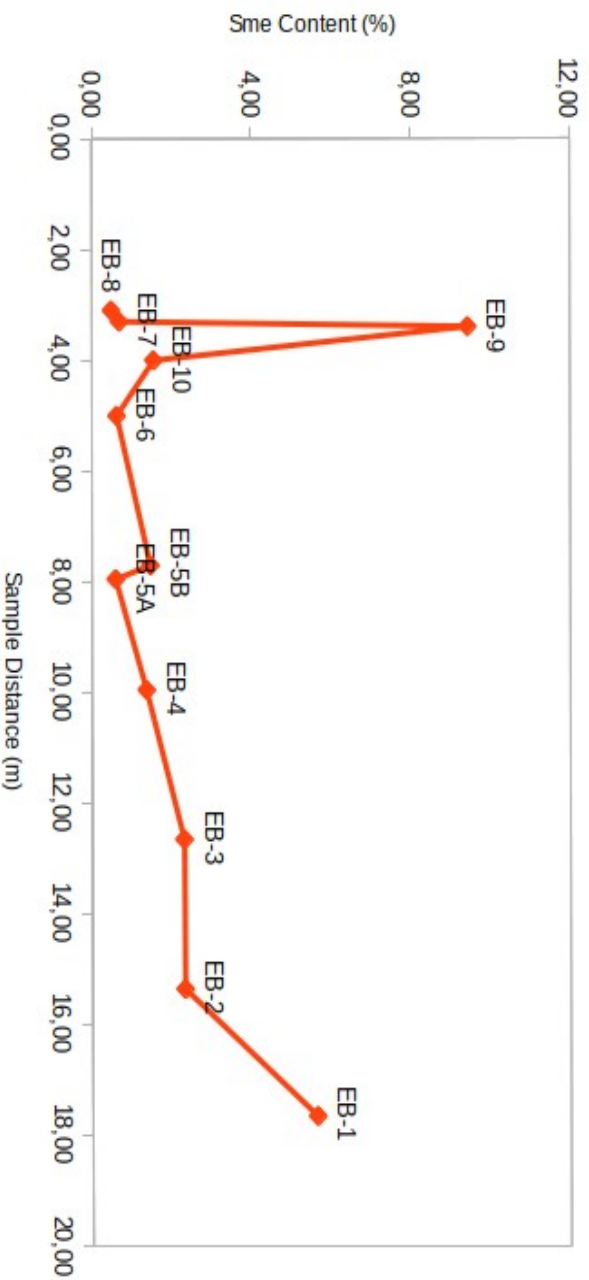
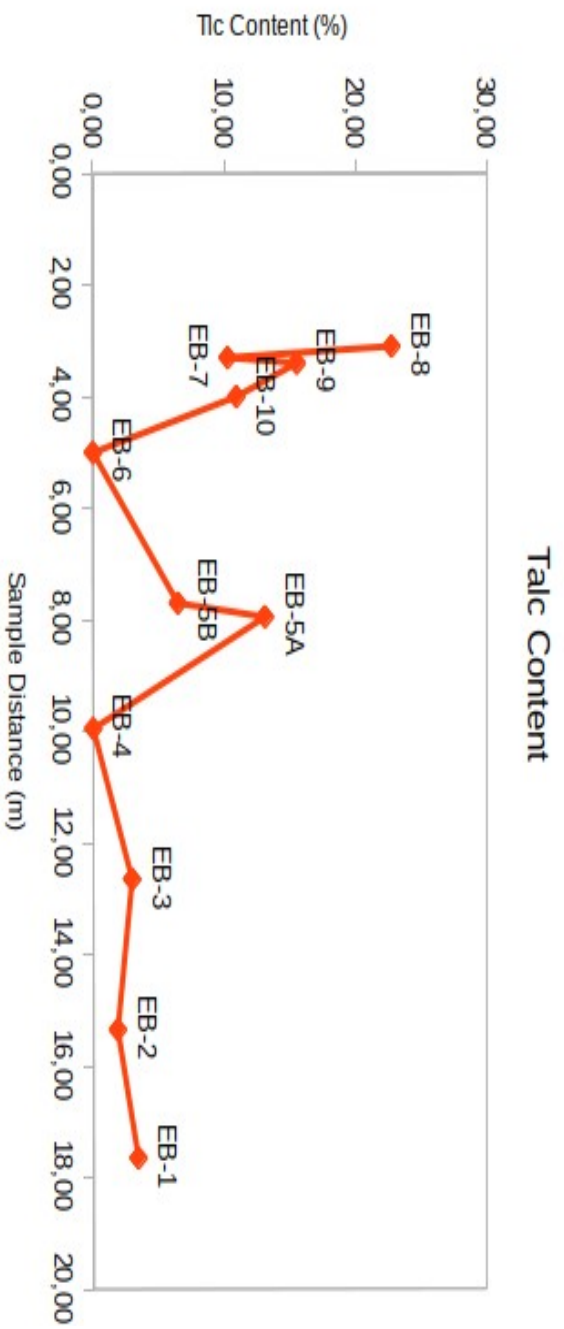
Quantitative analysis of all samples from PXRD patterns with the AutoQuan software:

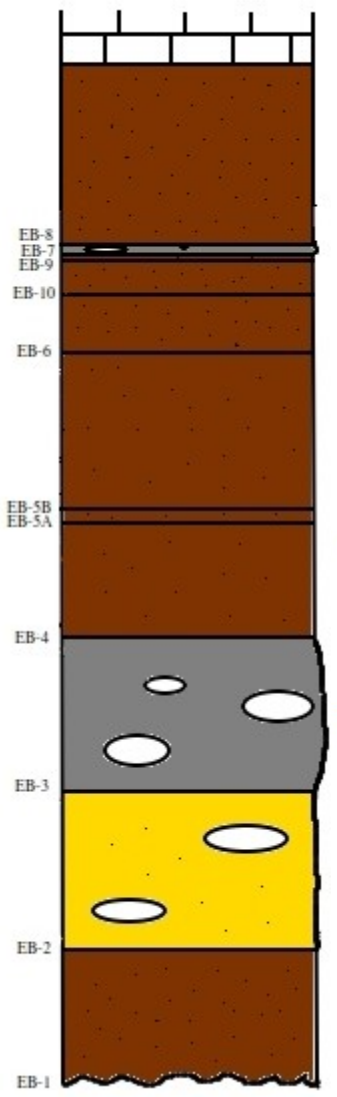
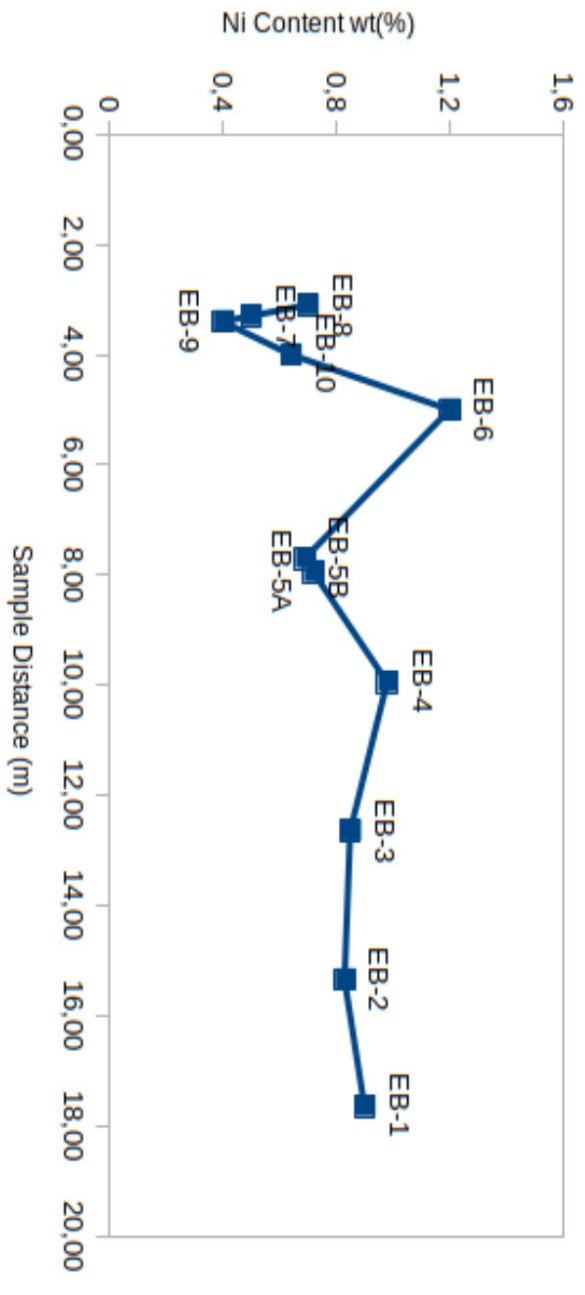
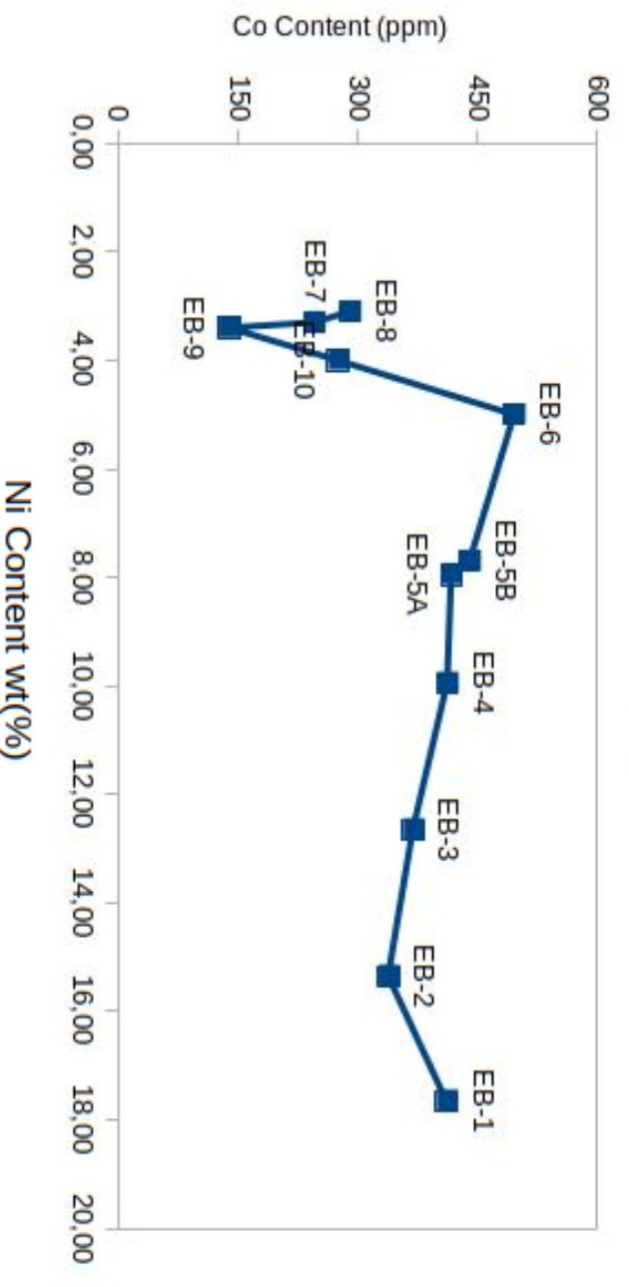
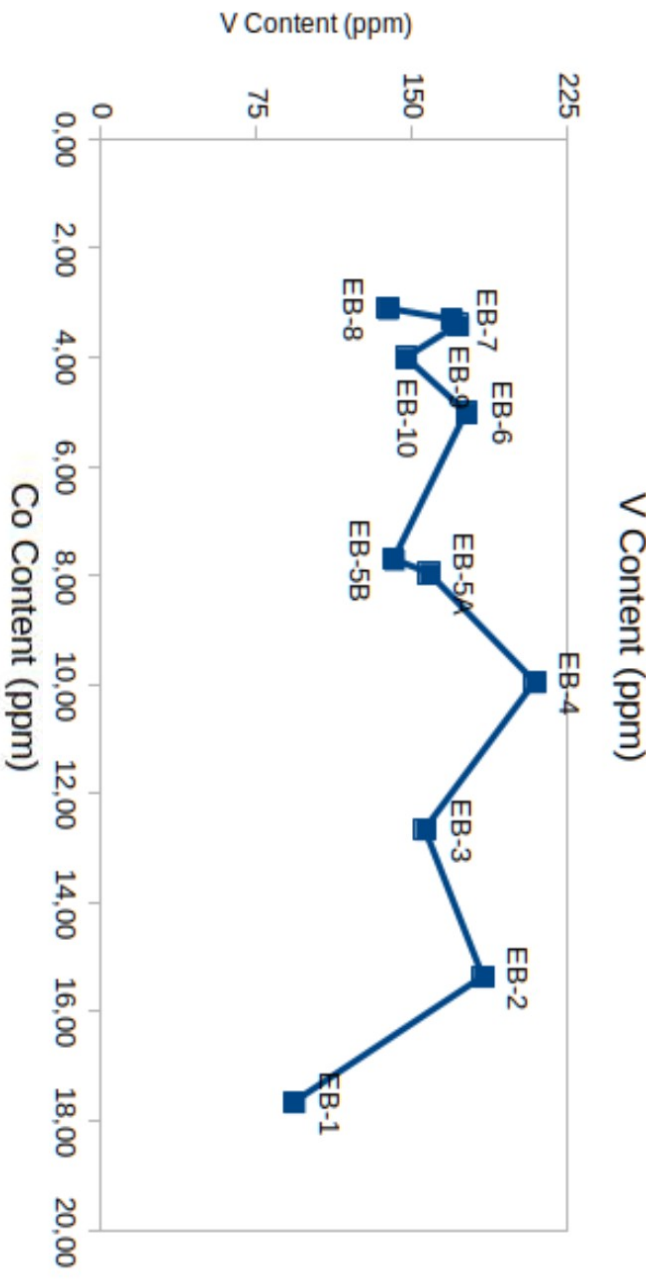
wt %	EB-1	EB-2	EB-3	EB-4	EB-5A	EB-5B	EB-6	EB-7	EB-8	EB-9	EB-10	EB-11	EB-12	EB-13	EB-14	EB-15	EB-16	EB-17	EB-18A	EB-18B	EB-19	EB-20	EB-21	EB-22	EB-23	EB-24	EB-25	EB-26	EB-27A	EB-27B	
Rwp%	2,4	2,2	2,1	2,1	2,2	2,4	2,1	2,1	2,4	2,7	2,4	2,0	2,3	2,3	2,2	2,3	2,2	2,0	2,1	3,3	2,2	2,0	2,5	2,3	2,1	2,1	2,1	2,3	2,9	3,0	
Qtz	43,9	32,4	27,3	28,9	23,7	21,2	36,4	31,2	12,8	4,1	28,0	31,9	29,4	40,7	20,9	36,8	21,8	32,9	31,8	0,7	20,7	34,1	41,9	39,5	34,6	25,6	27,7	29,8	28,7	24,7	
Hem	35,9	37,0	39,7	47,0	34,0	7,3	45,2	37,0	26,3	1,9	31,0	46,5	32,4	39,1	42,3	37,5	44,4	47,0	42,3	1,3	50,6	55,1	43,4	48,0	46,7	53,1	55,5	56,4	0,8	14,7	
Chl	3,9	10,1	12,8	11,0	12,3	7,2	11,0	5,8	14,5	4,3	11,3	9,7	8,3	13,0	3,1	10,3	8,0	9,4	14,0	16,4	18,1	4,6	4,5	5,7	11,8	10,1	10,8	3,4	20,4	20,3	
Sme	5,6	2,3	2,3	1,4	0,6	1,5	0,6	0,7	0,5	9,4	1,6	0,7	1,0	1,1	2,0	0,9	1,0	4,5	0,8	4,9	1,2	0,9	1,1			0,6	0,7	0,2	6,5	3,4	
Liz	4,1	1,0	1,1	0,9	0,9	2,8	1,7	0,6	1,9	3,8	1,0	0,7	2,8	1,3	4,8	3,2	3,3	0,8	4,0	0,8	4,9	5,9	4,1			4,0	4,7	1,4		3,1	
Tlc	3,4	1,8	2,9		13,1	6,5		10,3	22,8	15,5	10,9	4,1	2,5	3,7	6,7			4,3	6,8		1,1									3,8	
Cal		8,0	6,5	3,4	5,7	4,2		3,5	3,3	1,7	11,4	4,8	15,0	2,0	11,4	3,7	4,9		4,2				1,6	1,6						1,4	
Chr	0,9	5,3	7,3	7,5	11,3	4,7	3,6	4,4	10,6		3,2	4,8	7,2	2,7	9,3	7,7	16,6	0,9	2,5	1,3	5,2	0,9	3,2	5,2	1,4	3,9	3,7	7,1	1,6	1,8	
Pyr						34,2				2,2																			15,5	2,0	
Gyp						6,2	1,6			1,4									0,3			0,6				2,0			2,1	1,1	
Rut											0,3	1,3	1,1	0,9	0,8				0,2	1,7										0,7	
Plag										12,6											43,7										
Dol					7,0	3,2		6,5	4,0																						
Anh						1,2																									
Goe											24,7																				
ill										26,2													4,1					3,1	1,7	19,7	
Spn	1,1	0,1								1,0				0,2				0,2	0,5			0,2	0,4								
Kao															1,2					0,6									5,7		
Amp									6,9		1,7									3,8											
Mel																													10,0		
Mar																													3,8		
ilm										0,5															1,4		0,3				
Gib																															
Tit																															3,0
Zir																															6,8
Mgn									3,1			1,1	1,6																		0,6
Mon										1,7																					
Pyro																					13,4										
Micr																					6,3										
Tit																					3,0										

Table 2: Description of names Qtz=quartz, Hem=hematite, Chl=chlorite, Sme=smectite, Liz=lizardite, Tlc=talca, Cal=calcite, Chr=chromite, Pyr=pyrite, Gyp=gypsum, Rut=rutile, Plag=Plagioclase, Dol=dolomite, Anh=anhydrite, Goe=goethite, ill=illite, Spn=spinel, Kao=kaolinite, Amp=Amphibole, Mel=melanterite, Mar=marcasite, ilm=ilmenite, Gib=gibbsite, Tit=titanite, Zir=zircon, Mgn=magnetite, Mon=monazite, Micr=microcline, Pyro=Pyroxene

Quantitative mineralogical data show that hematite is major phase in all samples. Among the phyllosilicate minerals, chlorite is dominant phase while, smectite layers predominate over chlorite layers in only 2 samples (EB-1, EB-9). Sample EB-18B is part of the schist-chert-sand-stone formation and can be characterized as altered peridotite, which have underwent albitization, chloritization and possibly low-grade metamorphism. Below, follows a graphical presentation of some major phases and critical metals content along the Vrysakia section:







The section represents the stratigraphic sequence of Vrysakia deposit along the lens-form Fe-Ni ore, with EB-1 being closest to Cenomanian unconformity and EB-8 on top close to Upper Cretaceous limestones. Generally, it is difficult to discern a trend of phase content along the depth. Nevertheless, there seems to occur a gradual increase of quartz content with increasing depth. Moreover, it seems that chlorite's content tends to decrease downwards, with some fluctuations, while smectite's content increases over depth. Also, smectite presents the highest content in sample EB-9, while chlorite presents its lowest content. As for critical metals content, nickel and cobalt seem to present a similar distribution, almost steady in depth, with a steep decrease upwards, above sample EB-6. Vanadium's content distribution seems irregular without any trend.

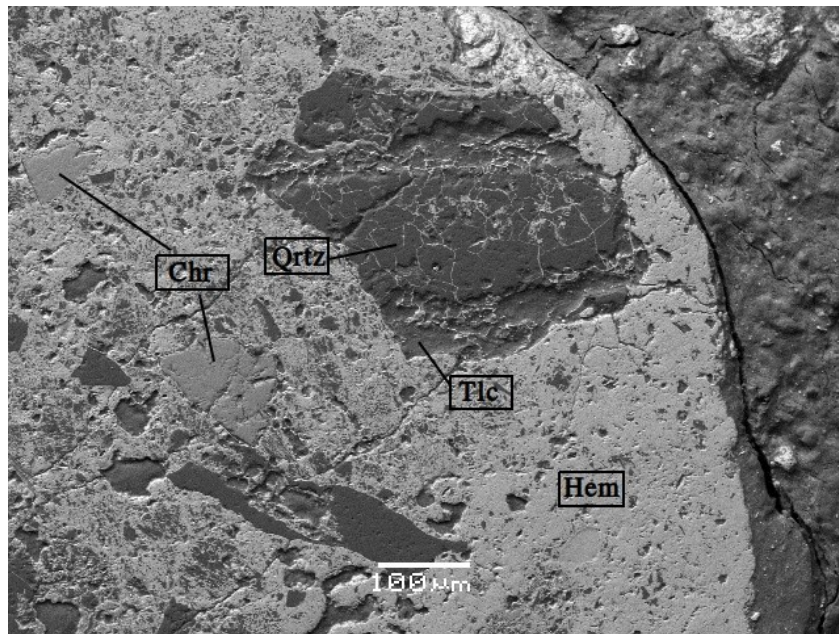


Fig.13: SEM micrograph from the Vrysakia deposit. Chr=chromite, Hem=hematite, Qrtz=quartz, Tlc=talca. Pisoid grain.

As for sulfide minerals, except from abundant pyrite in sample EB-5B, galena (PbS) was also identified:

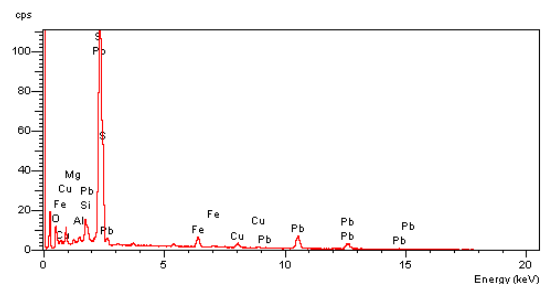
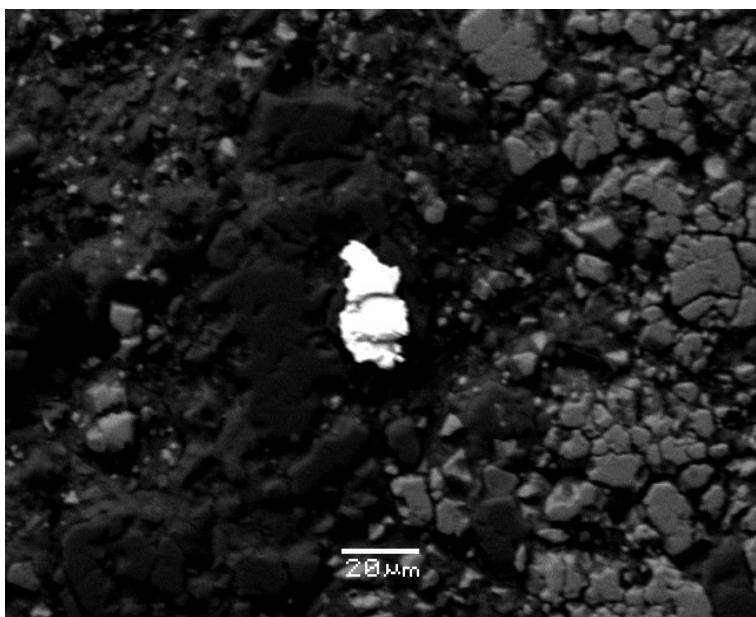


Fig.14: SEM micrographic from Vrysakia deposit. Galena grain (left) and SEM-EDS spectrum (right).

3.1.2 Clay mineralogy

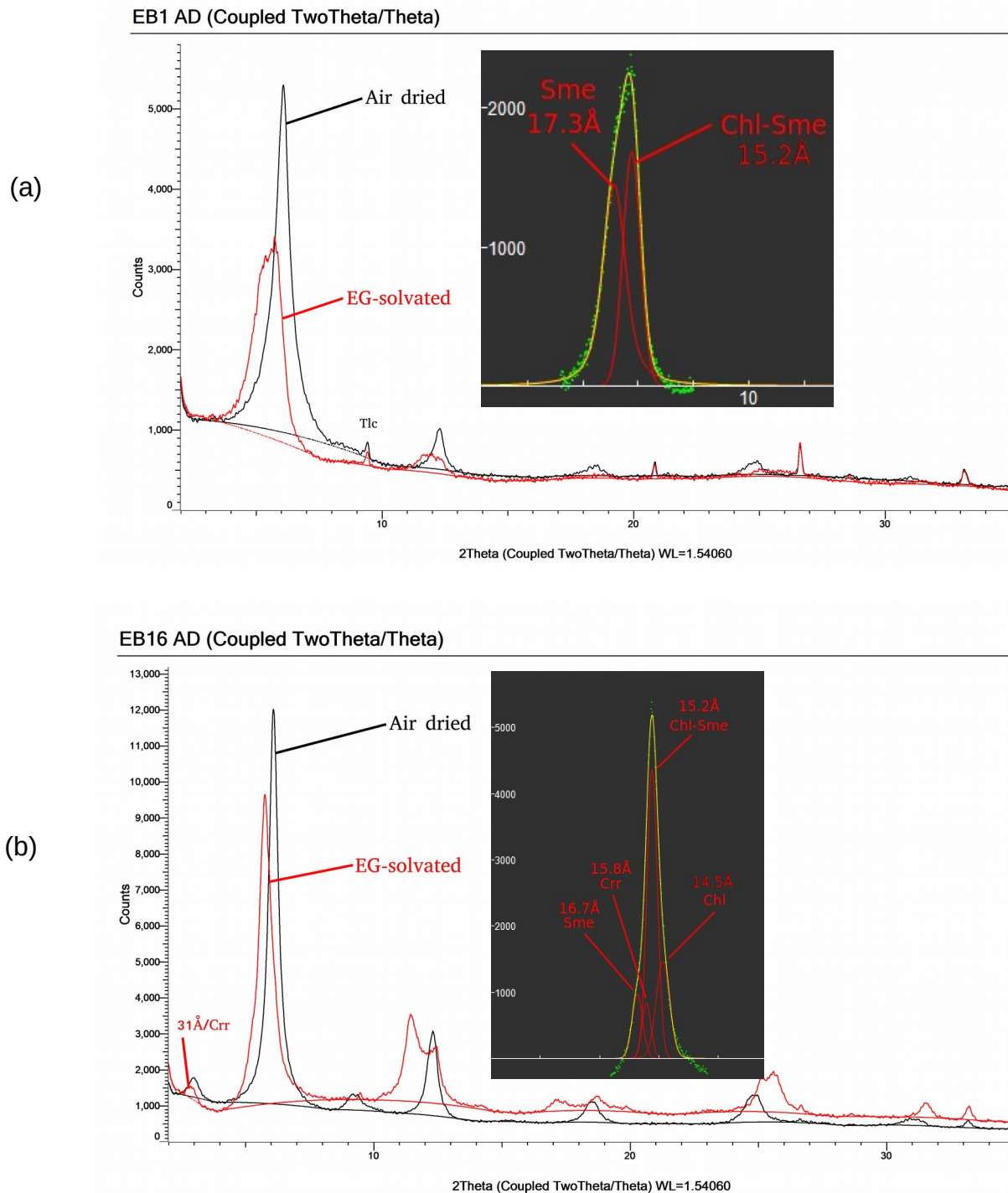
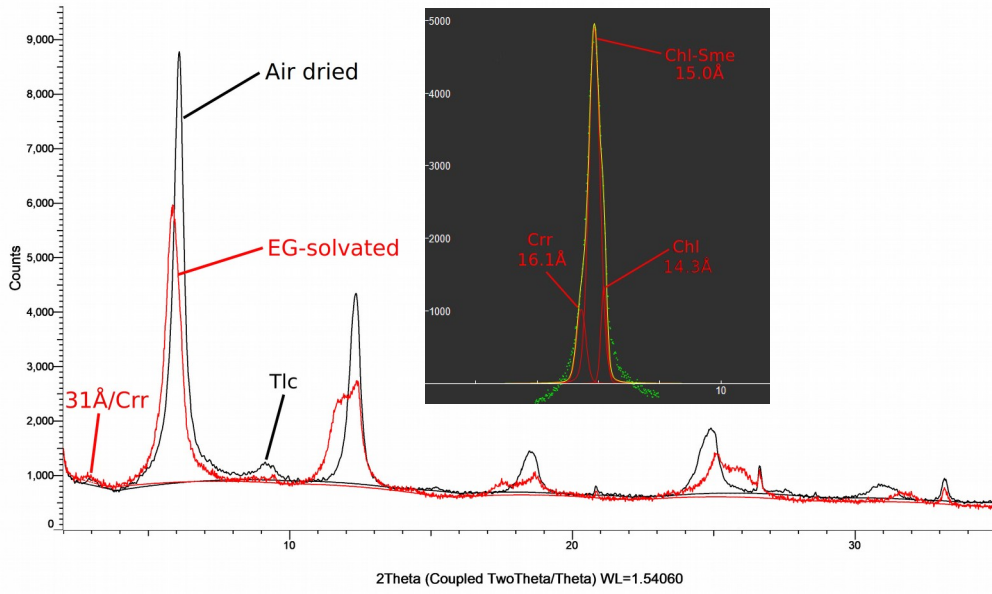


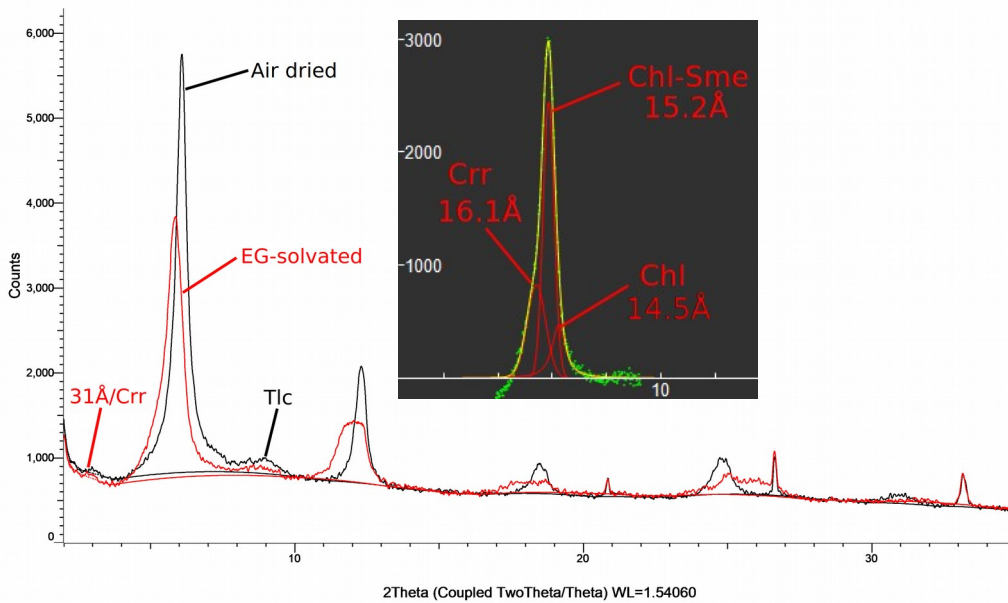
Fig.15: XRD traces of representative samples of oriented 2 μ m clay fractions from (a) the Vrysakia deposit with coexistence of talc with abundant discrete smectite and R0 mixed layered chlorite-smectite (Sme, Chl-Sme) and (b) from sample of Platani deposit with coexistence of corrensite (Crr, R1 mixed layer chl-sme), discrete smectite(Sme), R0 mixed layered Chl-Sme and discrete chlorite(Chl). The mineral symbols are after Warr (Warr, 2020).

EB11 AD (Coupled TwoTheta/Theta)



(a)

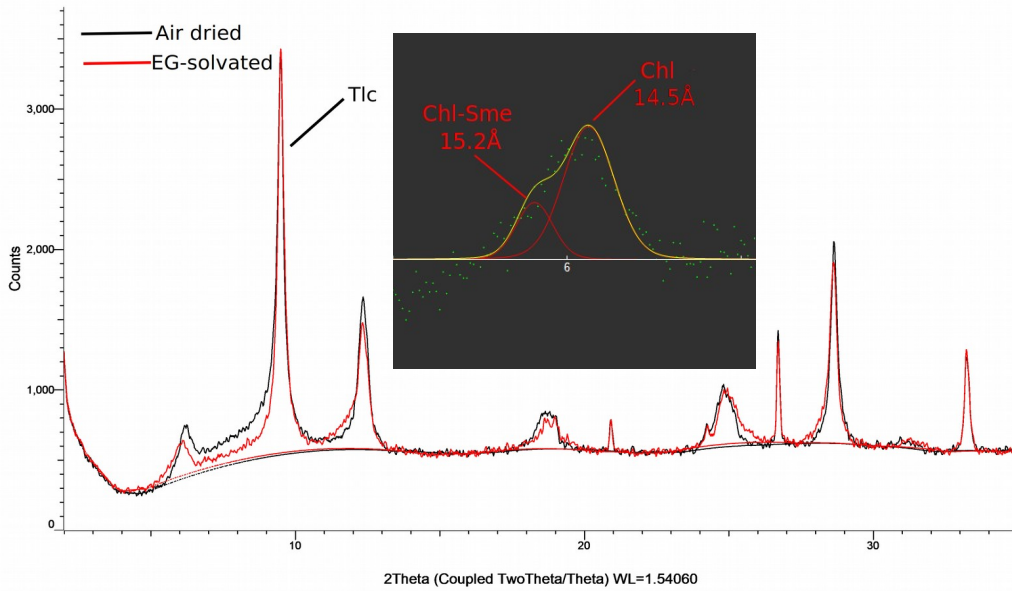
EB15 AD (Coupled TwoTheta/Theta)



(b)

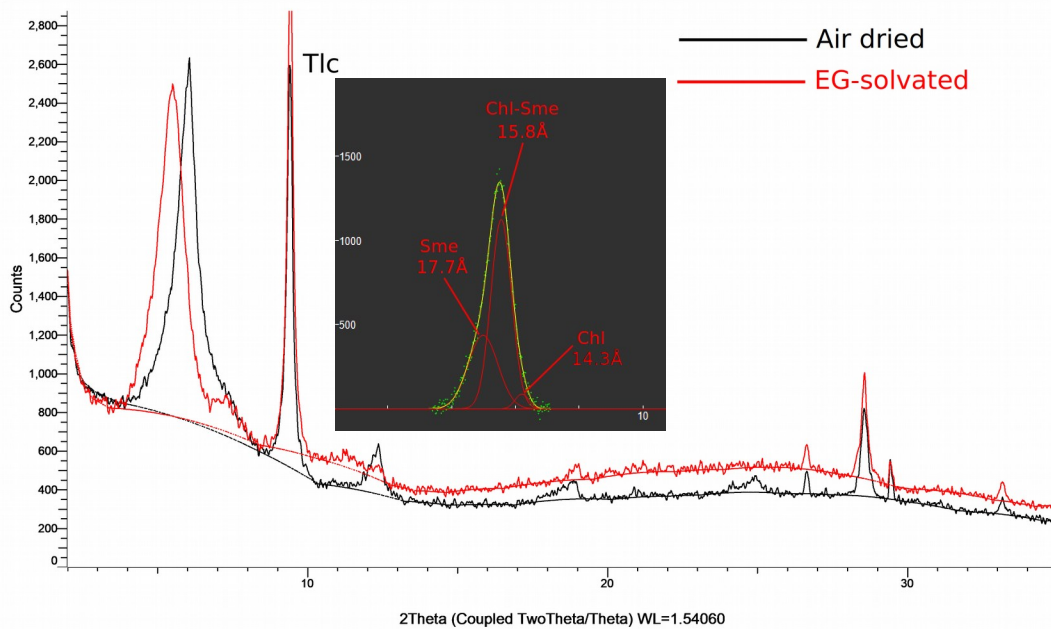
Fig.16:(a),(b) Peak at $2\theta=5.9^\circ/d=15.0\text{\AA}$ analyzed into 3 phases shows coexistence of corrensite (Crr) with talc(Tlc), R0 chlorite-smectite(Chl-Sme) and discrete chlorite(Chl) in samples EB-11, EB-15 of Vrysakia deposit

EB8 AD (Coupled TwoTheta/Theta)



(a)

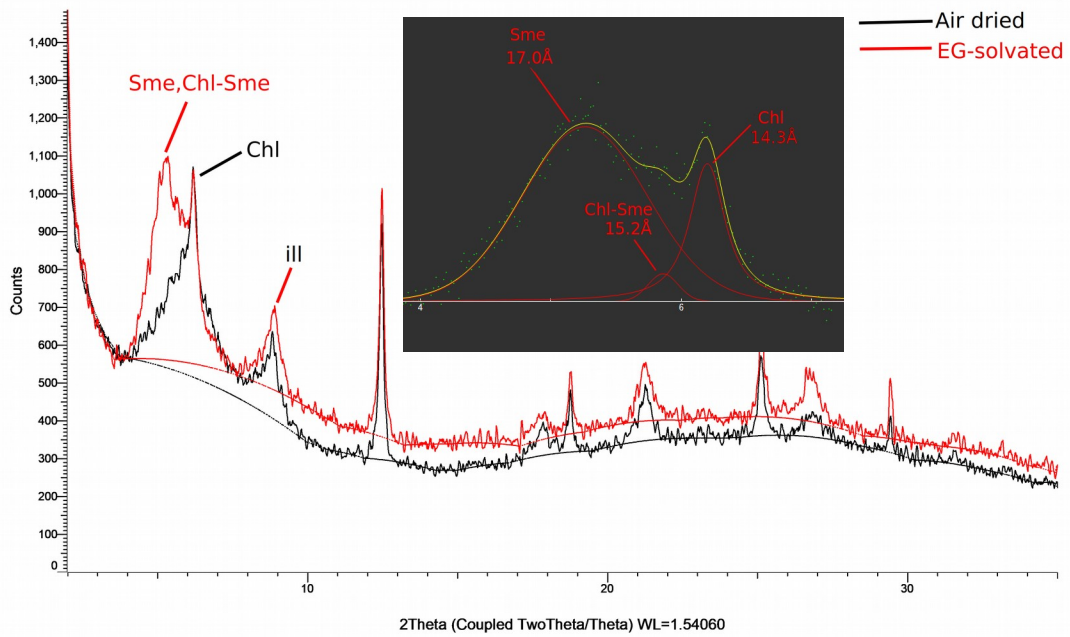
EB10 AD (Coupled TwoTheta/Theta)



(b)

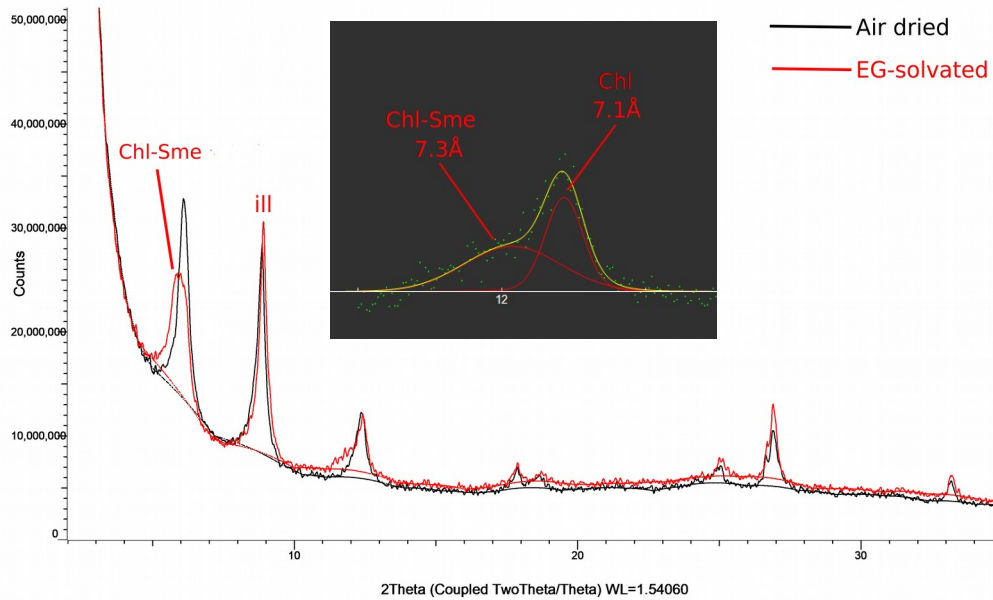
Fig.17:(a) Peak at 14.7 Å analyzed into 2 phases shows that abundant talc(Tlc) coexists with discrete smectite(Sme) and R0 mixed-layered chlorite-smectite(Chl-Sme) in sample EB-8. (b) Peak at 16.1 Å analyzed into discrete smectite(Sme), R0 mixed-layered chlorite-smectite(Chl-Sme) and discrete chlorite(Chl), which coexist with talc(Tlc) in sample EB-10.

EB9 AD (Coupled TwoTheta/Theta)



(a)

EB26 AD (Coupled TwoTheta/Theta)



(b)

Fig.18: (a) Peak at 15.5 Å analyzed into 3 phases shows coexistence of discrete smectite(Sme), R0 mixed layered chlorite-smectite(Chl-Sme) and discrete chlorite(Chl) with illite in sample EB-9 from Vrysakia deposit. (b) Peak at 7.1 Å analyzed into 2 phases shows coexistence of abundant

illite(ill) with R0 mixed layered chlorite-smectite(Chl-Sme) and discrete chlorite(Chl) in sample EB-26 from Rekavetsi deposit.

The clay fraction patterns show the predominance of a 14-14.5/7 Å phase, while talc is also abundant in many samples. In sectors of Vrysakia and samples of Platani deposits corrensite (Crr) is also present. Samples EB-1 and EB-9 from Vrysakia contain abundant discrete smectite, as well as other samples do, but in smaller amounts. In EG-solvated samples complex diffraction peaks at 14.0-15.0 Å are analyzed in 3 or 2 different phases, at ~17 Å discrete smectite (Sme), ~15.3 Å, R0 mixed layered chlorite-smectite (Chl-Sme), and ~14.3 Å, which corresponds to discrete chlorite (Chl). Corrensite occurs at ~16.0 Å (2nd peak) and may coexist with the aforementioned phases(Fig.15b). Similarly, the diffraction maximum at 7 Å is analyzed in 2 components, corresponding to R0 mixed layered chlorite-smectite(7.3 Å) and discrete chlorite(7.1 Å)(Fig.18b). There is also abundant illite in sectors of Rekavetsi and Vrysakia deposits (Fig.18).

3.2 SEM-EDS analyses

wt%	Chlorite			Chlorite-smectite mixed R0		Smectite		
	EB-1	EB-8	EB-9	EB-1		EB-8	EB-10	EB-1
MgO	18,31	18,44	9,19	15,46	7,20	17,58	23,99	8,94
Al ₂ O ₃	11,21	10,90	19,50	12,50	8,50	1,81	3,84	10,97
SiO ₂	39,58	36,65	33,81	43,90	44,74	57,03	52,83	49,22
CaO	-	0,51	-	1,18	-	0,35	0,82	-
SO ₄	-	-	1,51	-	-	0,73	-	-
K ₂ O	-	-	2,69	-	-	-	-	-
FeO	10,42	14,42	15,02	11,11	24,63	7,54	4,24	11,93
NiO	4,29	2,11	-	-	1,24	2,07	0,87	3,59
Total	83,80	83,03	81,72	84,16	86,31	87,11	86,59	84,65

wt%	Serpentine			Talc		Illite		
	EB-10	EB-1	EB-8	EB-1		EB-9		
MgO	12,00	7,20	29,51	30,64	32,73	3,67	2,95	3,40
Al ₂ O ₃	7,70	8,50	-	-	1,75	25,24	24,55	26,30
SiO ₂	40,75	44,74	62,01	62,44	59,50	57,93	53,86	56,51
CaO	1,22	-	-	-	-	0,23	-	-
SO ₄	-	-	-	-	-	2,16	1,52	1,56
K ₂ O	-	-	-	-	-	7,25	8,31	8,17
FeO	24,28	24,63	6,02	2,65	1,76	3,53	3,70	4,10
NiO	1,40	1,24	-	1,70	-	-	0,49	0,40
Total	87,35	86,31	97,55	96,43	95,74	100,00	95,38	100,90

Table 3: Representative Micro-analyses of Vrysakia ferronickel samples. Microprobe analyses are semi-quantitative, they don't represent distinct clay mineral phases and are indicative of the reported phases

After studying SEM-EDS semiquantitative results and back-scattered electron (BSE) images from Vrysaki polished sections samples, we ascertained that main nickeliferous phases are Ni-chlorite, Ni-smectite and to a lesser degree Ni-talc and serpentine. Moreover, most SEM-EDS analyses of phyllosilicate minerals do not represent pure phases, but clay minerals mixed with quartz and probably Fe-oxides/oxyhydroxides. Therefore we can explain the high values (compared to the literature for the region, i.e. Mposkos, 1996) of SiO₂ in analyses of chlorite and mixed-layered chlorite-smectite. The identification of chlorite and other phyllosilicate mineral as discrete phases is probably beyond the capabilities of the instrument because of the fine grain size and dense, cryptocrystalline groundmass.

Trace mineral phases SEM-EDS:

Galena		Mg-Chromite	
wt%	EB-5B	wt%	EB-5B
Mg	0,62	MgO	12,57
Al	0,54	Al ₂ O ₃	18,89
Si	1,70	Cr ₂ O ₃	48,54
S	15,70	FeO	17,11
Fe	3,55		
Cu	2,52		
Pb	50,38		
Total	75,02	Total	97,12

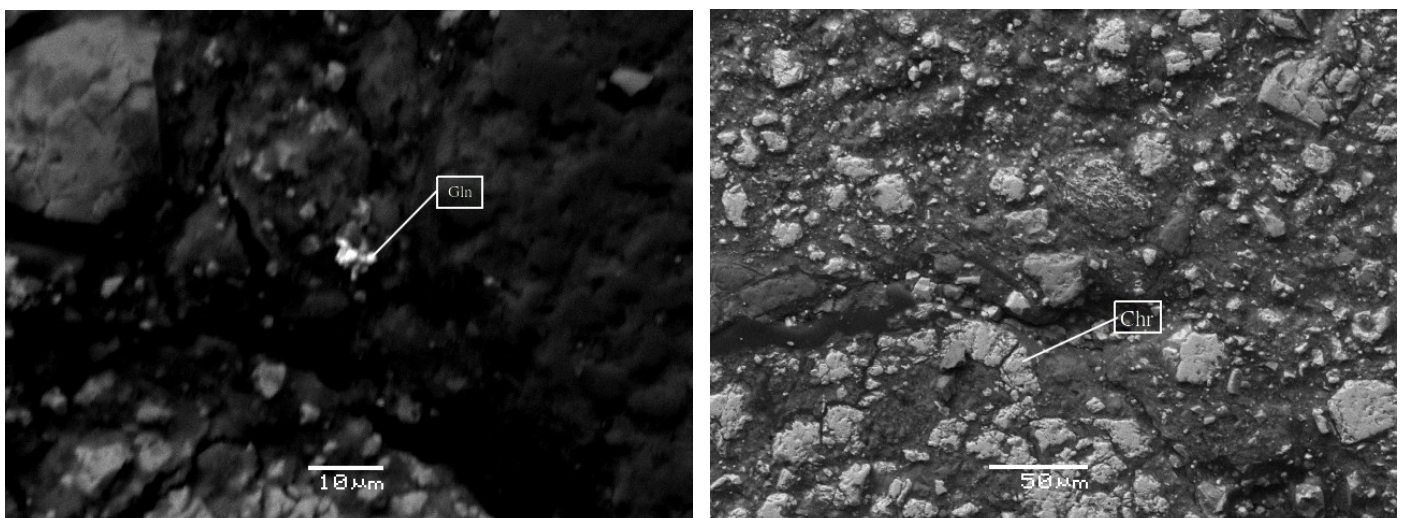


Fig.19: SEM micrographes of Chr=chromite right and Gln=galena left

3.3 Chemical analyses

The ICP-OES/MS chemical analyses provided us to useful information, on the geochemistry of samples and the relationships between certain chemical elements. The analyses refer to samples of the Vrysakia deposit collected along a vertical and horizontal profile.

In particular, Ni content is correlated to the Co content (Fig.20), but not to the V content. Ni content, in general, remains constant ~1 wt%, except for some positive peaks in EB-6 or EB-4 samples (Table 4). Moreover, Zn and V content show a very strong correlation in all samples (Fig.22 m).The Cr₂O₃ content distribution is more irregular than the NiO content, following the dissemination of detrital chromite grains in samples.

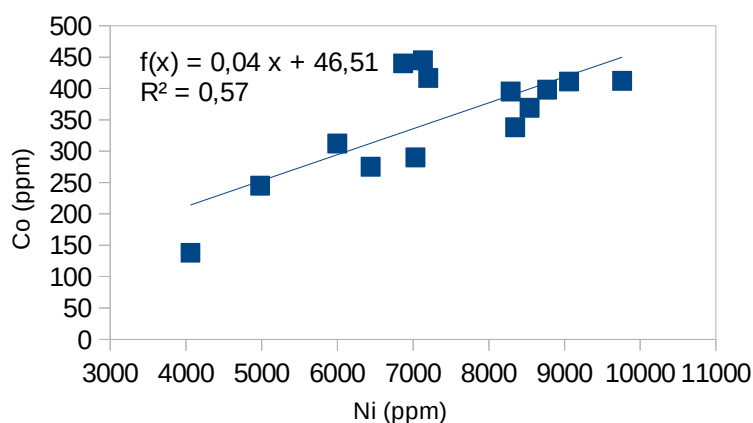


Fig.20: Distribution of Ni content compared to Co content in the samples of Vrysakia mine

Samples with the highest Fe₂O₃ content are EB-4, EB-7, EB-11 and EB-14, while the SiO₂ rich ones are EB-1, EB-6 and EB-13. Sample EB-5 is depleted in both SiO₂ and Fe₂O₃, while it has an important CaO enrichment and the highest LOI, due to the high contents in carbonate minerals. The MgO content is enriched in samples EB-8, EB-5A and EB-10, probably being associated with talc.

EB-9 can be characterized as a special sample. At first, Al₂O₃ content is more than 10% higher compared to the remaining samples, while Fe₂O₃ content has the lowest value. The sample is depleted in Ni, Co and Cr and is enriched in REE, P₂O₅, K₂O and Na₂O. Moreover, EB-9 sample displays a tenfold enrichment in most trace elements compared to the remaining samples. More precisely, the sample contains Ce (>100 ppm), La (~150 ppm), Y (~200 ppm) and Zr (~150 ppm), while the remaining REE and trace metals, such as, Dy, Ga, Gd, Nb, Nd, Pb, Pr, Rb (>50 ppm), Sm, Sr, Th, U and Yb are also enriched compared to the remaining samples of the profile. The content of trace metals in the ore usually ranges between 0,1-20 ppm based on the analyses, except for this particular sample. For example, Ce content is 114 ppm, while the next lower concentration is 15,4 ppm, the Er content is 12,35 ppm, while the second higher concentration is 1,02 ppm, Eu is 4,9 ppm while the next highest content is 0,41 ppm, Sm content is 19,5 ppm while the next highest value is 1,64 ppm and so on.

wt (%)	EB1	EB2	EB3	EB4	EB5A	EB5B	EB6	EB7	EB8	EB9	EB10	EB11	EB12	EB13	EB14
SiO ₂	48,20	37,30	32,10	32,90	34,10	26,70	42,20	33,80	34,90	38,40	38,00	33,20	31,90	44,40	25,40
Fe ₂ O ₃	30,70	37,20	40,80	44,40	38,20	30,50	38,70	44,20	36,80	22,70	29,60	44,80	34,40	36,60	41,00
Al ₂ O ₃	4,97	4,27	4,48	4,24	3,92	3,54	4,68	2,79	4,10	14,45	3,77	4,09	3,97	5,34	3,96
MgO	4,60	4,40	4,51	3,86	7,20	3,42	3,43	5,14	10,95	3,16	6,05	3,46	4,52	3,83	5,17
CaO	0,47	4,52	3,64	1,46	2,44	5,60	0,63	2,11	1,63	2,94	6,68	2,78	7,52	1,02	5,59
TiO ₂	0,23	0,30	0,20	0,11	0,16	0,13	0,19	0,09	0,18	0,93	0,17	0,16	0,41	0,30	0,27
P ₂ O ₅	<0,01	0,01	0,02	<0,01	0,01	0,02	<0,01	0,01	0,11	1,29	0,02	0,03	0,01	<0,01	0,01
K ₂ O	0,46	0,06	0,20	0,05	0,03	0,37	0,42	<0,01	0,16	2,09	0,01	0,16	0,01	0,82	<0,01
Na ₂ O	0,04	0,02	0,03	0,02	0,02	0,02	0,03	0,02	0,05	1,01	0,03	0,05	0,04	0,04	0,03
MnO	0,08	0,09	0,11	0,12	0,14	0,13	0,11	0,15	0,11	0,17	0,12	0,14	0,13	0,07	0,15
Cr ₂ O ₃	1,49	3,73	3,22	5,27	3,11	3,26	3,01	3,39	2,73	0,56	3,32	3,49	5,48	3,10	4,93
LOI	5,69	7,79	7,11	4,28	6,29	22,20	4,24	4,93	6,30	12,90	10,85	5,92	10,10	5,39	8,58
NI0	1,15	1,06	1,08	1,25	0,92	0,88	1,52	0,65	0,89	0,51	0,82	1,12	0,77	1,06	0,91
Total	96,93	99,69	96,42	96,71	95,62	95,89	97,65	96,63	98,02	100,60	98,61	98,28	98,49	100,91	95,09

Table 4: Major elements content (wt%) for samples of the Vrysakia deposit

ppm	EB1	EB2	EB3	EB4	EB5A	EB5B	EB6	EB7	EB8	EB9	EB10	EB11	EB12	EB13	EB14
As	<5	<5	<5	<5	6	32	<5	<5	<5	34	<5	<5	<5	<5	6
Ba	21,1	26,9	14	11,6	8,8	6,7	10,2	11,6	10,9	41,9	15,5	13,3	32	21,8	14,9
Cd	<0,5	0,7	<0,5	<0,5	<0,5	<0,5	<0,5	<0,5	0,5	<0,5	<0,5	<0,5	<0,5	<0,5	<0,5
Ce	6,3	9,6	10,5	8,1	10,5	6,5	11	13,8	13,1	114	6,6	13,9	8,9	15,4	9,3
Co	411	338	369	412	417	440	496	245	290	138	275	398	312	395	445
Cs	7,09	0,49	3,08	0,64	2,23	20,4	2,02	0,64	2,04	7,61	0,28	2,92	0,31	5,29	0,24
Cu	21	22	32	21	20	19	14	9	19	53	20	20	13	29	10
Dy	0,51	1,17	0,98	0,69	0,86	0,49	0,91	1,06	1,58	19,95	0,75	1,25	1	1,12	0,77
Er	0,34	0,74	0,57	0,37	0,47	0,27	0,46	0,56	1,02	12,35	0,51	0,67	0,57	0,64	0,47
Eu	0,12	0,29	0,25	0,17	0,22	0,12	0,26	0,33	0,41	4,9	0,18	0,34	0,25	0,33	0,23
Ga	5,5	5,3	5,4	5,4	4,5	4,1	5,5	3,5	5	19,2	4,5	4,9	5,2	6,2	5
Gd	0,6	1,39	0,92	0,71	0,85	0,57	0,91	1,23	1,88	23,5	0,71	1,31	0,96	1,09	0,89
Hf	0,9	0,7	0,8	0,6	0,6	0,5	0,6	0,5	0,6	3,7	0,6	0,6	0,5	1	0,5
Ho	0,14	0,23	0,19	0,12	0,19	0,1	0,18	0,19	0,34	4,45	0,16	0,27	0,17	0,22	0,16
La	2,8	4,7	4,9	4,2	4,8	3,1	4,5	7	10,1	142,5	3,5	8,1	4,4	7,6	4,5
Li	20	30	30	30	30	100	30	20	20	10	30	30	30	20	40
Lu	0,07	0,11	0,09	0,07	0,07	0,05	0,08	0,08	0,14	1,42	0,07	0,11	0,09	0,12	0,07
Mo	1	1	1	1	1	1	<1	1	<1	<1	1	1	2	1	2
Nb	2,6	1,6	2,2	1,7	1,6	1,3	3,1	1,3	2,1	17,5	1,6	1,9	1,3	3	1,4
Nd	2,6	1,6	2,2	1,7	1,6	1,3	3,1	1,3	2,1	17,5	1,6	1,9	1,3	3	1,4
Pb	4	3	5	3	3	4	2	8	8	25	6	6	<2	5	4
Pr	0,63	1,27	1,24	0,9	1,18	0,78	1,21	1,59	2,03	23,5	0,84	1,8	1,14	1,7	1,03
Rb	19,1	2,6	10,1	2,4	2,9	22,7	15,9	1,4	6,7	57,5	1,2	6,7	1,8	32,7	1
Sc	29	27	32	32	28	23	37	23	25	35	22	35	24	31	28
Sm	0,48	1,11	1,01	0,8	0,99	0,58	0,94	1,14	1,64	19,5	0,78	1,35	1	1,28	0,88
Sn	1	<1	<1	<1	<1	<1	<1	<1	<1	3	<1	<1	<1	<1	<1
Sr	9,7	20	24,9	16,8	30	48,4	10,6	38,5	23,6	46,9	16,1	33,6	35,6	23,8	40,9
Ta	0,2	0,1	0,3	0,3	0,2	0,3	0,2	0,2	0,3	0,5	0,2	0,2	0,2	0,1	0,2
Tb	0,09	0,19	0,14	0,11	0,13	0,08	0,15	0,18	0,26	3,33	0,12	0,19	0,14	0,19	0,11
Th	1,76	1,26	1,88	1,39	1,59	1,21	1,95	1,62	1,77	11,4	1,25	1,91	1,04	2,39	1,47
Tm	0,09	0,13	0,11	0,06	0,09	0,08	0,1	0,11	0,16	1,64	0,09	0,12	0,1	0,12	0,08
U	0,36	0,42	0,46	0,33	1,19	0,48	0,53	0,59	0,69	5,2	0,59	0,58	0,27	0,6	0,24
V	93	184	156	209	158	141	176	169	138	172	147	159	227	161	203
W	1	<1	<1	<1	2	6	1	2	1	3	1	<1	<1	1	<1
Y	2,9	6,4	5,1	3,4	4,1	2,9	4,5	5,7	12,5	191	4	7,8	4,8	6,2	4
Yb	0,38	0,73	0,5	0,37	0,49	0,31	0,53	0,62	0,93	9,9	0,48	0,63	0,57	0,61	0,46
Zn	142	181	182	274	168	155	229	154	151	214	188	199	242	165	212
Zr	28	29	26	19	20	20	26	17	24	149	20	23	21	35	20
ΣREE	46,93	56,37	60,45	53,6	54,32	40,11	65,57	57,56	72,78	619,54	42,21	74,4	49,14	70,29	52,12

Table 5: Trace elements (ppm) for samples of the Vrysakia deposit

The most abundant major element oxides are SiO₂ and Fe₂O₃. The SiO₂ content varies between 25,4 wt % (EB-14) and 48,2 wt % (EB-1) (average 35,57 wt %). The Fe₂O₃ content displays similar variation i.e. between 22,7 wt % (EB-9) and 44,8 wt % (EB-11) with an average of 36,7 wt %. Al₂O₃ content ranges between 3-5 wt %, except for EB-9 sample and the average MgO content is 4,91 wt %.

The abundance of critical metals such as Co, V and Zn exceeds 100 ppm, with variation of 138 ppm (EB-9) up to 496 ppm (EB-6) for Co, 93 ppm (EB-1) up to 227 ppm (EB-12) for V and 142 ppm (EB-1) up to 274 ppm (EB-4) for Zn. The Fe poor, Al₂O₃ rich sample EB-9 has also high contents of Ce, La, Y, and Zr.

Ce, La, Y, Nd, Nb, Sr, Zr, Rb show a positive correlation with Al₂O₃, P₂O₅, K₂O, Na₂O and TiO₂ content and negative correlation with Fe₂O₃, Cr₂O₃, NiO and MgO content. Also, the ΣREE content shows a very strong correlation with P₂O₅ and TiO₂ contents, while P₂O₅, K₂O, Na₂O and TiO₂ are all correlated strongly with Al₂O₃ and between them (Fig.22 a, b, c, e). The NiO content is slightly correlated with Fe₂O₃ and SiO₂ content (Fig.22 f, g), while Cr₂O₃ is more related to Fe₂O₃ and CaO (Fig.22 h, i). SiO₂ and Al₂O₃ are not correlated (Fig.22 l), but if sample EB-9 is excluded from the diagram, correlation increases (Fig.21). A similar situation is observed also between Al₂O₃ and MnO (Fig.22 d), which becomes stronger if we remove sample EB-9. Na₂O and K₂O content show direct association (Fig.22 n), while SiO₂ and MnO show a slightly positive correlation (Fig.22 o). Moreover, ΣREEs are also strongly correlated with Al₂O₃ (R²=0,95), K₂O (R²=0,84) and Na₂O (R²=0,99) (data not shown).

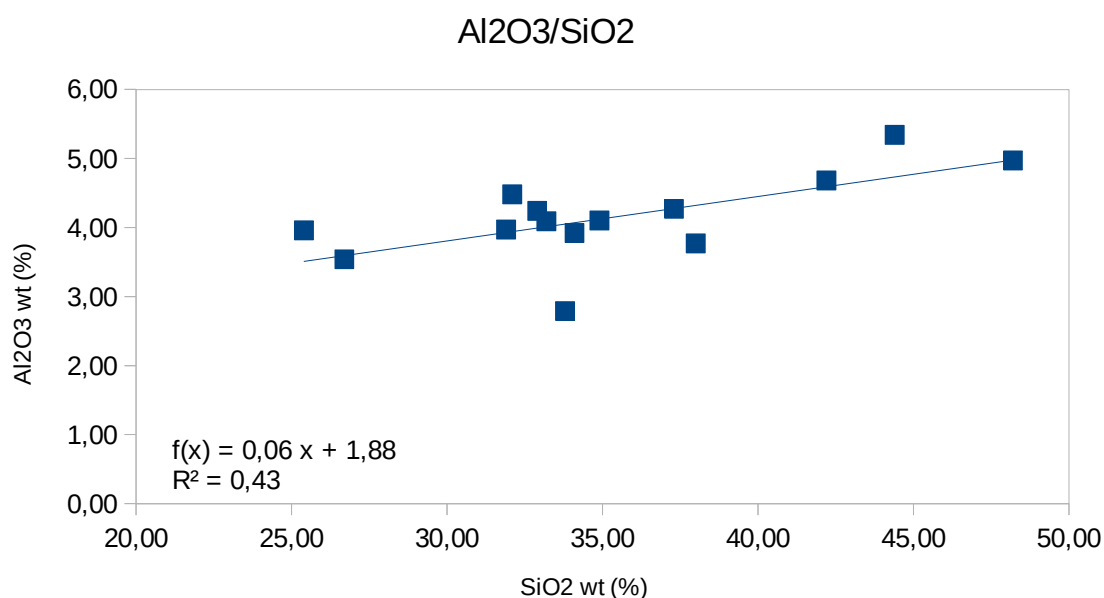


Fig.21: Correlation between Al₂O₃ and SiO₂ for all samples of Vrysakia mine except from EB-9

The REEs are associated in specific domains of the ore, with ΣREE+[Sc]=1382 ppm, ΣLREE=1024 ppm and ΣHREE=392 ppm. Hence the LREEs are significantly enriched compared to the HREEs. Critical metals (REEs+Co+Nb+Sc+Sr+Sn+Ta+V+W+Ga+Hf, (last update of critical raw materials list in EU, CRMs_for_Strategic_Technologies_and_Sectors_in_the_EU_2020)) content reaches up to 10803 ppm.

The chondrite-normalized REE plots (Fig.23) show negative anomalies for Ce and Nd. We also observe gradually negative slopes for HREEs (Fig.20 B), enrichment in LREEs with various

anomalies and a slight Eu negative anomaly, especially in sample EB-9. In addition, the other remaining samples differ from EB-9 because they do not display a negative Ce anomaly, the slope between La, Ce and Pr remains stable and a slightly positive peak appears in Tm. Finally, all samples are enriched to REEs compared to chondrite composition, especially, EB-9.

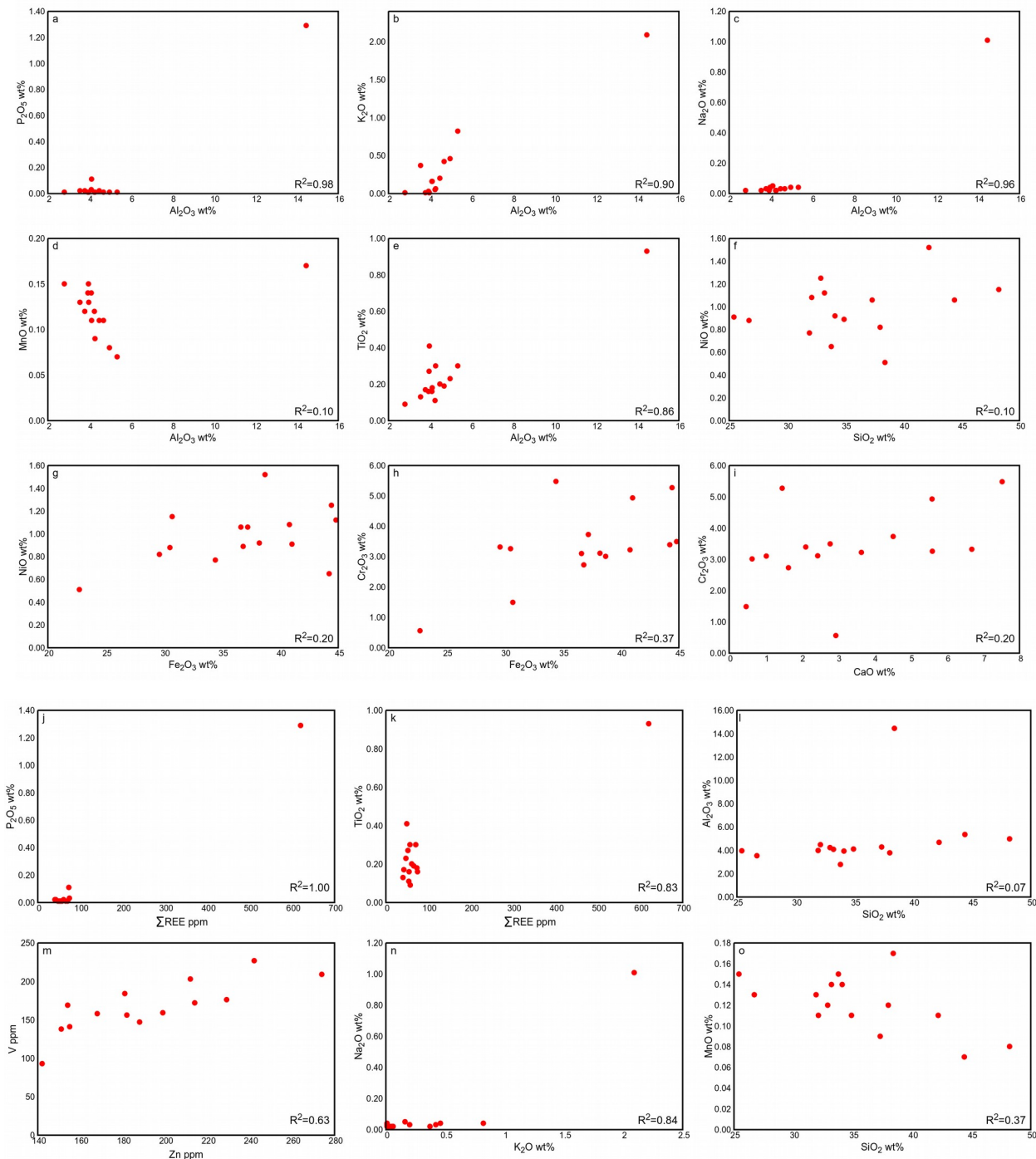


Fig.22: Selected diagrams for major and trace elements in the analyzed lateritic samples from Vrysakia mine. (a) Al_2O_3 vs P_2O_5 , (b) Al_2O_3 vs K_2O , (c) Al_2O_3 vs Na_2O , (d) Al_2O_3 vs MnO , (e) Al_2O_3 vs TiO_2 , (f) SiO_2 vs NiO , (g) Fe_2O_3 vs NiO , (h) Fe_2O_3 vs Cr_2O_3 , (i) CaO vs Cr_2O_3 , (j) Total REE vs P_2O_5 , (k) Total REE vs TiO_2 , (m) Zn vs V , (n) K_2O vs Na_2O , (o) SiO_2 vs MnO

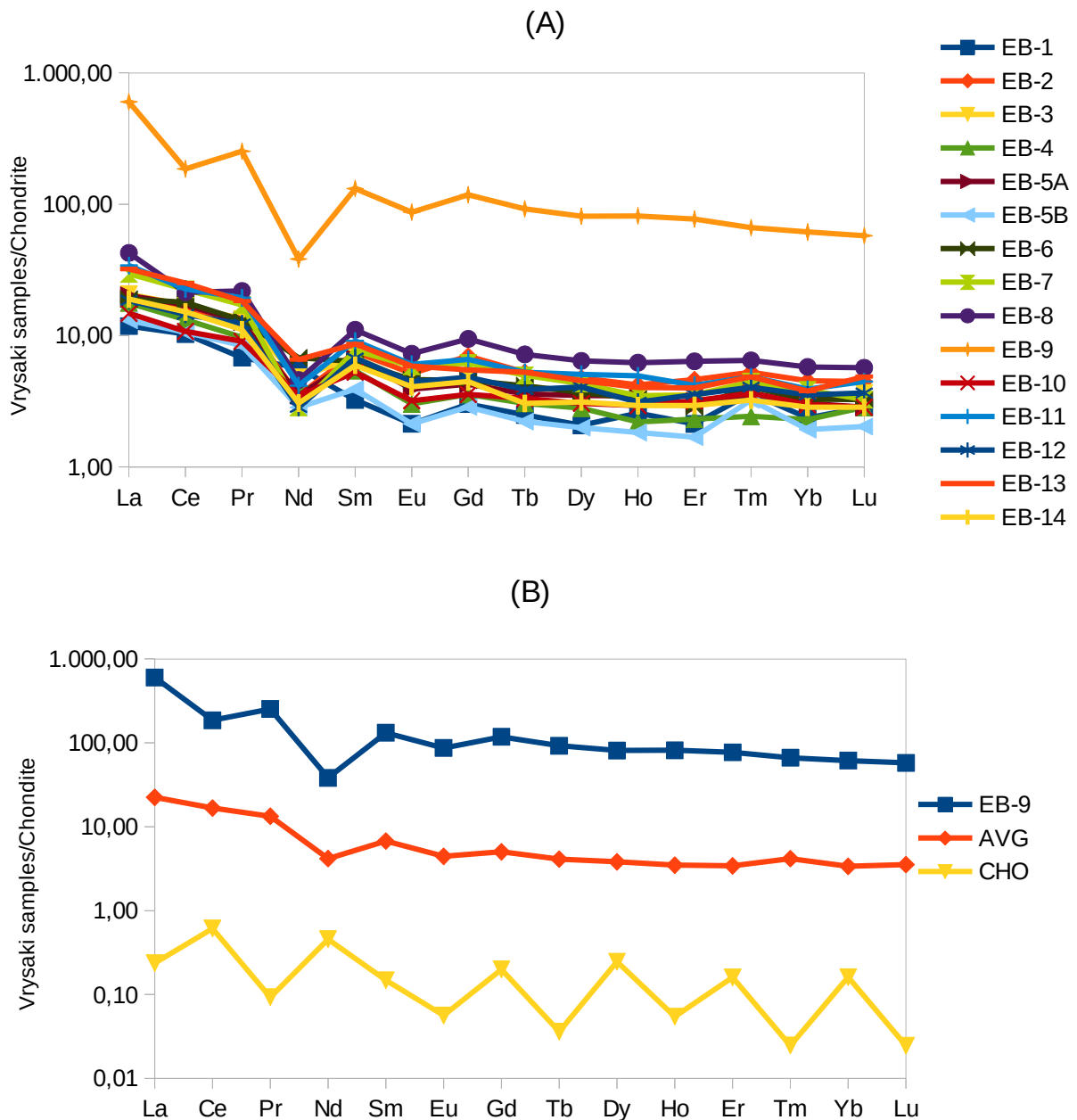
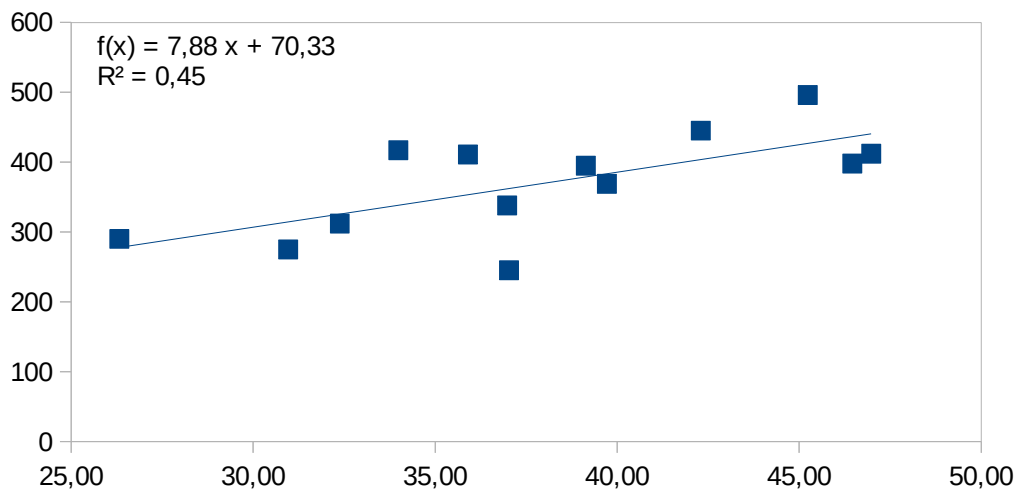


Fig.23: Chondrite-normalized REE plot for whole rock data of (A) all samples of Vrysaki and (B) plot for EB-9 sample, AVG= average composition of all Vrysaki samples except from EB-9 and CHO=Chondrite composition. Normalization values by McDonough and Sun, 1995.

3.4 Correlation of geochemical with mineralogical data

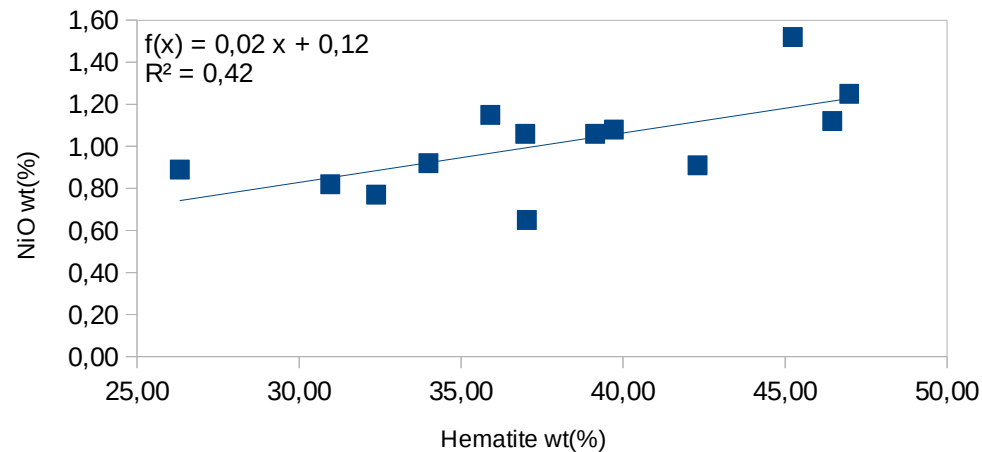
Modelization and quantification of PXRD mineral data through Rietveld method in AutoQuan software, allows us to represent graphically and compare mineral phase's content with geochemical data.

Co/Hematite Content



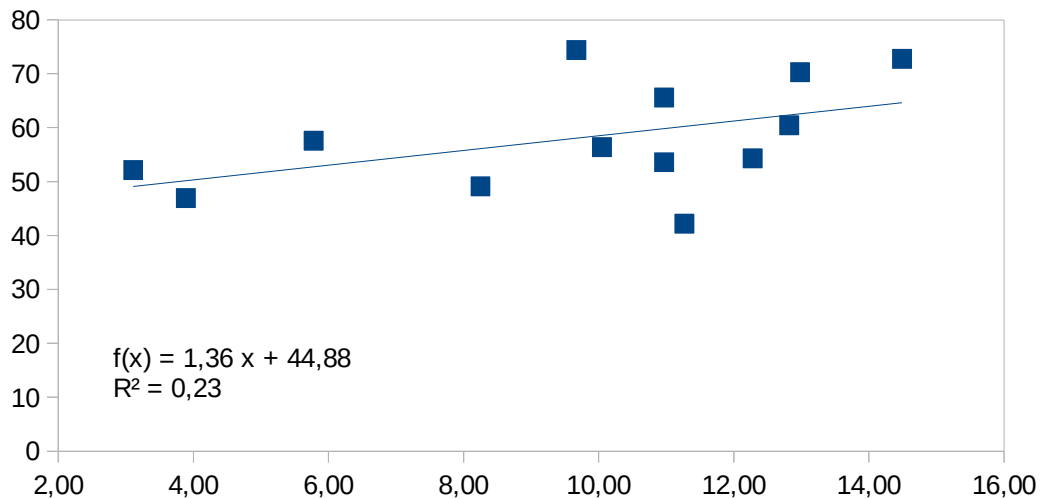
(a)

NiO/Hematite Content



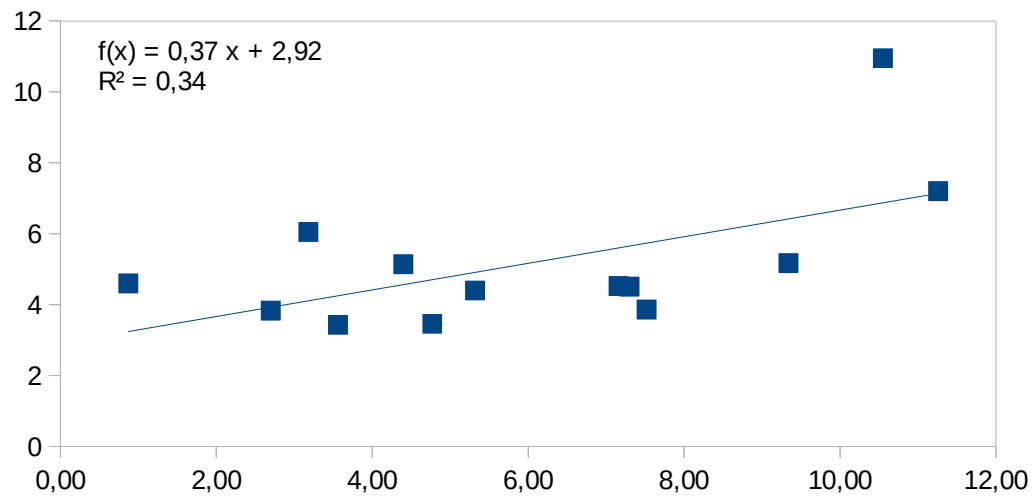
(b)

Σ REE/Chlorite Content



(c)

MgO/Chromite Content



(d)

Fig.24: Correlation between major oxides and critical metals with minerals content in samples from Vrysakia deposit. Samples EB-9 and EB-5B have been excluded from the above diagrams as they presented significant geochemical differences from the rest ferronickel samples.

R^2 is the coefficient of determination. It varies between 0-1 and shows the proportion of the variation in one parameter which is explained by other parameter. From the above diagrams we deduce that some elements follow the distribution of certain minerals, which are apparently related to. For example, Co and NiO content follow hematite content (Fig.24 a&b), which means that at least some part of cobalt and nickel is hosted on hematite, apart from phyllosilicates. Moreover, a slight correlation is presented between total REE content and chlorite, which indicates that some part of REE content might be hosted on chlorite. Finally, chromite can be characterized as Mg-rich considering the above correlation (Fig.24 d).

3.5 REE Mineralogy

Elevated values of LREE (Ce, La, Nd) suggest the possible existence of a REE-mineral phase. Indeed, SEM examination of polished block of sample EB-9 showed the presence of a phosphate-REE mineral phase. These grains have high brightness, most of them are subhedral, partly weathered with angular shape. Their size is tiny and varies between 5-8 μm .

SEM-EDS analysis of grains:

wt%	Phosphate-REE phase		
	EB-9		
Al ₂ O ₃	0,6	0,7	3,5
SiO ₂	0,9	1,7	-
P ₂ O ₅	29,5	32,1	33,3
SO ₄	3,0	3,4	4,5
K ₂ O	0,5	0,3	-
CaO	1,2	1,2	1,6
FeO	0,7	0,5	0,7
Y ₂ O ₃	-	2,6	-
La ₂ O ₃	16,8	16,4	20,4
CeO ₂	24,9	21,5	21,1
Pr ₂ O ₃	3,0	3,4	4,2
Nd ₂ O ₃	13,1	13,4	12,5
Sm ₂ O ₃	-	1,4	1,3
ThO ₂	-	1,5	-
Total	94,2	100,0	102,9

Similar phosphate-REE phases have been discovered in Catalan bauxitic deposits, NE Spain ([95]Reinhardt, 2018) and in the Upper Carboniferous graywackers of the Drahany Upland, Bohemian Massif, Czech Republic ([32]Čopjaková, 2011):

Na.	MM-4 p1	MM-4 p6	0.4 A mag. FC* p10	0.4 A mag. FC* p13
P ₂ O ₅ (wt %)	28.19	28.42	28.44	27.12
SiO ₂	d.l.	1.64	0.04	d.l.
TiO ₂	0.20	0.25	d.l.	d.l.
Al ₂ O ₃	0.48	2.73	d.l.	0.01
FeO	0.14	0.17	0.30	0.20
MnO	d.l.	d.l.	d.l.	d.l.
CoO	0.03	0.02	0.02	0.01
BaO	d.l.	d.l.	d.l.	d.l.
SrO	0.02	d.l.	0.03	0.03
CaO	1.16	0.24	0.25	0.27
Ga ₂ O ₃	0.31	0.06	0.18	0.24
Y ₂ O ₃	1.03	0.36	0.42	0.41
ThO ₂	4.55	0.80	1.89	1.82
UO ₂	0.19	0.05	0.26	0.18
La ₂ O ₃	12.70	6.76	15.79	16.74
Ce ₂ O ₃	27.55	29.49	31.76	31.29
Pr ₂ O ₃	2.96	3.89	2.83	3.11
Nd ₂ O ₃	13.17	18.74	12.40	12.56
Sm ₂ O ₃	1.76	1.96	2.02	2.09
Eu ₂ O ₃	0.99	1.25	0.98	0.96
Gd ₂ O ₃	2.86	2.46	3.27	3.15
Tb ₂ O ₃	d.l.	d.l.	d.l.	d.l.
Dy ₂ O ₃	0.43	0.32	0.27	0.44
Ho ₂ O ₃	0.04	d.l.	d.l.	d.l.
Er ₂ O ₃	0.02	d.l.	d.l.	d.l.
Tm ₂ O ₃	0.26	0.18	0.16	0.24
Yb ₂ O ₃	d.l.	d.l.	d.l.	d.l.
Lu ₂ O ₃	0.02	d.l.	d.l.	0.00
F	1.01	0.87	0.91	1.05
SUM	100.07	100.66	102.22	101.92

Fig.25 : Representative electron microprobe analyses of monazite-(Ce) in heavy mineral concentrates and thin sections of bauxitic samples of Catalan Coastal Range, NE Spain

Representative microprobe analyses of monazite and rhabdophane.

	Mnz 1	Mnz 2	Mnz 3	Mnz 4	Mnz 5	Mnz 6	Mnz 7	Rhb 8	Mnz 9	Rhb 10
SO ₃	<0.01	<0.01	<0.01	<0.01	<0.01	<0.01	<0.01	0.35	<0.01	0.17
P ₂ O ₅	30.53	30.48	30.51	30.54	30.15	29.60	29.60	27.82	29.25	27.22
SiO ₂	0.12	0.02	0.66	0.48	0.11	0.92	3.11	1.10	0.49	2.38
UO ₂	0.99	0.07	0.02	<0.02	0.05	0.02	0.04	0.16	0.03	0.07
ThO ₂	4.47	0.13	0.33	0.09	0.62	1.06	1.81	6.13	3.64	5.75
La ₂ O ₃	12.56	3.90	8.81	17.24	12.07	16.47	13.75	12.55	20.05	15.96
Ce ₂ O ₃	27.34	19.64	29.72	33.35	28.27	32.62	30.95	26.29	35.28	27.99
Pr ₂ O ₃	3.15	4.35	4.31	3.49	3.75	3.29	3.38	2.84	2.50	2.42
Nd ₂ O ₃	12.02	26.86	17.41	11.56	16.50	10.82	11.64	9.37	6.12	7.07
Sm ₂ O ₃	2.50	9.05	3.79	1.56	4.03	1.82	2.00	1.68	0.71	1.00
Eu ₂ O ₃	<0.09	1.35	0.56	<0.09	0.34	<0.09	<0.09	<0.12	<0.09	<0.12
Gd ₂ O ₃	1.87	3.20	1.77	0.52	2.27	0.99	1.14	1.04	0.16	0.66
Dy ₂ O ₃	0.78	0.44	0.37	0.17	0.51	0.26	0.20	0.32	<0.06	0.16
Er ₂ O ₃	0.15	0.05	0.05	<0.04	0.07	<0.04	0.05	<0.04	<0.04	0.05
Y ₂ O ₃	2.63	0.59	0.58	0.31	0.89	0.67	0.59	0.95	0.07	0.82
Al ₂ O ₃	<0.02	<0.02	0.18	0.24	0.02	0.07	0.23	0.40	0.13	1.15
FeO	<0.03	<0.03	<0.03	0.07	0.50	0.35	1.42	1.28	0.44	1.12
PbO	0.14	<0.01	<0.01	<0.01	<0.01	0.01	0.03	0.08	0.05	0.15
CaO	1.08	0.13	0.20	0.06	0.16	0.26	0.30	3.44	0.75	2.38
SrO	<0.03	0.05	0.12	0.04	0.16	0.13	0.13	1.39	0.57	1.13
BaO	<0.03	<0.03	<0.03	<0.03	<0.03	<0.03	<0.03	0.38	<0.03	0.22
F	<0.05	<0.05	<0.05	<0.05	<0.05	<0.05	<0.05	0.34	0.16	0.19
-O=F	0.00	0.00	0.00	0.00	0.00	0.00	0.00	-0.14	-0.07	-0.08
Total	100.35	100.30	99.39	99.73	100.48	99.45	100.37	97.41	100.35	97.78

Fig.26 : Representative microprobe analyses of monazite and rhabdophane from graywackes in Czech Republic (Čopjaková, 2011).

4. Discussion

Geological and diagenetic evolution of sedimentary Fe-Ni deposits of Central Euboea has not received accurate and indisputable explanation so far. Clay mineralogy can guide us to extract some useful conclusions and suggestions about diagenetic events. The transition of one mineral to another through intermediate mixed-layered phases is indicative of diagenesis of the ore. Clay phases that are formed by two or more clay mineral types are characterized as mixed-layered or interstratified. Factors that can trigger this transition include increased temperature and pressure levels due to burial of sediments, fluid movement and circulation, and shearing connected with regional tectonism ([86]Moore and Reynolds, 1989).

The ore contains both discrete and mixed-layered phases with ordered and random interstratification. Chlorite-smectite is the mixed-layered phase, with typically 80% chlorite and 20% smectite composition and random R0 ordering of layers, and it is the main clay phase in almost all samples. Also, chlorite is the major and most abundant clay mineral. Only two samples (EB-1, EB-9) of the Vrysakia deposit are richer to smectitic layers than chloritic ones. Corrensite, the mixed-layered chlorite-smectite phase with 50% chlorite-50% smectite and perfect R1 ordering, is also present in some samples. The above mixed-layered phases usually exist in a variety of geologic environments such as, contact metamorphic zones of shales, old carbonate sequences, Lake Superior iron ores, hydrothermal alteration and weathering products of ophiolitic rocks and dolomites, and generally, sediments that contain sufficient quantities of Mg, which have been by burial diagenesis and weathering, like, for example, Euboea's lateritic sedimentary deposits ([86]Moore and Reynolds, 1989).

The identification of the exact type of smectite was not possible in the present work. Nevertheless, based on the $d_{060}=1,513$ value for smectite and on previous work on Lokris area ([29]Christidis & Skarpelis), we can characterize this phase as nontronitic (Fe-rich, Ni-poor), a composition that is consistent with the ultrabasic source rocks of the ore. The d_{060} reflection value is used in order to distinguish the dioctahedral from the trioctahedral types of clay mineral, based on the fact that the b cell dimension is sensitive to the size of cations and the site occupancy in the octahedral sheet, which it remains unchangeable by the monoclinic angle β effect ([86]Moore and Reynolds, 1989).

The coexistence of discrete chlorite, with R0 chlorite-smectite and corrensite strongly suggests that a) diagenetic phenomena and reactions have affected the primary clay mineralogy of the deposits and b) conversion of smectite to chlorite is a diagenetic process. In literature, there have been some reports about conversion of smectite to chlorite via corrensite and mixed-layered R0 chlorite-smectite or / and mixed layered corrensite-chlorite in diagenetic, metamorphic and hydrothermal geological environments ([25]Buatier, 1995; [17]Beaufort et al., 1999; [100]Robinson et al., 2002; [102]Ryan & Hiller, 2002; [39]Drits et al., 2011; [18]Beaufort et al., 2015). However, so far, smectite of nontronitic composition transformation to chlorite has not been reported to literature. Chlorite genesis has been reported from a) saponite to Mg-chlorite and mixed layered corrensite-chlorite ([25]Buatier, 1995; [17]Beaufort et al., 1999; [100]Robinson et al., 2002; [18]Beaufort et al., 2015), b) berthierine (Fe-rich serpentine) to chlorite via mixed layered berthierine-chlorite ([102]Ryan & Hiller, 2002) and c) kaolinite to sudoite (2:1 layer Mg-rich chlorite with two dioctahedral and one trioctahedral interlayer sheet) via tosudite (1:1 dioctahedral Mg-Al rich regularly interstratified R1 mixed-layered chlorite-smectite) in Al-Mg systems ([18]Beaufort et al., 2015).

Chlorite can be characterized as the main nickeliferous clay mineral with up to 4% NiO content (Table 3) with Mg-Fe-rich composition. Serpentine, which contains up to 1.40% NiO, is present in the majority of samples as minor phase or traces, although, we assume that in the original lateritic in situ mantle the abundance of serpentine and its Ni content were higher. In other cases, the primary lateritic mantle of serpentized peridotites contains as main Ni-bearing phases Ni-serpentine and Ni-goethite in Kastoria's N. Greece laterites ([85]Mposkos et al., 2000), and Ni-smectite and Ni-serpentine in laterites of New Caledonia ([46]Fonteneau et al., 2020). Therefore, the high contents of Mg and Ni in chlorite might originate from the dissolution of serpentine, while the Fe percentage from the dissolution of nontonite/Fe-smectite, reactions that took place during diagenesis. Another source that might contributed to chlorite's Mg and Ni content was possibly the disintegration of Ni-stevensite (trioctahedral Mg-smectite), which his presence has been reported in Othrys mountain Greece ([28]Christidis & Mitsis, 2006) and in laterites of Brazil and N.Caledonia as main Ni-phase ([75]Mano et al., 2014; [46]Fonteneau et al., 2020). Transformation of stevensite can also produce talc layers ([46]Fonteneau et al., 2020), so the presence of abundant talc in certain segments of Vrysakia deposit, might be attributed to the above transfiguration during post-depositional processes. Thus, the main reaction for chlorite genesis in the deposits can be described as:



The coexistence of smectite, corrensite, R0 chlorite-smectite and discrete chlorite might be related to thermal instability in the system, due to different stability temperatures of these mineral phases. The thermal range of the above minerals reactions depends on many aspects. At first, Mg-rich chlorites (clinochlore) replace corrensite above 100-120 °C ([118]Worden & Morad, 2003; and references therein; [18]Beaufort et al., 2015), whereas tosudite and corrensite form below 100 °C. Also, there are reports that in shales, corrensite can develop in temperatures as low as 70 °C ([27]Chang et al., 1986; [18]Beaufort et al., 2015). In view of the above, and due to the predominance of mixed-layered chlorite-smectite and chlorite in the deposits, the burial temperature of lateritic sediments might have been between 70-100 °C. Nevertheless, additional work would be necessary for more accurate estimation of burial conditions and confirmation of (eq. 1).

Redistribution of Ni in the deposits, as has been reported by previous researchers ([114]Valeton et al., 1987), can be attributed to dissolution of serpentine and stevensite during diagenesis, as described by equation 1. Other critical metals, like Co, might also be associated with the same reaction path or similar procedures, as stevensite has been reported as a Co source during lateritization ([28]Christidis & Mitsis, 2006).

On the origin of REEs mineral phase

REE-bearing monazite like phases form naturally as minor or trace constituents in acid/alkalic igneous and metamorphic rocks such as granites, pegmatites, schists, shales, carbonatites and gneiss or in hydrothermally altered silicate rocks. In our case, the REE-phosphate phase was detected in the Vrysakia deposit, coexisting with albite, goethite, abundant illite and talc, as well as, discrete smectite and mixed-layered chlorite-smectite. The sample was collected close to the lowest part of the lens, stratigraphically close to Jurassic limestones floor, and was hosted in an enclave-like formation of the ore.

During laterization process, extreme weathering and limited mobility of REEs inside the lateritic profile induce to enrichment of Rare Earth Elements in residual ores, compared to the parent rocks. These elements can be hosted in the form of: (i) accumulation of primary REE phases of magmatic origin, (ii) precipitation of authigenic/diagenetic product as REE phase and may have been transported via (a) LREE-Actinide oxides sorbed in epigenetic Fe-oxides (b) ion-adsorption clays ([113]Torró et al., 2017; [34]Deady et al., 2016; [2]Aiglsperger et al., 2016; [93]Radusinović et al., 2017; [49]Gamaletsos et al., 2018). Concerning the above, there are two possible mechanisms to explain the existence of monazite like phase. The monazite-(Ce)-like mineral phase might have been transported from the original ophiolite formation, which typically contains a restricted zone of granitic/felsic and alkaline rocks. Indeed, when a subduction system reaches the maturity stage, together with the related back arc basin produces a wide variety of magmatic rocks from MORB-like type to island-arc-tholeiites (IAT) to bonninites and finally to calc-alkaline and alkaline magmatic rocks, progressively over time and stratigraphically upwards ([38]Dilek & Furnes, 2009). For example, in Vardar zone, in Oraiokastron ophiolitic complex, evolved rock types, such as plagiogranites have been reported in the form of lenses or intrusive dykes inside the gabbros. In addition, a dioritic intrusion has been reported in the basaltic lava in the southern border near Pentalofos village ([116]Zachariadis, 2007). It is also possible that the phosphate-REE mineral phase originates from granitic intrusions or metamorphic rocks which aren't related to ophiolitic complex, but have contributed to the formation of the sedimentary Fe-Ni laterite. The other possibility suggests formation of authigenic REE-phosphate mineral during post-depositional processes. In Marmeiko and Nissi karstic nickel deposits in Lokris authigenic REE minerals, mostly bastnasite have been discovered. In these occurrences REEs are considered to have been transported as absorbed ions on clay particles ([74]Maksimovic & Panto, 1996; [60]Kalatha et al., 2017). Authigenic monazite-(Nd) have been reported in the Marmara bauxitic deposit, while monazite-(La) was reported in the Upper Jurassic bauxites of Montenegro ([74]Maksimovic & Panto, 1996). Moreover, apatite, a PO_4 -rich phase, have been reported in Ni-laterites of Edessa area N.Greece. Apatite is related with processes during or after re-deposition of the lateritic crust, and is not considered detrital originating from mafic rocks ([42]Economou-Eliopoulos, 2003).

It is considered that the monazite-like phase in the Vrysakia deposit, is not related to ultrabasic rock sources and due to it's coexistence with abundant albite, illite, goethite and smectite, we propose a sedimentary and not authigenic deposition together with part of the primary/host rock. However, this assumption has to be confirmed with more data, which will assist understanding the variable of sources of the sedimentary Fe-Ni deposits of central Euboea.



Fig.28: EB-9 sample of Vrysakia deposit rich in REEs

5. Conclusions

The sedimentary Fe-Ni deposits of Central Euboea that were formed from erosion and transportation of lateritic mantles, contain a variety of phyllosilicates, which are indicative of certain diagenetic reactions. The main characteristic of the deposits is the coexistence of smectite with corrensite, R0 mixed layer Chlorite-Smectite and discrete chlorite, which suggest disequilibrium conditions. The non-clay mineral phases consist of hematite, quartz, chromite, calcite and pyrite in certain samples, while talc and serpentite are abundant in sectors of the deposits. It is proposed that chlorite, the main Ni-host phase in the deposits is diagenetic, formed by gradual conversion of Fe-rich smectite and possibly stevensite. This alteration might be associated with mobilization of Ni and Co during diagenesis. Additional work would be necessary to specify the exact reaction paths between phyllosilicates and investigate the mobilization of Ni and critical metals during diagenesis. Finally, a (La, Ce, Nd)-rich phosphate, monazite-like mineral phase have been identified in Vrysakia deposit, with REE content in bulk samples up to $\sum\text{REE}+[\text{Sc}]=1382$ ppm and critical metals $\text{CM}=10803$ ppm. It is suggested that Fe-Ni sedimentary deposits of Central Euboea show a rather diverse origin of the lateritic material, not only ultramafic ophiolitic rocks.

Acknowledgments

We are grateful to LARCO GMMSA for allowing us to sample the deposits and the Geologists and Mineral Resources Engineers (Dr. A. Apostolikas, Mr. S. Koukoumtzis and Mr. K. Tavis) of the company for helping in sampling. We are indebted to Prof. Stephen Kiliyas and Mr. Vas. Skounakis (NKUA-Geology Department) for their permission and assistance with the SEM analysis, and Dr. A. Stratakis (MRED-TUC) for the XRD analysis.

References

1. Aiglsperger, T., Proenza, J.A., Zaccarini, F., Lewis, J.F., Garuti, G., Labrador, M., Longo, F., 2015. Platinum group minerals (PGM) in the Falcondo Ni laterite deposit, Loma Caribe peridotite (Dominican Republic). *Miner. Deposita* 50, 105-123.

2. Aiglsperger, T.; Proenza, J.A.; Lewis, J.F.; Labrador, M.; Svojtka, M.; Rojas-Purón, A.; Longo, F.; Ďurišová, J. (2016) Critical metals (REE, Sc, PGE) in Ni laterites from Cuba and the Dominican Republic. *Ore Geol. Rev.* 2016, 73, 127–147.
3. Albandakis, N. 1974. The nickeliferous Fe-ores of Lokris and Euboia. *Metal. Mining Annals*, 19, 1-41 (in Greek).
4. Albandakis, N.D. The nickel-bearing iron-ores in Greece (1980). In *Proceedings of the International Symposium on Metallogeny of Mafic Ultramafic Complexes*, Athens, Greece, 9–11 October 1980; UNESCO IGCP-169; National Technical University of Athens: Athens, Greece, 1980; pp. 194–213.
5. Aleva GJJ (1994) *Laterites—concepts, geology, morphology and chemistry*. ISRIC, Wageningen.
6. Alevizos, G. 1997. *Mineralogy, geochemistry and genesis of sedimentary nickeliferous Fe-ores of Lokris (Central Greece)*. Unpubl. Ph.D Thesis, Tech. Univ. Crete, Greece, 245 p (in Greek).
7. Alexander LT, Cady JG (1962) Genesis and hardening of laterite in soils. *Tech Bull (United States Department of Agriculture)* 1281:1–90.
8. ALS GEOCHEMISTRY (2013) Schedule of services and fees. www.alsglobal.com
9. Andoniades, P.A. & Vgenopoulos, A.G. 1989. Some aspects of the genesis of Ni-Fe-Lateritic ore deposits at Pissona and Katsikiza in the island of Euboea, Greece. In: Augustithis, S.S. (ed) *Metallogeny of basic and ultrabasic rocks (regional presentations)*, Theophrastus Publications, Athens, 519-531.
10. Argyriadis, I. 1966. La série stratigraphique de l'Eubée moyenne (Grèce). Existence de mouvements intra-séno-niens. *Comptes-rendus de l'Académie des Sciences, Paris*, 262 (D), 2427 – 2430.
11. ARONIS, G. (1954) : Geographical distribution, geological placing and aspects on the genesis of the Greek bauxite. *Bull. Geol. Soc. Greece*, vol.II, no 1, p.55-79.
12. AUBOUIN, J. 1959. Contribution à l'étude de la Grèce septentrionale: les confins de l'Épire et de la Thessalie. Thèse, sciences, Univ. Paris, 1958 et *Ann. géol. Pays hellen.*, 10, 1-525, Athènes.
13. Aubouin, J., 1977. Alpine tectonics and plate tectonics: thoughts about the Eastern Mediterranean. *Europe from Crust to Core*. J. Wiley, pp. 143–158.
14. Augustithis, S.S., 1962. Mineralogical and Geochemical Changes in the Diagenetic and Post-Diagenetic Phases of the Ni-Cr-Iron Oolitic Deposit Larymna/Lokris, Greece. *Chemie der Erde* 22, 5-17.

15. Barth, M. G., Mason, P. R., Davies, G. R., & Drury, M. R. (2008). The Othris Ophiolite, Greece: a snapshot of subduction initiation at a mid-ocean ridge. *Lithos*, 100(1–4), 234–254. <https://doi.org/10.1016/j.lithos.2007.06.018>
16. Baumgartner, P.O. and Bernoulli, D., 1976. Stratigraphy and radiolarian fauna in a Late Jurassic–Early Cretaceous section near Achladi (Evvoia, eastern Greece). *Eclogae Geol. Helv.*, 69 (3):601–626.
17. Beaufort, D.; Baronnet, A.; Lanson, B.; Meunier, A. Corrensite: A single phase or mixed-layer phyllosilicate in the saponite-to-chlorite conversion series? A case study of Sancerre-Couy deep drill hole (France). *Amer. Miner.*, **1999**, 82, 109-124.
18. Beaufort, D.; Rigault, C.; Billon, S.; Billault, V.; Inoue, A.; Inoue, S.; Patrier, P. Chlorite and chloritization processes through mixed-layer mineral series in temperature geological systems – a review. *Clay Miner.*, **2015**, 50, 497-523.
19. Bignot F.J., Fleury J.J. and Guernet C1. (1973) Sur la stratigraphie du Cretace superieur et du flysch en Eubee meoyenne (Zone pelagonienne, Grece), *Bull. SOC. gdol. Fr.*, 7, 484-489.
20. Bland W, Rolls D (1998) *Weathering: an introduction to the scientific principles*. Arnold, London.
21. Bobba, S., Carrara, S., Huisman, J. (co-lead), Mathieux, F., Pavel, C. (co-lead) (2020) *Critical Raw Materials for Strategic Technologies and Sectors in the EU: A Foresight Study*.
22. Bortolotti, V., & Principi, G. (2005). Tethyan ophiolites and Pangea break-up. *Island Arc*, 14(4), 442–470. <https://doi.org/10.1111/j.1440-1738.2005.00478.x>
23. Brand, N.W., Butt, C.R.M., Elias, M., 1998. Nickel laterites: classification and features. *AGSO J. Aust. Geol. Geophys.* 17, 81–88.
24. Brunn, J., 1956. Contribution a l'etude geologique du Pinde septentrionale et d'une partie de la Macedoine occidentale. *Ann. Geol. Pays Hellen.* 7, 1–358.
25. Buatier, M.D.; Früh-Green, G.L.; Karpoff, A.M. Mechanisms of Mg-phyllosilicate formation in a hydrothermal system at a sedimented ridge (Middle Valley, Juan de Fuca). *Contrib. Mineral. Petrol.*, **1995**, 122, 134-151;
26. Butt, C.R.M., Cluzel, D., 2013. Nickel laterite ore deposits: Weathered serpentinites. *Elements* 9, 123-128.
27. Chang H.K., Mackenzie F.T. & Schoonmaker J. (1986) Comparisons between the diagenesis of dioctahedral and trioctahedral smectite, Brazilian offshore basins. *Clays and Clay Minerals*, 34, 407–423.
28. Christidis, G.E.; Mitsis, I. A new Ni-rich stevensite from the ophiolite complex of Othrys, central Greece. *Clays Clay Miner.*, **2006**, 54; 653-666.
29. Christidis, G.E., Skarpelis, N., 2010. Clay mineralogy of the sedimentary iron nickel ore of Agios ioannis, NE boeotia: new data and implication for diagenetic modifications.

- Proceedings of the 12th International Congress of the Geological Society of Greece. pp. 2553–2561.
30. Clift, P. D., & Dixon, J. (1998). Jurassic ridge collapse, subduction initiation and ophiolite obduction in the southern Greek Tethys. *Eclogae Geologicae Helveticae*, 91, 123–138.
 31. Cluzel, D., and Vigier, B., 2008, Syntectonic mobility of supergene nickel ores from New Caledonia (southwest Pacific). Evidences from faulted regolith and garnierite veins: *Resource Geology*, v. 58, p. 161–170.
 32. Čopjaková R. , Novák M. , Franců E. (2011) Formation of authigenic monazite-(Ce) to monazite-(Nd) from Upper Carboniferous graywackes of the Drahany Upland: Roles of the chemical composition of host rock and burial temperature, *Lithos* 127 (2011) 373–385. doi:10.1016/j.lithos.2011.08.001.
 33. Danelian, T., & Robertson, A. H. (2001). Neotethyan evolution of eastern Greece (Pagondas Melange, Evia island) inferred from radiolarian biostratigraphy and the geochemistry of associated extrusive rocks. *Geological Magazine*, 138(3), 345–363. <https://doi.org/10.1017/S0016756801005337>
 34. Deady, É.A.; Mouchos, E.; Goodenough, K.; Williamson, B.J.; Wall, F. A review of the potential for rare-earth element resources from European red muds: Examples from Seydişehir, Turkey and Parnassus-Giona, Greece. *Mineral. Mag.* 2016, 80, 43–61.
 35. De Bono, A. (1998). Pelagonian Margins in central Evia island (Greece): stratigraphy and geodynamic evolution, Université de Lausanne.
 36. De Bono, A., Martini, R., Zaninetti, L., Hirsch, F., Stampfli, G. M., & Vavassis, I. (2001). Permo-Triassic stratigraphy of the pelagonian zone in central Evia island (Greece). *Eclogae Geologicae Helveticae*, 94, 289–311.
 37. Deprat, J. 1904. Étude géologique et pétrographique de l'île d'Eubée. Thèse, Besançon 1904, 230 pp. 14 pl.
 38. Dilek I., Furnes H., Structure and geochemistry of Tethyan ophiolites and their petrogenesis in subduction rollback systems, *Lithos*, Volume 113, Issues 1–2, 2009, p. 1-20, ISSN 0024-4937.
 39. Drits, V.A.; Ivanovskaya, T.A.; Sakharov, B.A.; Zviagyna, B.; Gor'kovam N.V.; Pokrovskaya, E.V.; Savichev, A.T. Mixed-layers corrensitite-chlorites and their formation mechanisms in the glauconic sandstones-clayed rocks (Riphean, Anabar uplift). *Lithol. Mineral Res.*, **2011**, 46, 566-593.
 40. Eggleton RA (2001) The Regolith Glossary. Cooperative Research Centre for Landscape Evolution and Mineral Exploration, Perth, 144 pp, www.crclme.org.au/Pubs/monographs
 41. Eliopoulos, D., Economou-Eliopoulos, M., 2000. Geochemical and mineralogical characteristics of Fe-Ni and bauxitic laterite deposits of Greece. *Ore Geol. Rev.* 16, 41-58.

42. Economou-Eliopoulos, M. (2003) Apatite and Mn, Zn, Co-enriched chromite in Ni- laterites of northern Greece and their genetic significance. *J. Geochem. Explor.* 2003, 80, 41–54.
43. Economou-Eliopoulos, M., Megremi I. , Vasilatos Ch. , Frei R. , Mpourodimos I. (2017) Geochemical constraints on the sources of Cr(VI) contamination in waters of Messapia (Central Evia) Basin, *Applied Geochemistry* 84 (2017) 13-25
44. Ferriere, J., Bertrand, J., Simantov, J., Dewever, P., 1988. Comparaison entre des formations volcanodétritiques (« Mélanges ») du Malm des Hélienides internes (Orthrys, Eubée); implications géodynamiques. *Bulletin of the Geological Society of Greece* 20, 223–235.
45. Ferriere J. , Baumgartner Peter O. , Chanier F. (2016) The Maliaic Ocean: the origin of the Tethyan Hellenic ophiolites. *Int J Earth Sci (Geol Rundsch)*. DOI 10.1007/s00531-016-1303-6
46. Fonteneau, L.; Caner, L.; Petit, S.; Juillot, F.; Ploquin, F.; Fritch, E. Swelling capacity of mixed talc-like/stevensite layers in white/green clay infillings (“deweylite”/ “garnierite”) from serpentine veins of faulted peridotites, New Caledonia. *Amer. Mineral.*, **2020**, *105*, 1536-1546.
47. Francke, Jan, Nobes, DC (2000) Preliminary evaluation of GPR for nickel laterite exploration [4084-02] PROCEEDINGS-SPIE THE INTERNATIONAL SOCIETY FOR OPTICAL ENGINEERING
48. Freyssinet, Ph., Butt, C.R.M., Morris, R.C., 2005. Ore-forming processes related to lateritic weathering. *Econ. Geol.* 100 th Anniversary Volume, 681-722.
49. Gamaletsos, P.N.; Godelitsas, A.; Filippidis, A.; Pontikes, Y. The Rare Earth Elements Potential of Greek Bauxite Active Mines in the Light of a Sustainable REE Demand. *J. Sustain. Metall.* 2018.
50. Gartzos, E., 1986. On the Genesis of Cryptocrystalline Magnesite Deposits in the Ultramafic Rocks of Northern Evia (Greece). PhD Thesis ETH Zuerich, Switzerland, 195 pp.
51. Gartzos E. , Dietrich V.J. , Migiros G. , Serelis K. , Lymperopoulou Th. (2009) The origin of amphibolites from metamorphic soles beneath the ultramafic ophiolites in Evia and Lesbos (Greece) and their geotectonic implication, *Lithos* 108 (2009) 224–242.
52. Ghosh S, Guchhait S (2015) Characterization and evolution of primary and secondary laterites in northwestern Bengal Basin, West Bengal, India. *J Palaeogeogr* 4(2):203–230.
53. Ghosh S, Guchhait S (2020) Laterites of the Bengal Basin_ Characterization, Geochronology and Evolution; SpringerBriefs in Geography, Springer Nature Switzerland AG 2020; Chapter 1; pp 1-16;
54. Golightly, J.P., 2010. Progress in understanding the evolution of nickel laterites. *Soc. Econ. Geol. Spec. Publ.* 15, 451-485.

55. Gleeson, S.A., Butt, C.R., Elias, M., 2003. Nickel laterites: a review. SEG Newsletter 54, 11–18.
56. Guernet, Cl. 1971. Etudes géologiques en Eubée et dans les régions voisines (Grèce). Thèse, Paris 1971, Mémoire de la Faculté de Sciences de Paris, 395 p. 50 pl.
57. Guernet C. (1975) Sur l'existence en Eubée moyenne d'une nappe constituée principalement de roches vertes et de leur couverture mésozoïque, Ann. SOC. Géol. du Nord, XCV, 59-66.
58. Jacobshagen, V., & Wallbrecher, E. (1984). Pre-Neogene nappe structure and metamorphism of the North Sporades and the southern Pelion peninsula. Geological Society, London, Special Publications, 17(1), 591–602. <https://doi.org/10.1144/GSL.SP.1984.017.01.46>
59. Kalatha, S., Economou-Eliopoulos, M., 2015. Framboidal pyrite and bacterio morphic goethite at transitional zones between Fe-Ni-laterites and limestones: Evidence from Lokris, Greece. Ore Geol. Rev. 65, 413-425.
60. Kalatha, S., Perraki, M., Economou-Eliopoulos, M., Mitsis, I., 2017. The origin of bastnaesite-(La,Nd,Y) in the Nissi (Patitira) bauxite laterite deposit, Lokris, Greece. Minerals 7, 1–19.
61. Karunakaran C, Sinha Roy C (1981) Laterite profile development linked with polycyclic geomorphic surfaces in South Kerala. In: Proceedings of the international seminar on lateritisation processes, Trivandrum, India.
62. KATSIKATSOS, G., FYTIKAS, M., KOUKIS, G. (1969) The iron-nickel ore deposits of the north-eastern part of Central Euboea (Kimi area). Geological reconnaissance, no45, Inst.Geol.Subsurf.Res. , Athens.
63. KATSIKATSOS, G., KOUKIS, G., PAPASPYROU, A. (1975) The magnesite and iron-nickel deposits of Pisonos area, Central Euboea. Mineral Deposit Res. , no 2, N.I.G.M.R. , Athens.
64. Katsikatsos, G., 1977. La structure tectonique d'Attique et de l'île d'Eubée. Réunion. Extraord. Soc. Géol. Fr. et de Grèce en Grèce, 1976, Bull. Soc. Géol. Fr., (7), XIX, 1, 75-80.
65. Katsikatsos G., Fytrolakis N. and Perdikatsis V., 1980. Contribution to the Genesis of Lateritic Deposits of the Upper Cretaceous Transgression in Attica and Central Euboea (Greece). UNESCO, International Symposium on Metallogeny of Mafic and Ultramafic Complexes (I.G.C.P. project No. 169). Technical University of Athens. Dept. of Mineralogy-Petrography.
66. Katsikatsos, G., de Bruijn, H., van der Meulen, A., 1981. The Neogene of the Island of Euboea (Evia), a review. Geol. Mijnb. 60, 509–526.

67. Katsikatsos G. et al. (1981a) 2:50,000 Geological map of the Psachna-Pilion Sheet. IGME, Athens, Greece.
68. Katsikatsos G. et al. (1981b) 1:50,000 Geological map of the Kymi Sheet. IGME, Athens, Greece.
69. Katsikatsos, G., Migiros, G., Triantafyllis, M., Mettos, A., 1986. Geological structure of internal Hellenides (E. Thessaly–SW Macedonia–Euboa–Attica–northern Cyclades and Lesvos). *Geol. Geophys. Res.*, sp. Vol. in Honor prof. Papastamatiou, pp. 191–212.
70. ΚΤΕΝΑ Κ. (1930) Έκθεσις περί των κατά τα έτη 1928 και 1929 γενομένων γεωλογικών ερευνών. Πρακτ. Ακαδ. Αθηνών, Τ. 5, σ. 92-107.
71. KURZWEIL, H. (1966) Zur Mineralogie Ni-führender Verwitterungs und sedimentarer Fe-Erze in Lokris, Mittelgriechenlands. *Berg-und Hüttenm. Monatsch. Jahrg*, T. III, S. 488-497, Wien.
72. Maffione, M., Thieulot, C., Van Hinsbergen, D. J., Morris, A., Plümpner, O., & Spakman, W. (2015). Dynamics of intraoceanic subduction initiation: 1. Oceanic detachment fault inversion and the formation of supra-subduction zone ophiolites. *Geochemistry, Geophysics, Geosystems*, 16, 1753–1770. <https://doi.org/10.1002/2015GC005746>
73. Maignien R (1966) Review of research on laterites. UNESCO, Paris
74. Maksimovic, Z.J.; Pantó, G. Authigenic rare earth minerals in karst-bauxites and karstic nickel deposits. In *Rare Earth Minerals, Chemistry, Origin and Ore Deposits*; Jones, A.P., Wall, F., Williams, C.T., Eds.; Springer: Berlin, Germany, 1996; Chapter 10; pp. 257–279.
75. Mano, E.S.; Caner, L.; Petit, S.; Chaves, A.P.; Mexias, A.S.; Mineralogical characterisation of Ni-bearing smectites from Niquelândia, Brazil. *Clays Clay Miner*, **2014**, 62, 324–335.
76. ΜΑΡΑΤΟΣ, Γ. (1960) Σιδηρονικελιούχα κοιτάσματα Τσούκας-Λουσιίου-Καστρακίου (περιοχή Λοκρίδος). Γεωλ. Αναγν. Εκθ. 30 , ΙΓΕΥ, Αθήναι.
77. McDonough W.F. , Sun S.-s. (1995) The composition of the Earth. *Chemical Geology* 120 (1995) 223-253.
78. McFarlane MJ (1976) Laterite and landscape. Academic Press, London
79. Ministère de l'Énergie et des Ressources naturelles of Québec Canada (2017) DISCUSSION PAPER: REVIEW OF QUÉBEC'S ROLE IN THE DEVELOPMENT OF CRITICAL AND STRATEGIC MINERALS
80. Μουντράκης, Δ. (1985). Γεωλογία της Ελλάδας. University Studio Press.
81. Mountrakis, D. (1986). The Pelagonian zone in Greece. A polyphase-deformed fragment of the Cimmerian Continent and its role in the geotectonic evolution of the Eastern Mediterranean. *Journal of Geology*, 94, 335-347.
82. ΜΟΥΝΤΡΑΚΙΣ, Δ. (2002). Tectonic evolution of the Hellenic Orogen. Geometry and kinematics of deformations. *Bulletin of the Geological Society of Greece*, 34(6), 2113-2126.

83. Mountrakis D. M (2010) *Geology and Geotectonic evolution of Greece*. Thessaloniki. University Studio Press.
84. Mposkos, E.; Perraki, T.; Kolokotroni K. (1996) The Ni and Cr distribution in the mineralogical phases of the nickeliferous laterites from Evia Island. *Miner. Wealth*, **1996**, 101, 9-26 (in Greek with English abstract).
85. Mposkos, E.; Orphanoudaki A.; Perraki, T. (2000) The Ni distribution in the mineral phases of Greek Fe-Ni laterite deposits. *Proceedings of the 3rd Congress of Mineral Wealth*, Athens, Greece, 2000, 107-115.
86. Moore, D.M. & Reynolds, R.C. Jr 1989. *X-Ray Diffraction and the Identification and Analysis of Clay Minerals*, Oxford University Press, New York
87. Papanikolaou D. (2009) Timing of tectonic emplacement of the ophiolites and terrane paleogeography in the Hellenides, *Lithos* 108 (2009) 262–280
88. Papanikolaou D. 2015. *Geology of Greece*. *Regional Geology Reviews*, Springer, Cham. <https://doi.org/10.1007/978-3-030-60731-9>
89. PETRASCHEK, W. (1954) Die Eisenerz und Nickelagerstätten von Lokris in Ostriegrichenland. *Bull. Of Inst. Geol. And Subsurf. Res.* p. 135-169, Athens.
90. Porkoláb, K., Willingshofer, E., Sokoutis, D., Creton, I., Kostopoulos, D., & Wijbrans, J. (2019). Cretaceous–Paleogene tectonics of the Pelagonian zone: Inferences from Skopelos island (Greece). *Tectonics*, 38, 1946–1973. <https://doi.org/10.1029/2018TC005331>
91. Proenza, J.A., 2015. *Mineralogía y Geoquímica de Ni, Co, EGP, Sc, REE en Yacimientos Lateríticos*. Macla, 3-9.
92. Putzolu F., Santoro L.†, Porto C., Mondillo N., Machado M., Almeida B. Saar De, Bastos A., Herrington R. (2021) The Influence of the Magmatic to Postmagmatic Evolution of the Parent Rock on the Co Department in Lateritic Systems: The Example of the Santa Fé Ni-Co Deposit (Brazil). *Economic Geology*, v. XXX, no. XX, pp. X–X.
93. Radusinović, S.; Jelenković, R.; Pačevski, A.; Simić, V.; Božović, D.; Holclajtner-Antunović, I.; Životić, D. Content and mode of occurrences of rare earth elements in the Zagrad karstic bauxite deposit (Nikšić area, Montenegro). *Ore Geol. Rev.* 2017, 80, 406–428.
94. Reche, R., 1983. *Petrographische und geochemische Untersuchungen an alpinotypen Harzburgiten und deren Begleitgesteinen in Lokris und auf Euboea, Mittelgriechenland*. Thesis, Univ. of Hamburg, Hamburg, 128 pp.
95. Reinhardt Nils, Proenza A.J. , Villanova-de-Benavent C., Aiglsperger Th., Bover-Arnal T. , Torró L. , Salas R. and Dziggel A., (2018) *Geochemistry and Mineralogy of Rare Earth*

- Elements (REE) in Bauxitic Ores of the Catalan Coastal Range, NE Spain, *Minerals* 2018, 8, 562; doi:10.3390/min8120562
96. Renz, C. 1940. Die Tektonik der griechischen Gebirge. *Mémoires de l'Académie d'Athènes*, 8, 1-171.
97. Richter, D., Müller, C. & Risch, H. 1996: Die Flysch-Zonen Griechenland XI. Neue Daten /ur Stratigraphie und Paläogeographie des Flysches und seiner Unterlage in der Pelagonischen Zone (Griechenland). *N. Jb. Geol. Paläont. Abh.* 201. 327-366.
98. Robertson, A. H. F., 1990. Late Cretaceous oceanic crust and Early Tertiary foreland basin development, Euboea, Eastern Greece. *Terra Nova*, 2: 333-339.
99. Robertson, A.H.F., 1991. Origin and emplacement of an inferred Late Jurassic subduction–accretion complex, Euboea, Eastern Greece. *Geological Magazine* 128, 27–41.
100. Robinson, D.; Schmidt, S.Th.; Santana de Zamora, A. Reaction pathways and reaction progress for the smectite-to-chlorite transformation: evidence from hydrothermally altered metabasites. *J. Metamorphic Geol.*, **2002**, 20, 167-174.
101. Rosenberg, F. 1984. Geochemie und Mineralogie lateritischer Nickel- und Eisenerze in Lokris und auf Euböa, Griechenland. Unpubl. Ph.D Thesis, Univ. Hamburg, Germany, 129 p.
102. Ryan, P.C.; Hillier, S. Berthierine/chamosite, corrensite and discrete chlorite from evolved verdine and evaporate-associated facies in the Jurassic Sundance Formation, Wyoming. *Amer. Miner.*, **2002**; 87, 1607-1615
103. Samama, J.C., 1986. Ore fields and continental weathering: New York, Van Nostrand Reinhold Co., 326 p.
104. Samouhos M., Godelitsas A., Nomikou Ch., Taxiarchou M., Tsakiridis P., Zavašnik J., N. Gamaletsos P., Apostolikas A. (2019) New insights into nanomineralogy and geochemistry of Ni-laterite ores from central Greece (Larymna and Evia deposits), *Geochemistry*, Volume 79, Issue 2, 2019, p. 268-279.
105. Schellmann W (1982) Eine neue laterite definition. *Geol jahrb D* 58:31–41
106. Scherreiks, R. (2000). Platform margin and oceanic sedimentation in a divergent and convergent plate setting (Jurassic, Pelagonian Zone, NE Evvoia, Greece). *International Journal of Earth Sciences*, 89(1), 90–107. <https://doi.org/10.1007/s005310050319>
107. Scherreiks, R., Bosence, D., BouDagher-Fadel, M., Meléndez, G., & Baumgartner, P. O. (2010). Evolution of the Pelagonian carbonate platform complex and the adjacent oceanic realm in response to plate tectonic forcing (Late Triassic and Jurassic), Evvoia, Greece. *International Journal of Earth Sciences*, 99(6), 1317–1334. <https://doi.org/10.1007/s00531-009-0461-1>

108. Skarpelis, N. 1997. Eocene nickel laterite deposits in Greece and Albania. In: Papunen H. (ed) Mineral Deposits: Research and Exploration. Where do they meet? A.A. Balkema, Rotterdam, 503-506.
109. Skarpelis N. (2002) Introduction to Economic Geology, National Kapodistrian University of Athens, Department of Geology and Geoenvironment, Economic Geology and Geochemistry Sector
110. SPILIADIS, TH. (1958): Geologische erzlagerstatische Untersuchungen im östlichen Teil von Mitteleuböa. Ann. Geol. Pays. Hell. , t.9, p. 198-200.
111. Stampfli, G. M., & Borel, G. (2002). A plate tectonic model for the Paleozoic and Mesozoic constrained by dynamic plate boundaries and restored synthetic oceanic isochrons. Earth and Planetary Science Letters, 196(1-2), 17-33. [https://doi.org/10.1016/S0012-821X\(01\)00588-X](https://doi.org/10.1016/S0012-821X(01)00588-X)
112. Tardy Y (1992) Diversity and terminology of laterite profile. In: Martini IP, Chesworth W (eds) Weathering, soils and paleosols. Elsevier, Amsterdam, pp 379-405.
113. Torró, L.; Proenza, J.A.; Aiglsperger, T.; Bover-Arnal, T.; Villanova-de-Benavent, C.; Rodríguez-García, D.; Ramírez, A.; Rodríguez, J.; Mosquea, L.A.; Salas, R. Geological, geochemical and mineralogical characteristics of REE-bearing Las Mercedes bauxite deposit, Dominican Republic. Ore Geol. Rev. 2017, 89, 114-131.
114. Valetón, I., Biermann, M., Reche, R. & Rosenberg, F. 1987. Genesis of nickel laterites and bauxites in Greece during the Jurassic and Cretaceous, and their relation to Ultrabasic parent rocks. Ore Geol. Rev. 2, 359-404.
115. Villanova-de-Benavent, C., Proenza, J.A., Galí, S., García-Casco, A., Tauler, E., Lewis, J.F., and Longo, F., 2014, Garnierites and garnierites: Textures, mineralogy and geochemistry of garnierites in the Falcondo Ni-laterite deposit, Dominican Republic: Ore Geology Reviews, v. 58, p. 91-109.
116. Zachariadis P., 2007, Ophiolites of the eastern Vardar Zone, N. Greece. PhD Thesis, Johannes Gutenberg-Universität, Mainz.
117. Warr, L.N. Recommended abbreviations for the names of clay minerals and associated phases *Clay Miner.*, **2020**, 55, 261-264.
118. Worden R.H. & Morad S. (2003) Clay minerals in sandstones: control on formation, distribution and evolution. International Association of Sedimentologists, Special Publication, 34, 3-41.

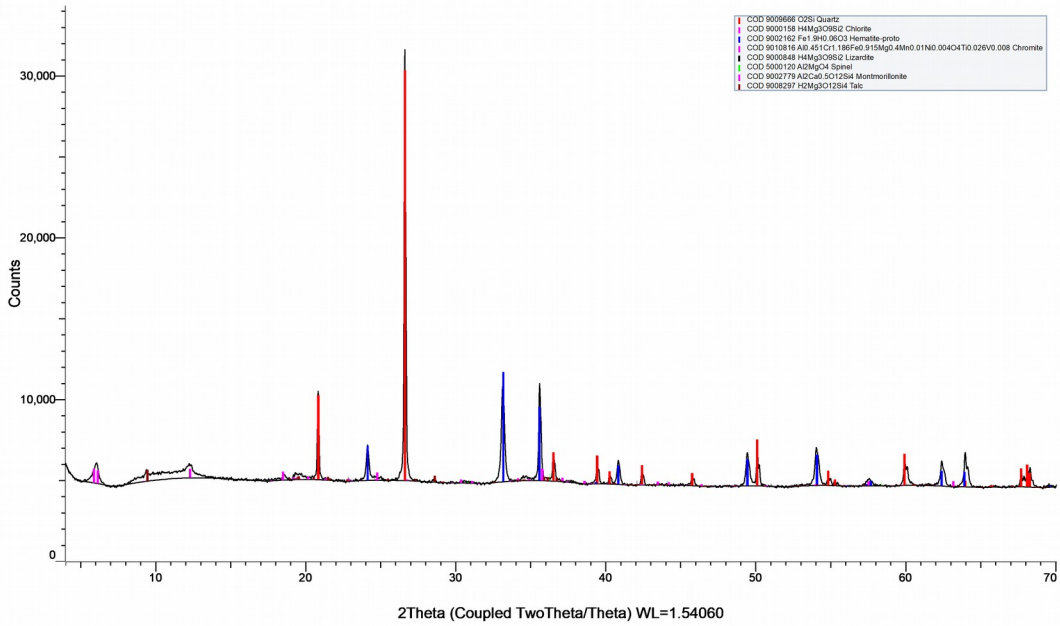
APPENDIX

ANALYTES AND RANGES (ppm)								CODE
SiO ₂	0.01-100%	MgO	0.01-100%	TiO ₂	0.01-100%	BaO	0.01-100%	ME-ICP06
Al ₂ O ₃	0.01-100%	Na ₂ O	0.01-100%	MnO	0.01-100%	LOI	0.01-100%	
Fe ₂ O ₃	0.01-100%	K ₂ O	0.01-100%	P ₂ O ₅	0.01-100%			
CaO	0.01-100%	Cr ₂ O ₃	0.01-100%	SrO	0.01-100%			
Ba	0.5-10,000	Hf	0.2-10,000	Sn	1-10,000	W	1-10,000	ME-MS81
Ce	0.5-10,000	Ho	0.01-1,000	Sr	0.1-10,000	Y	0.5-10,000	
Cr	10-10,000	La	0.5-10,000	Ta	0.1-2,500	Yb	0.03-1,000	
Cs	0.01-10,000	Lu	0.01-1,000	Tb	0.01-1,000	Zr	2-10,000	
Dy	0.05-1,000	Nb	0.2-2,500	Th	0.05-1,000			
Er	0.03-1,000	Nd	0.1-10,000	Tl	0.5-1,000			
Eu	0.03-1,000	Pr	0.03-1,000	Tm	0.01-1,000			
Ga	0.1-1,000	Rb	0.2-10,000	U	0.05-1,000			
Gd	0.05-1,000	Sm	0.03-1,000	V	5-10,000			
Ag	0.5-100	Cu	1-10,000	Ni	1-10,000	Zn	2-10,000	
Cd	0.5-1,000	Li	10-10,000	Pb	2-10,000			ME-4ACD81
Co	1-10,000	Mo	1-10,000	Sc	1-10,000			
As	0.1-250	Hg	0.005-25	Se	0.2-250	Te	0.01-250	ME-MS42
Bi	0.01-250	Sb	0.05-250					

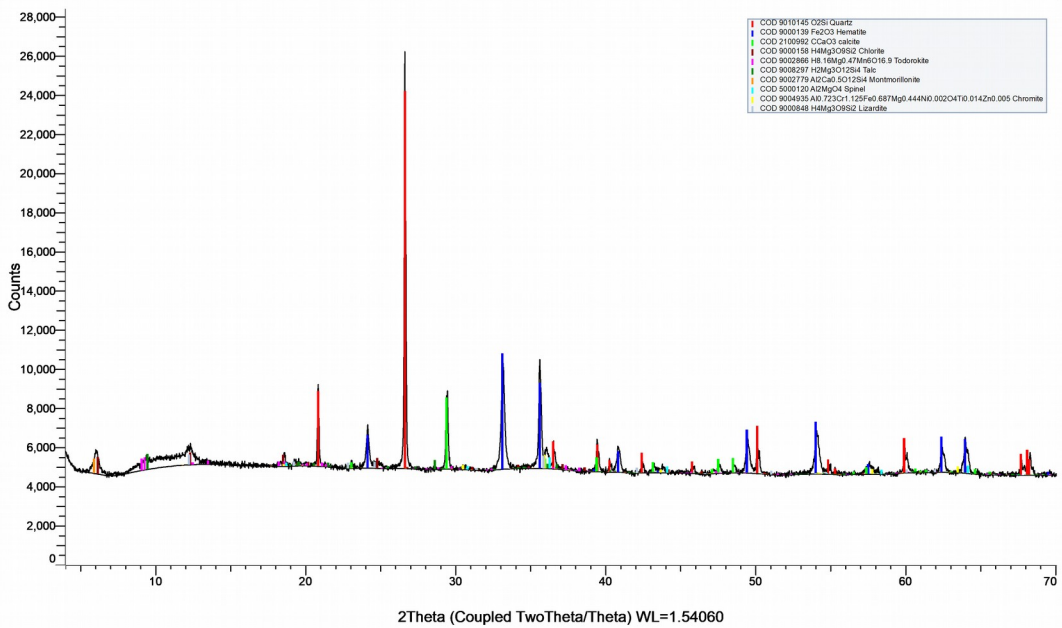
Table A: Limits of each analytic method that was used and code names. ME-ICP06: ICP-AES technique, ME-MS81: lithium borate fusion, ME-4ACD81: a four acid digestion for the base metals, ME-MS42: aqua regia digestion for volatile gold and associated elements

PXRD patterns of all bulk samples:

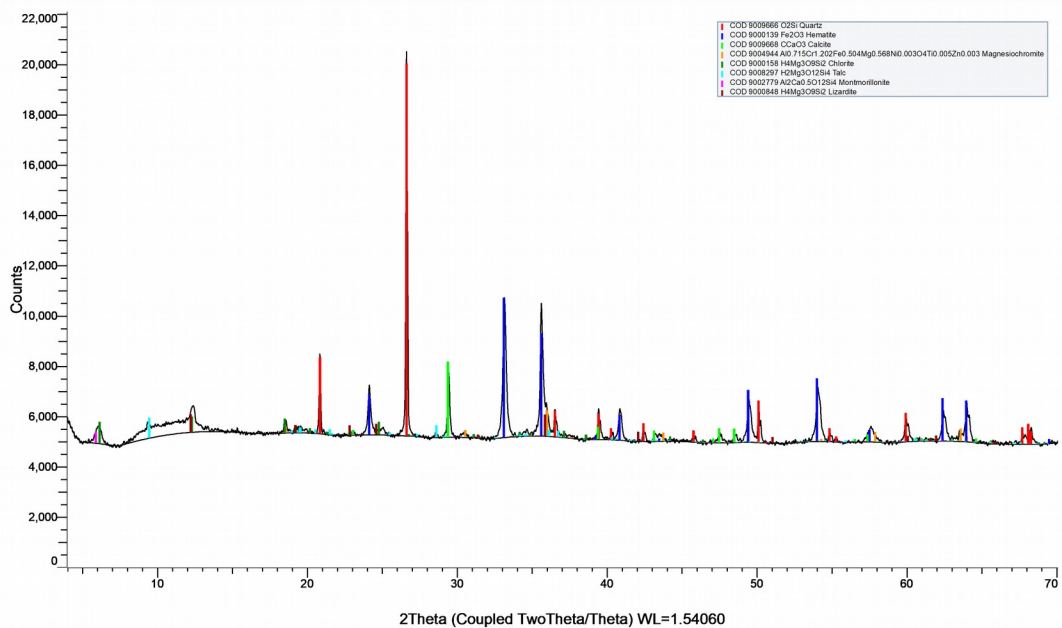
EB1 Bulk (Coupled TwoTheta/Theta)



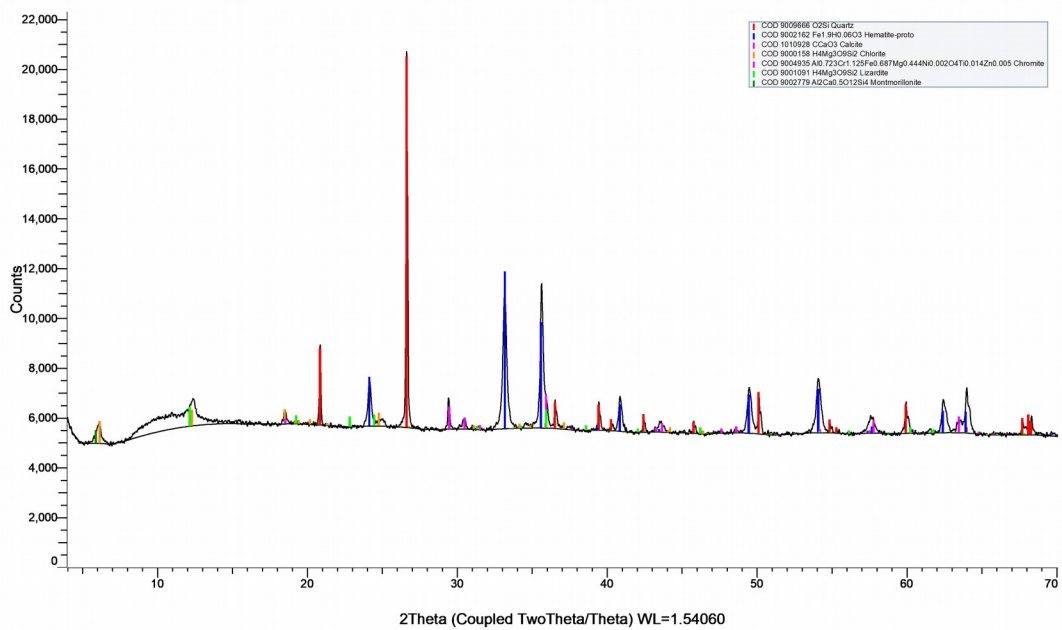
EB2 Bulk (Coupled TwoTheta/Theta)



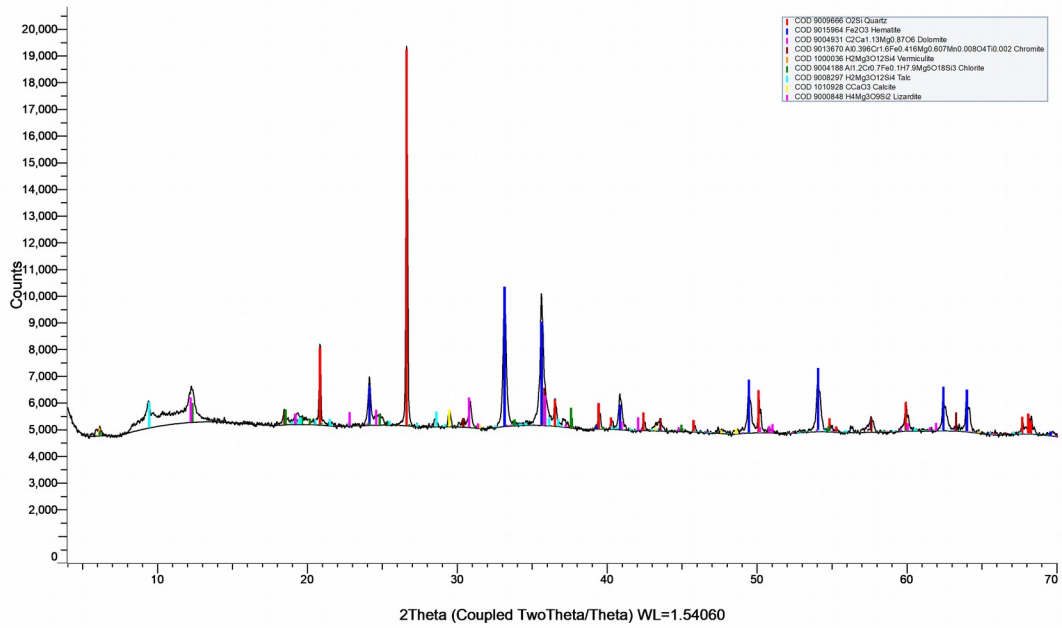
EB3 Bulk (Coupled TwoTheta/Theta)



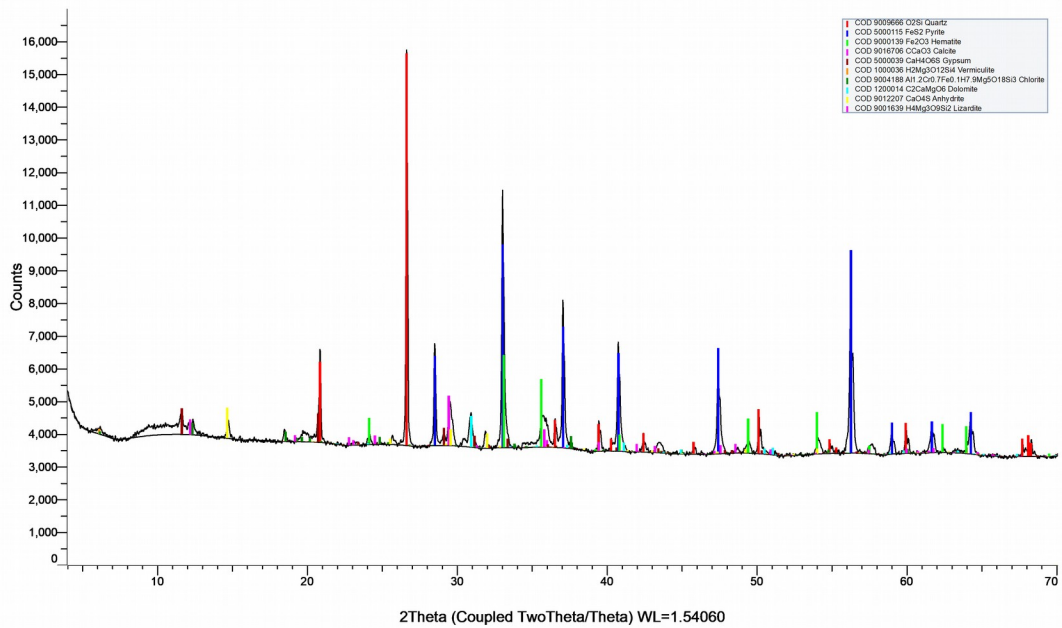
EB4 Bulk (Coupled TwoTheta/Theta)



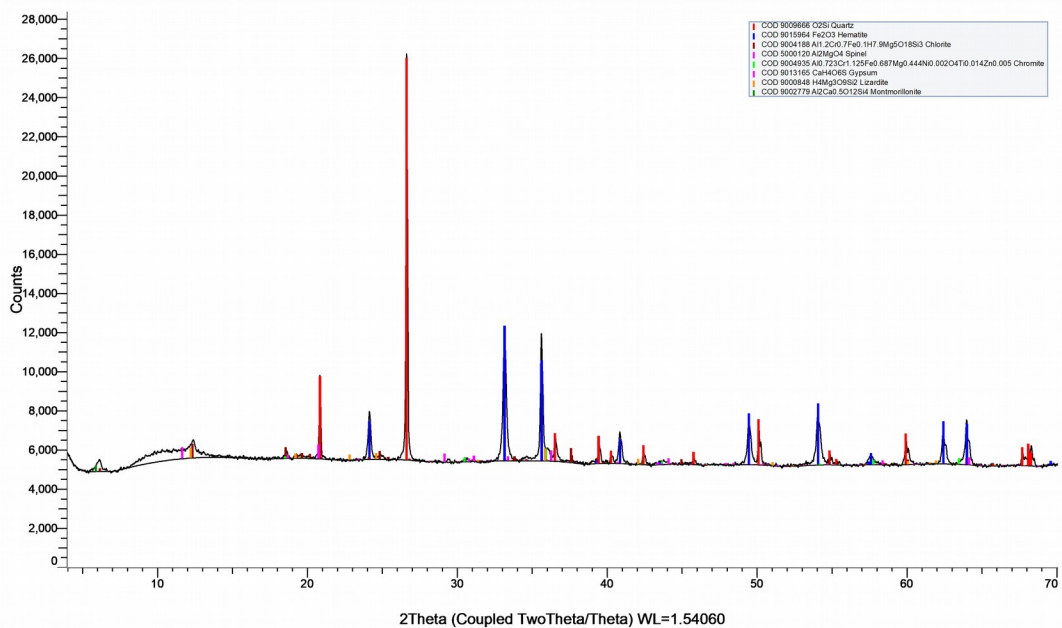
EB5A Bulk (Coupled TwoTheta/Theta)



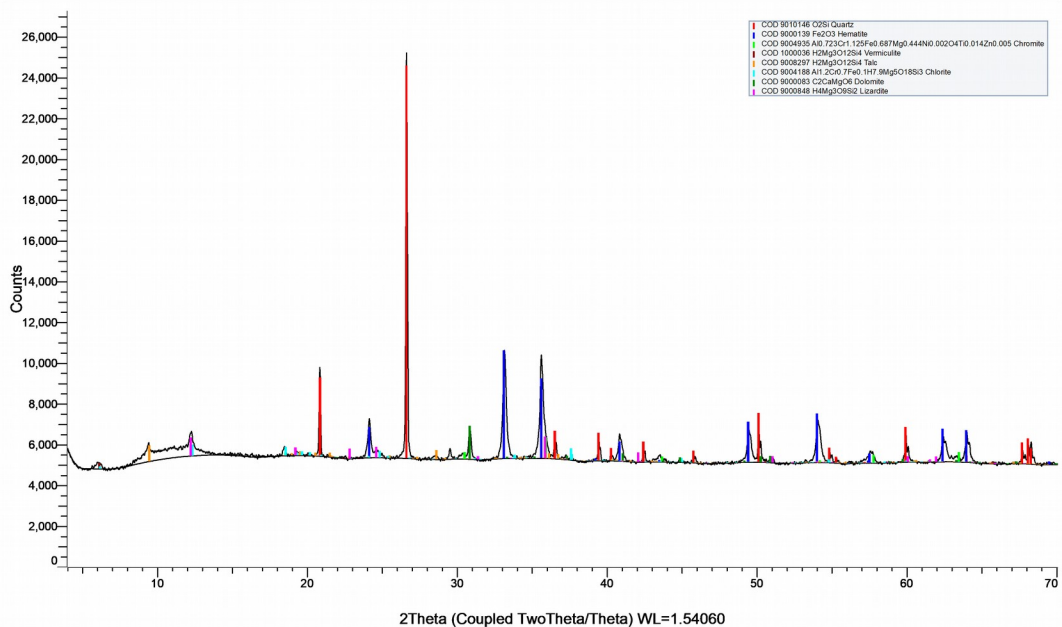
EB5B Bulk (Coupled TwoTheta/Theta)



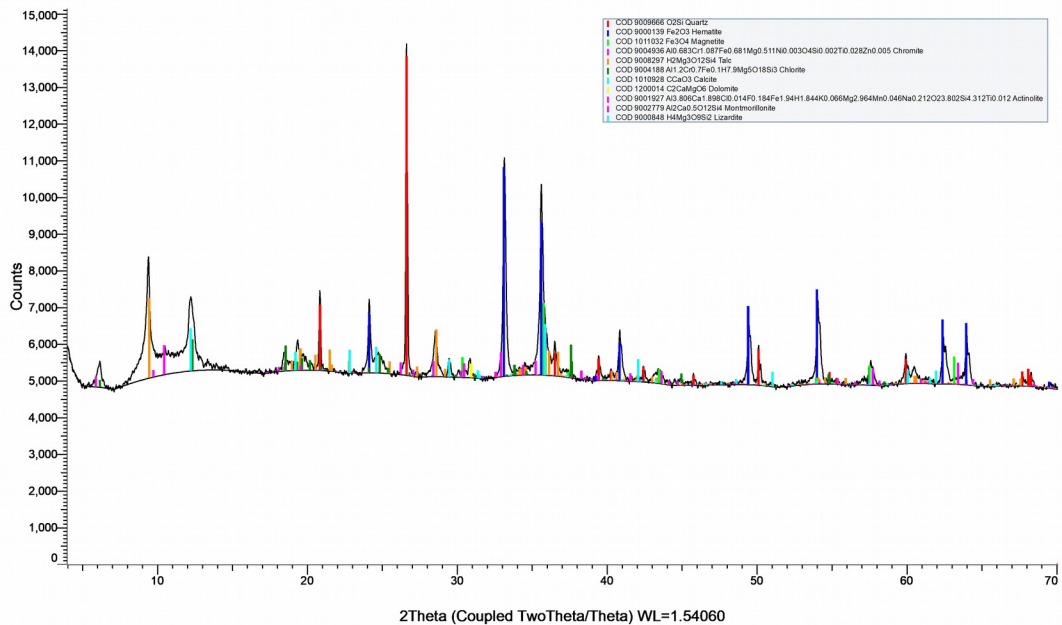
EB6 Bulk (Coupled TwoTheta/Theta)



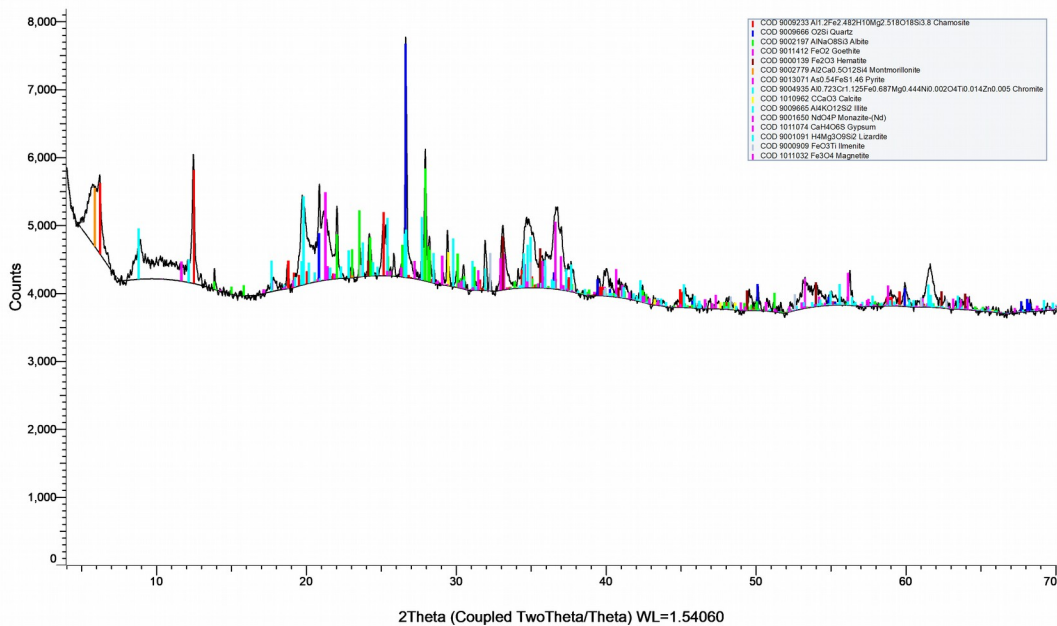
EB7 Bulk (Coupled TwoTheta/Theta)



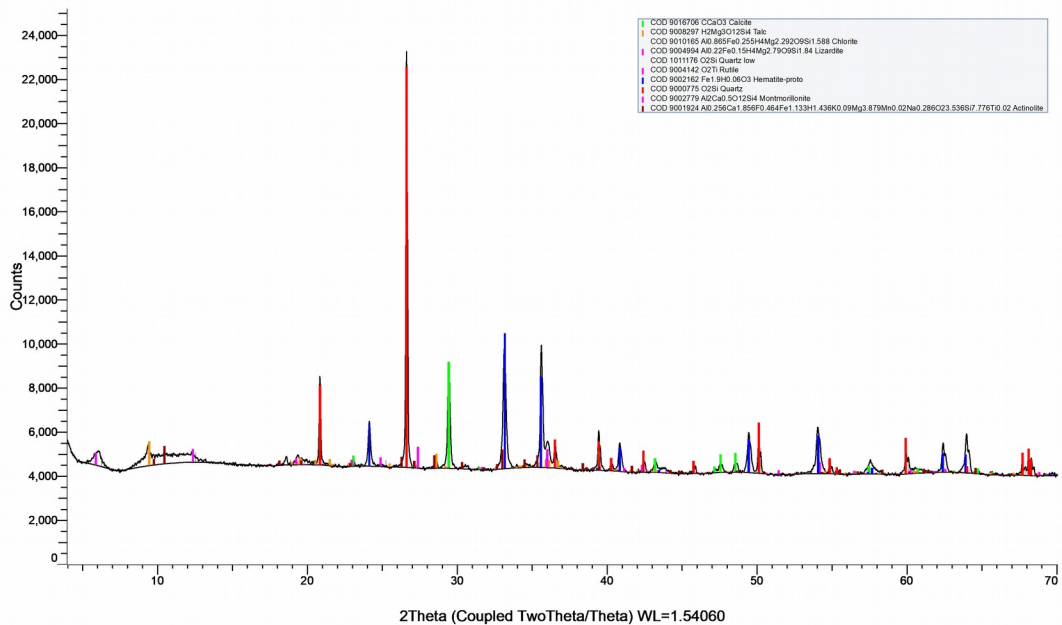
EB8 Bulk (Coupled TwoTheta/Theta)



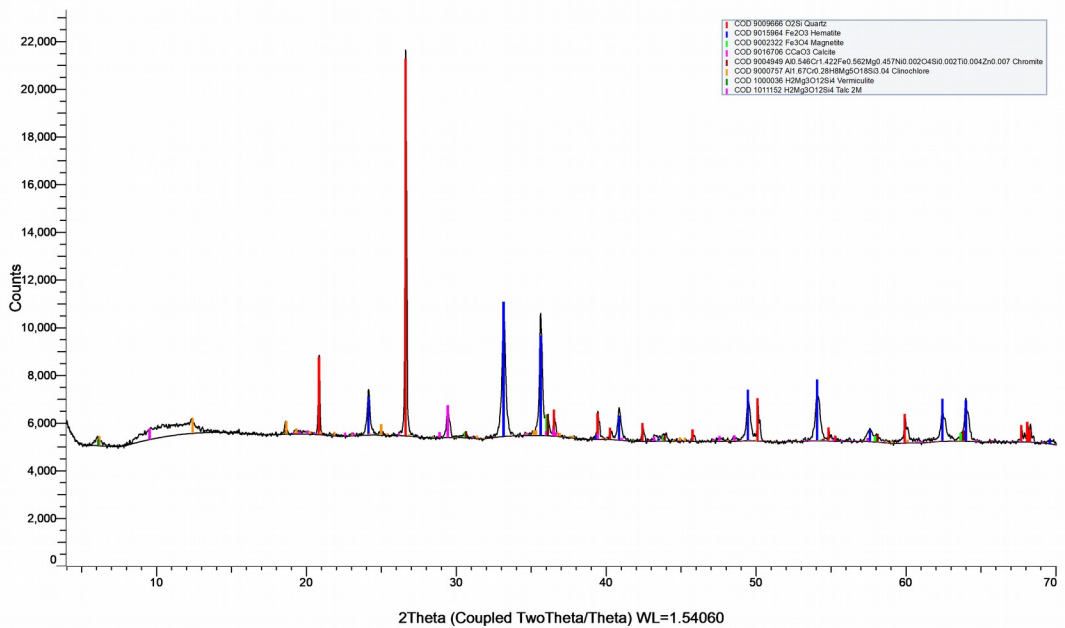
EB9 Bulk (Coupled TwoTheta/Theta)



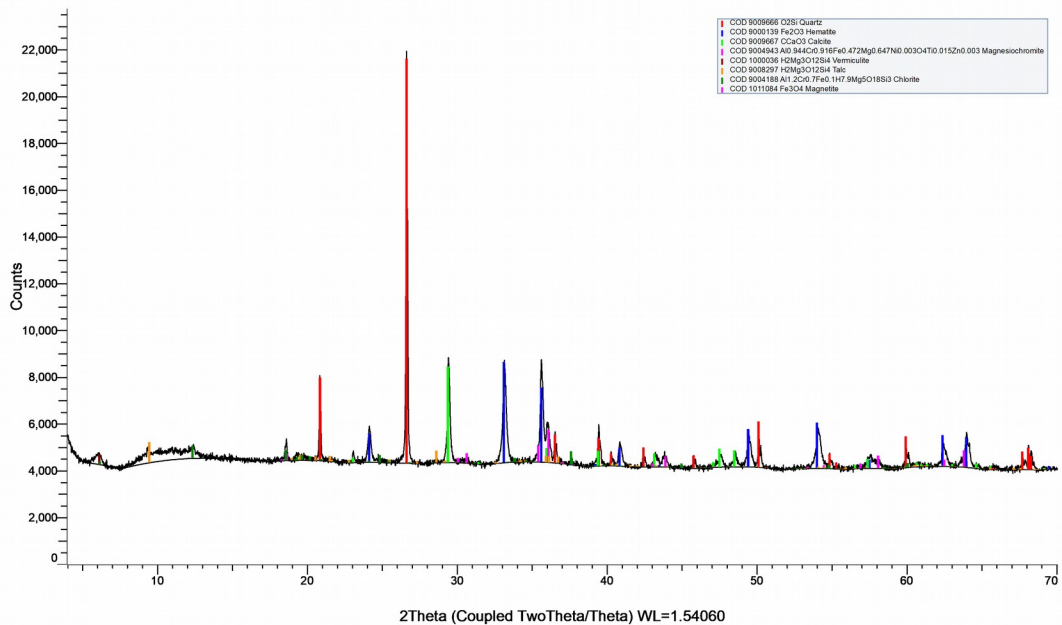
EB10 Bulk (Coupled TwoTheta/Theta)



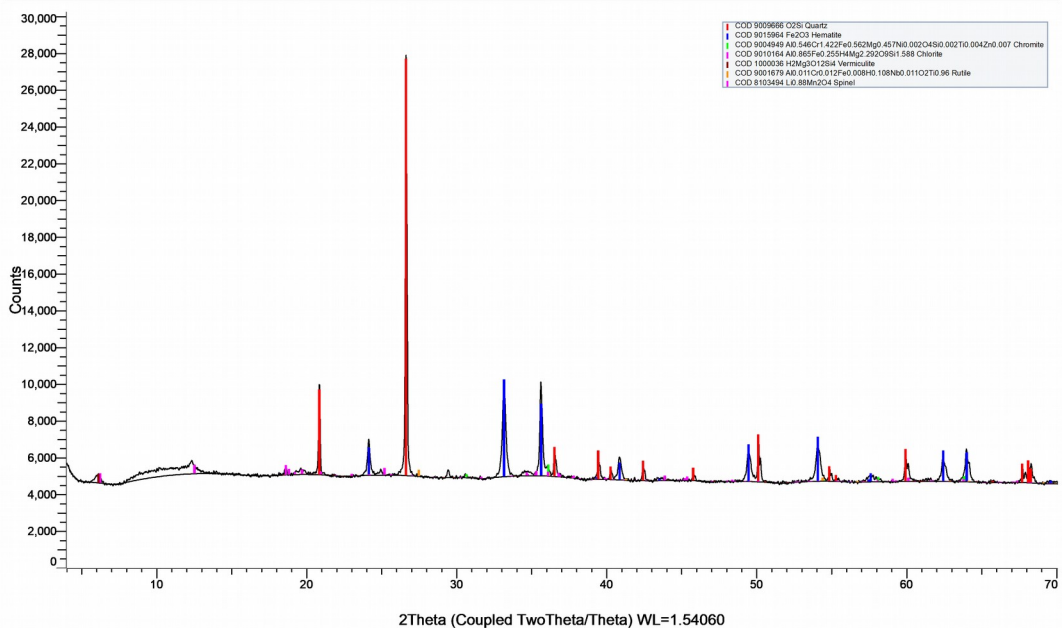
EB11 Bulk (Coupled TwoTheta/Theta)



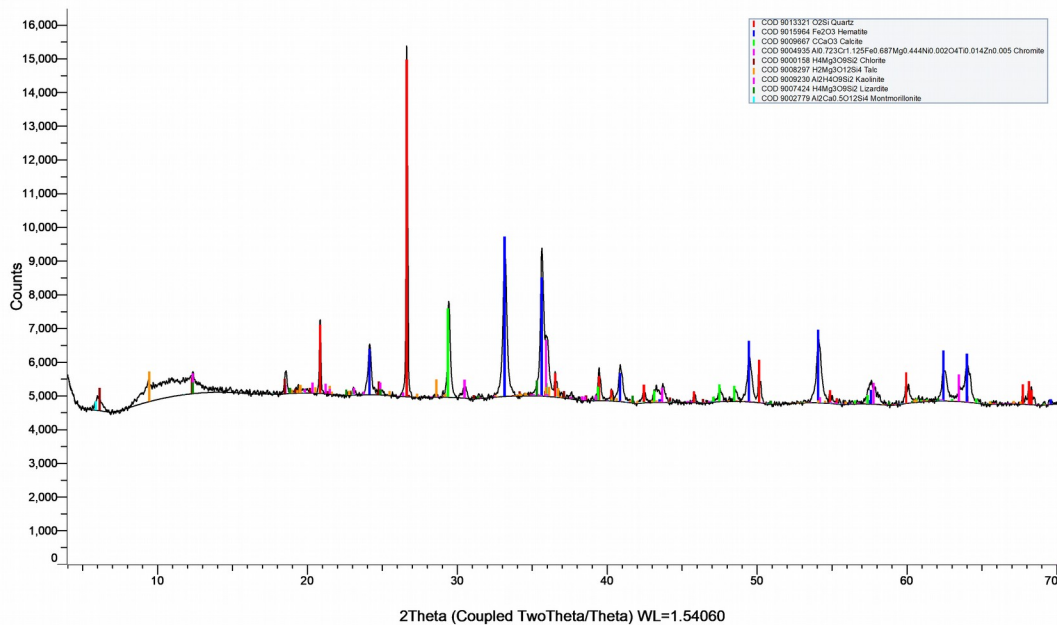
EB12 Bulk (Coupled TwoTheta/Theta)



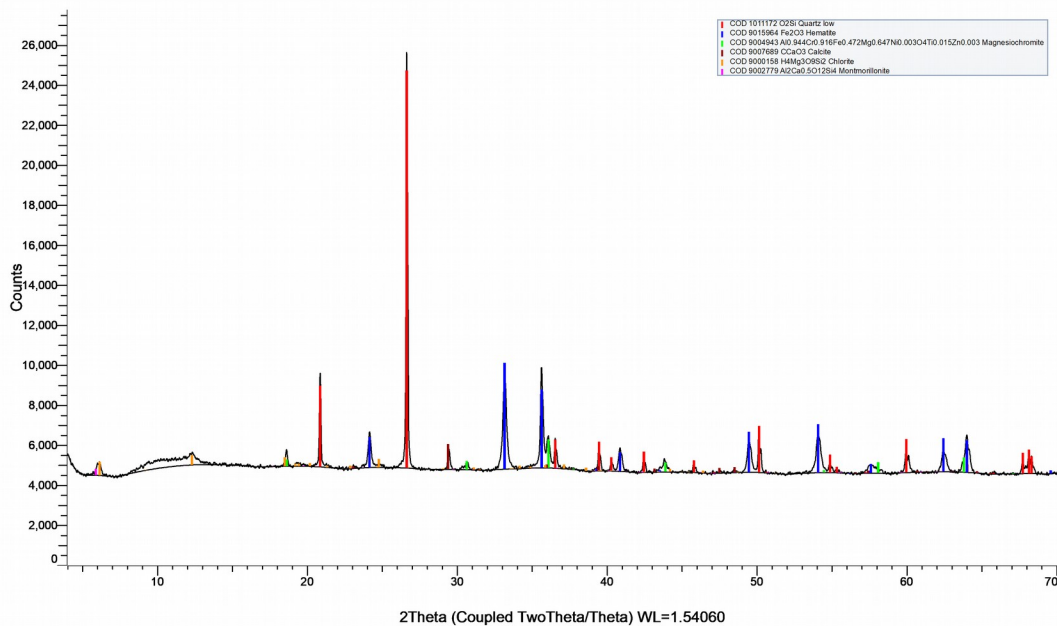
EB13 Bulk (Coupled TwoTheta/Theta)



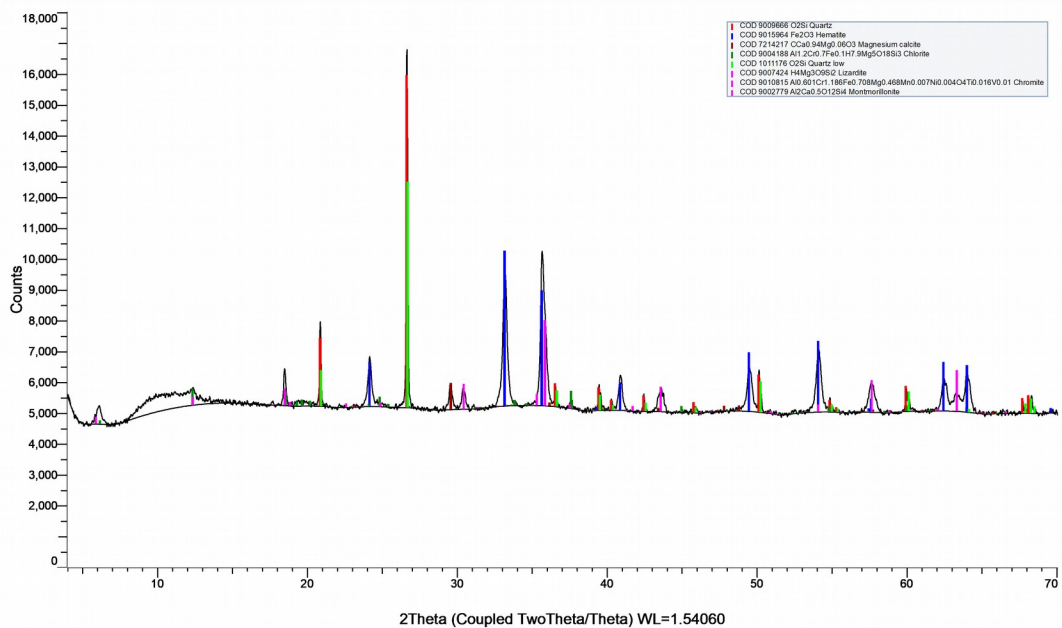
EB14 Bulk (Coupled TwoTheta/Theta)



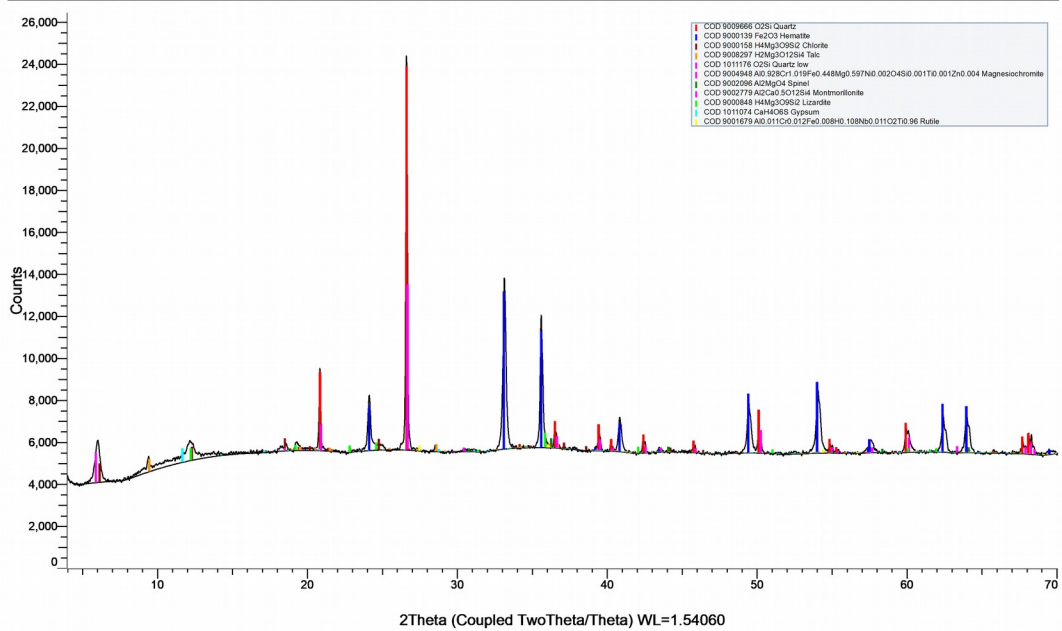
EB15 Bulk (Coupled TwoTheta/Theta)



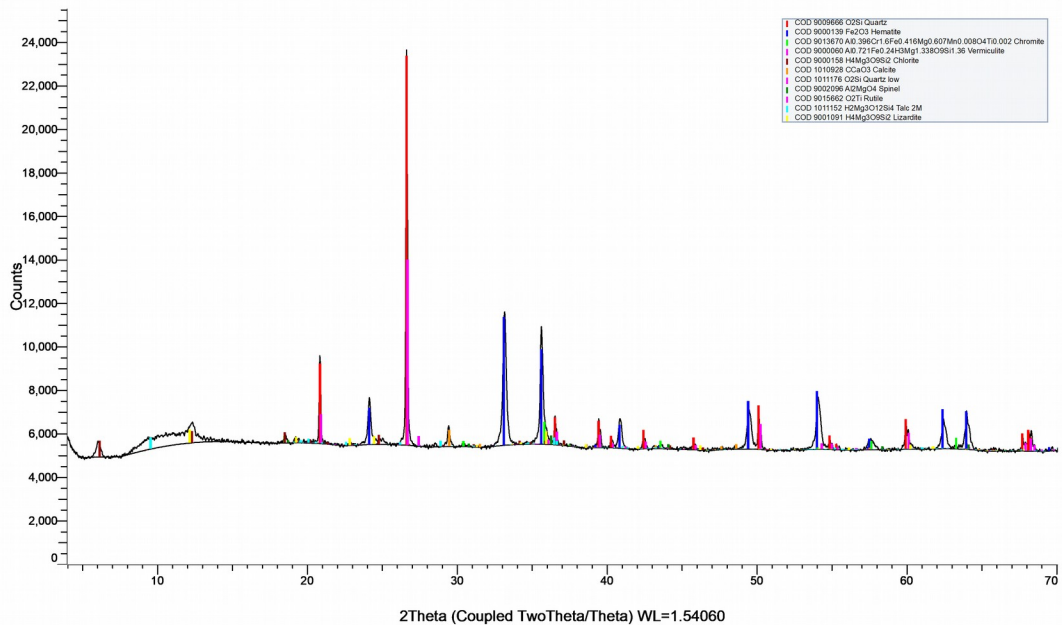
EB16 Bulk (Coupled TwoTheta/Theta)



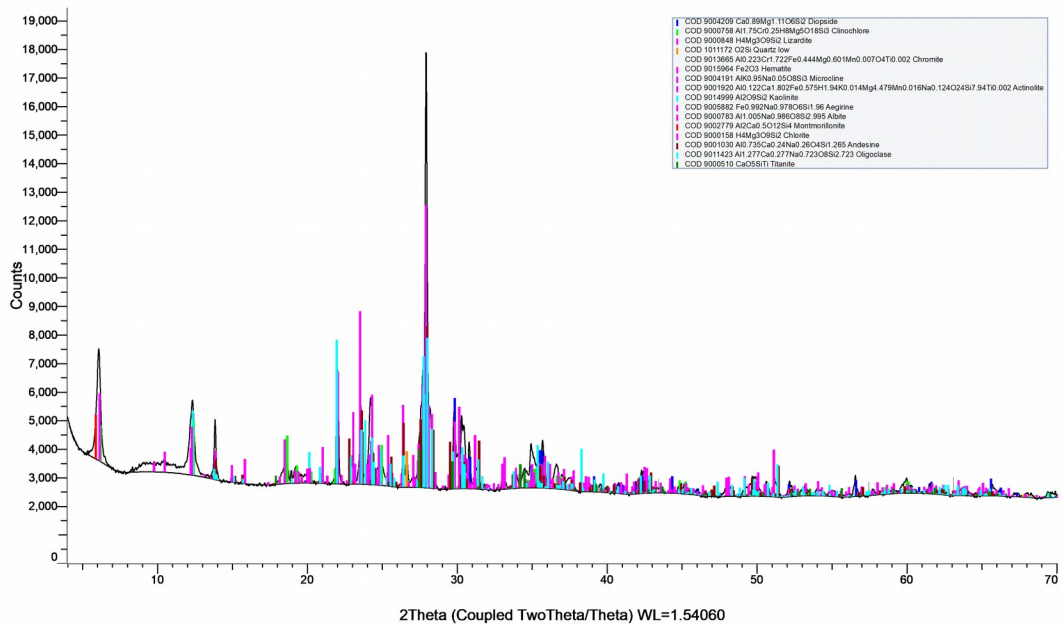
EB17 BULK (Coupled TwoTheta/Theta)



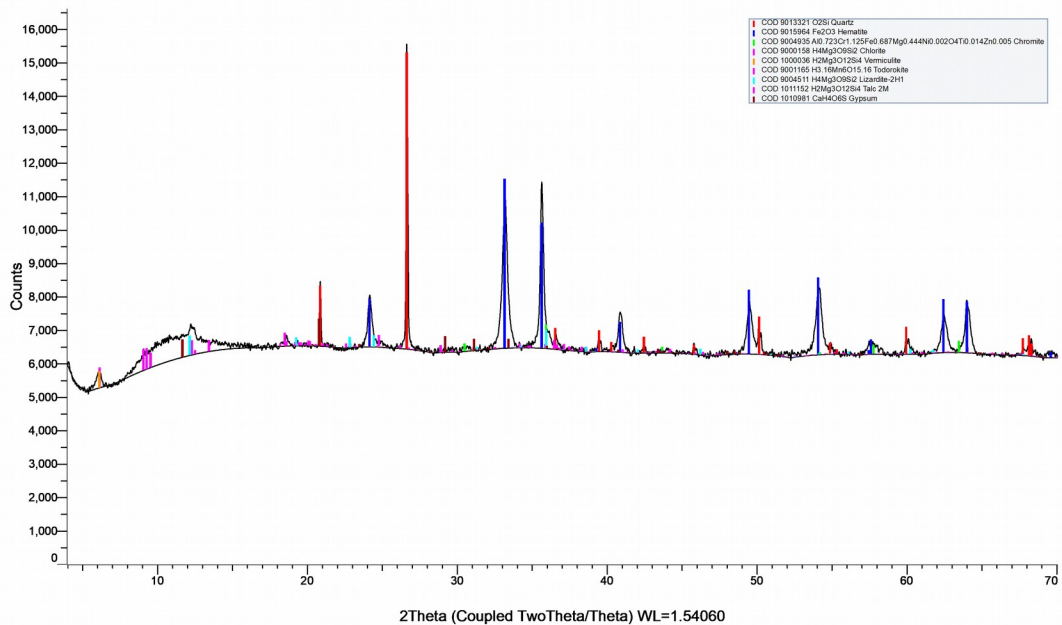
EB18A Bulk (Coupled TwoTheta/Theta)



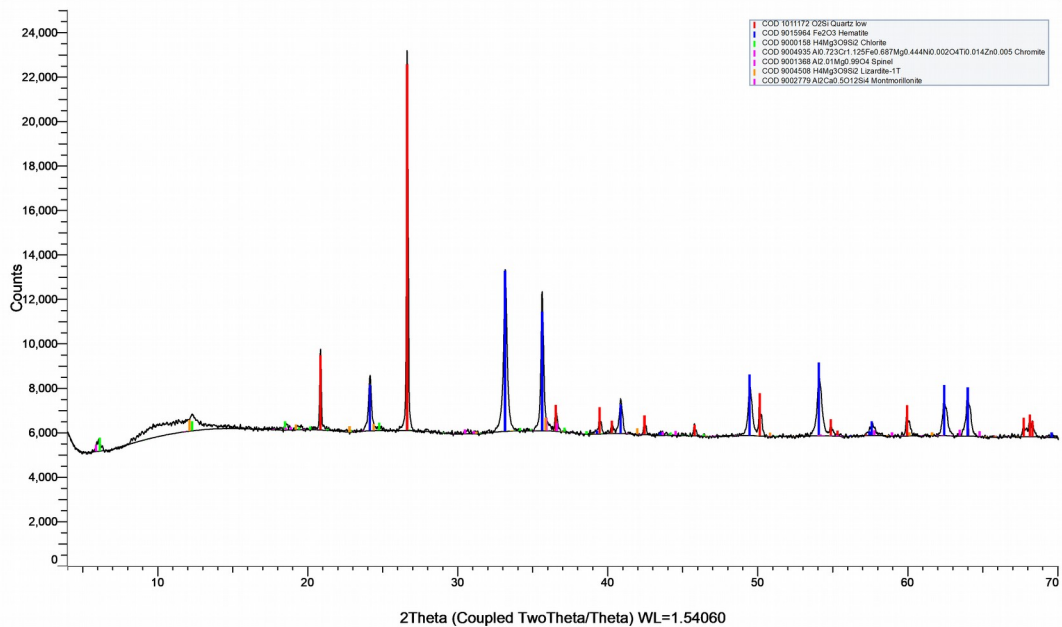
EB18B Bulk (Coupled TwoTheta/Theta)



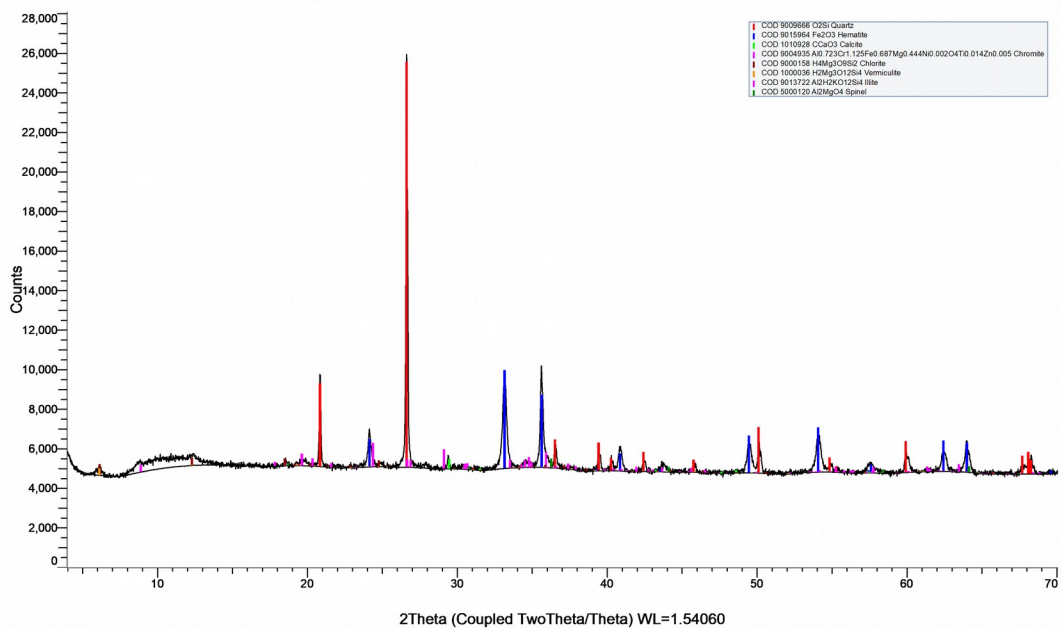
EB19 Bulk (Coupled TwoTheta/Theta)



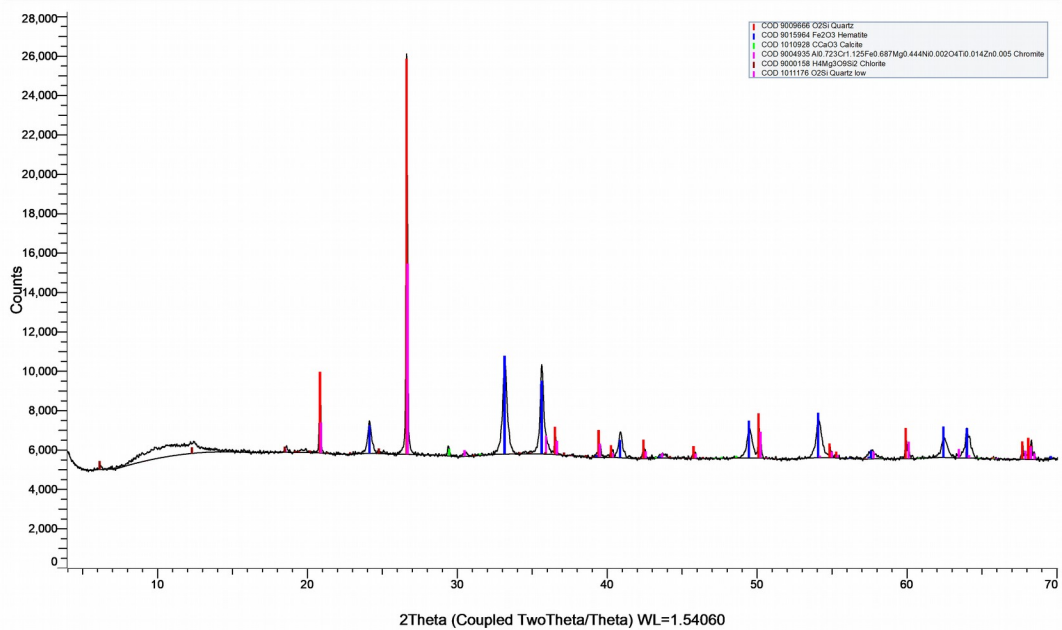
EB20 Bulk (Coupled TwoTheta/Theta)



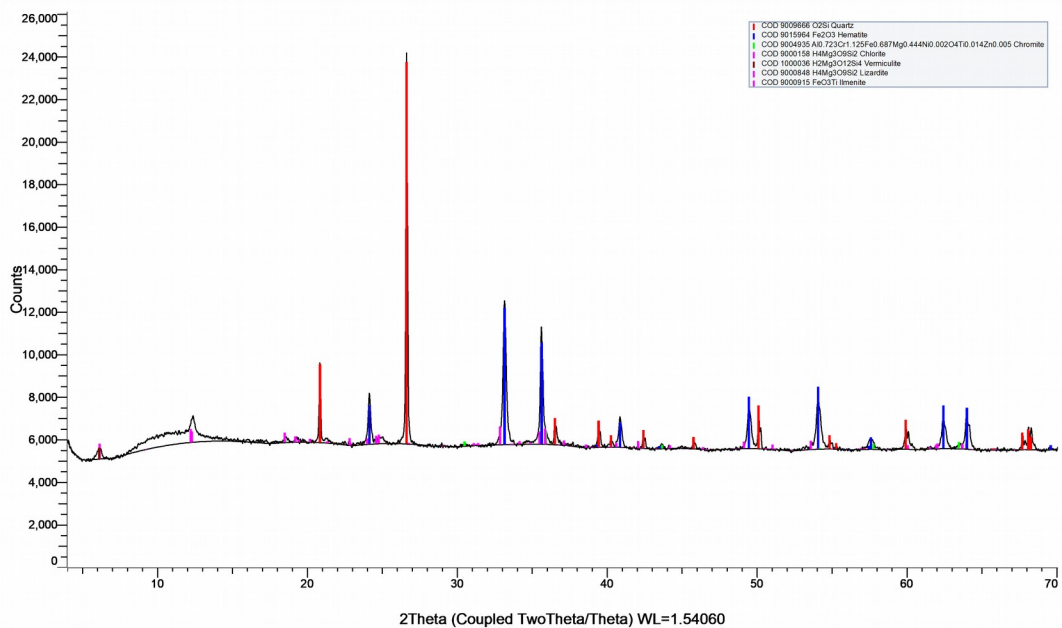
EB21 Bulk (Coupled TwoTheta/Theta)



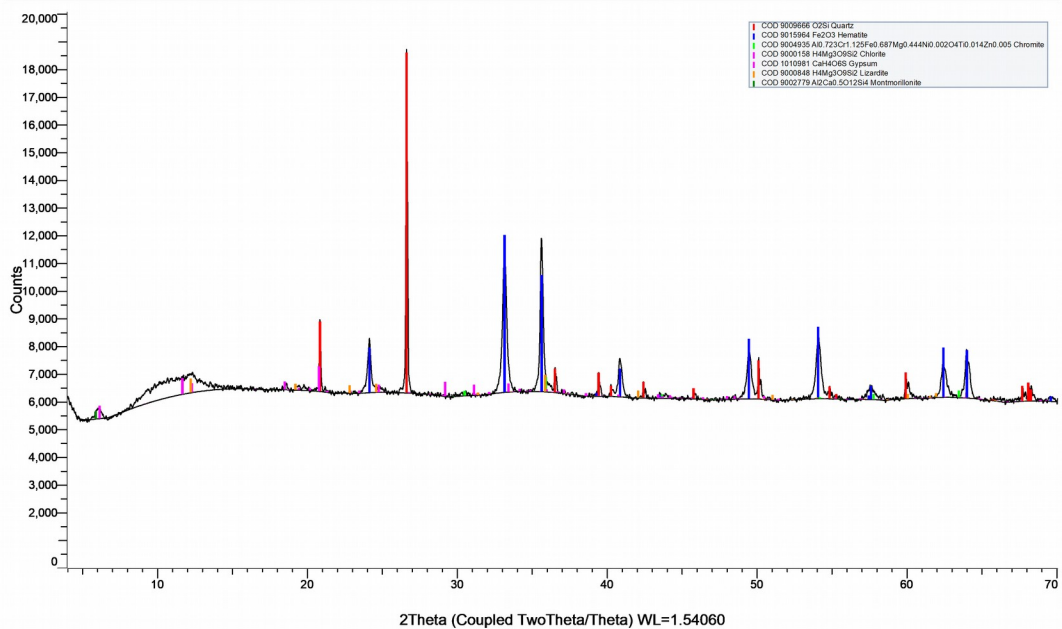
EB22 Bulk (Coupled TwoTheta/Theta)



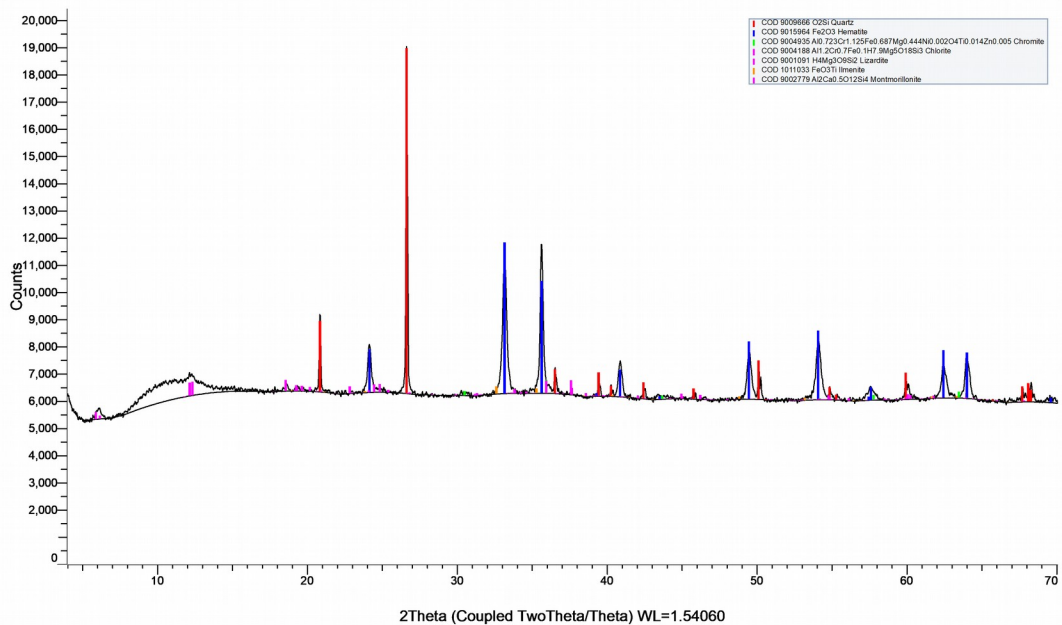
EB23 Bulk (Coupled TwoTheta/Theta)



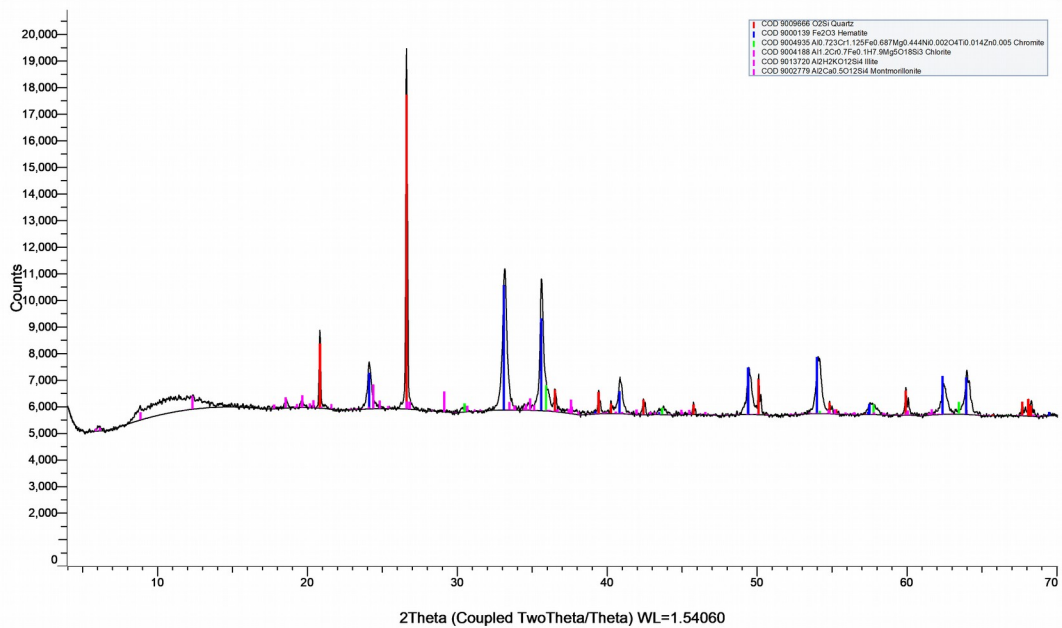
EB24 Bulk (Coupled TwoTheta/Theta)



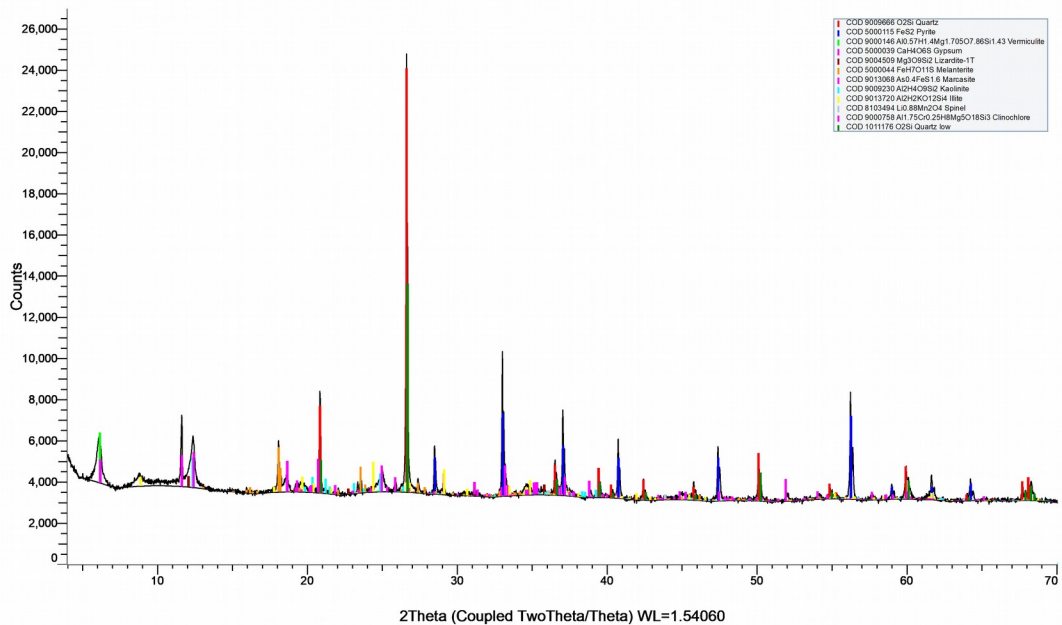
EB25 Bulk (Coupled TwoTheta/Theta)



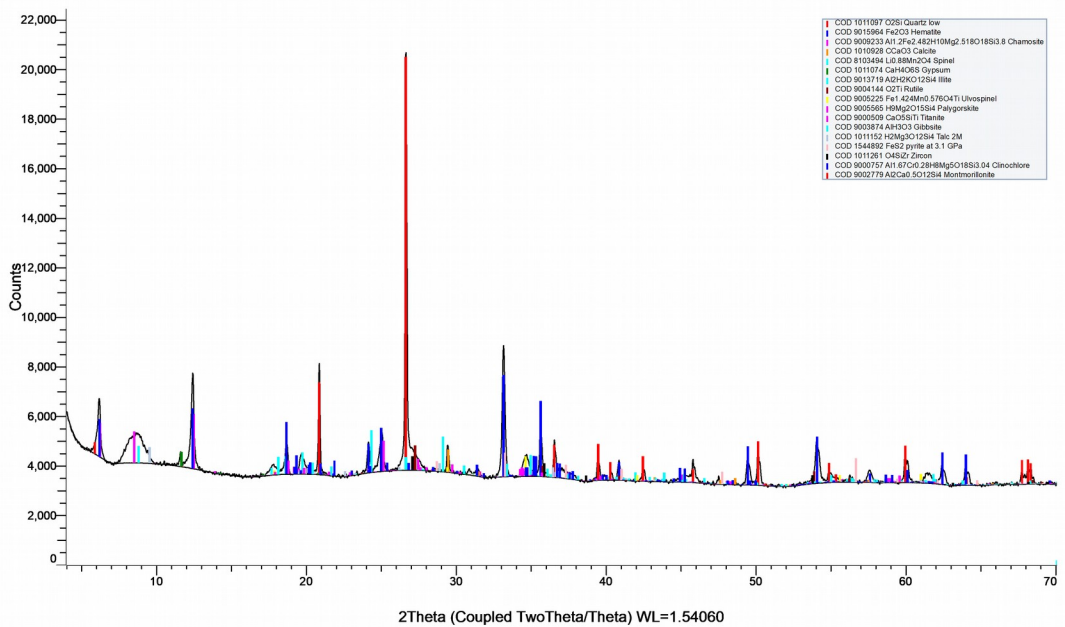
EB26 Bulk (Coupled TwoTheta/Theta)



EB27A Bulk (Coupled TwoTheta/Theta)

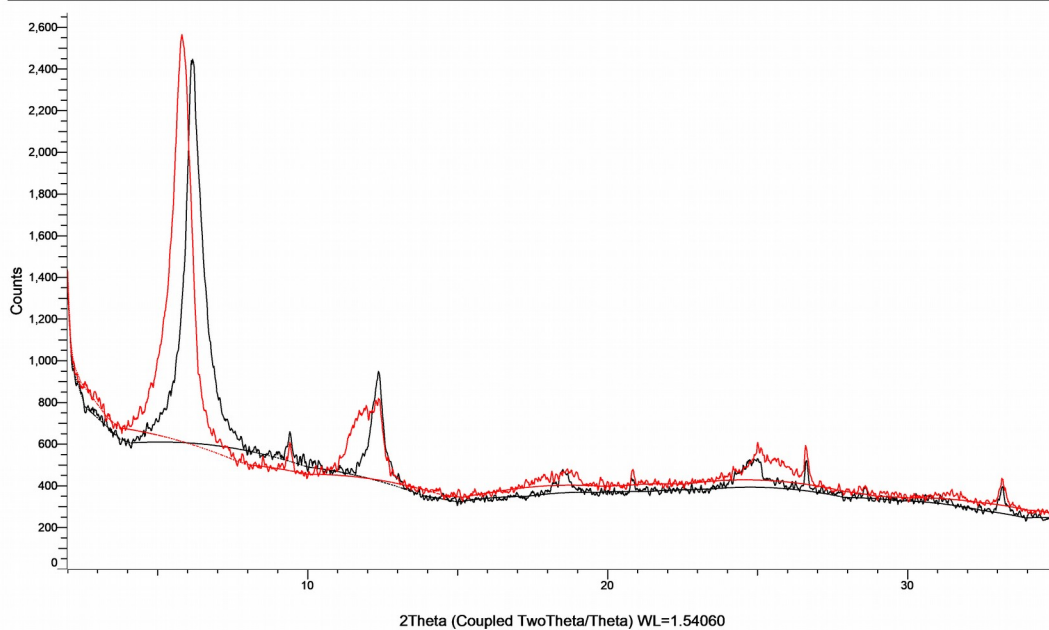


EB27B Bulk (Coupled TwoTheta/Theta)

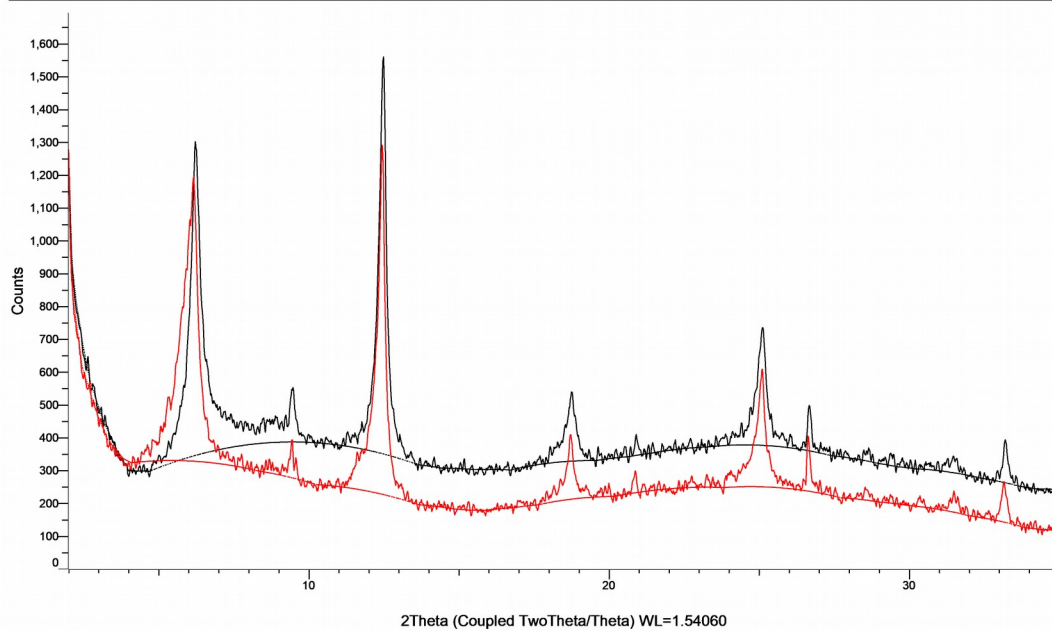


Clay fraction PXRD patterns of the remaining samples:

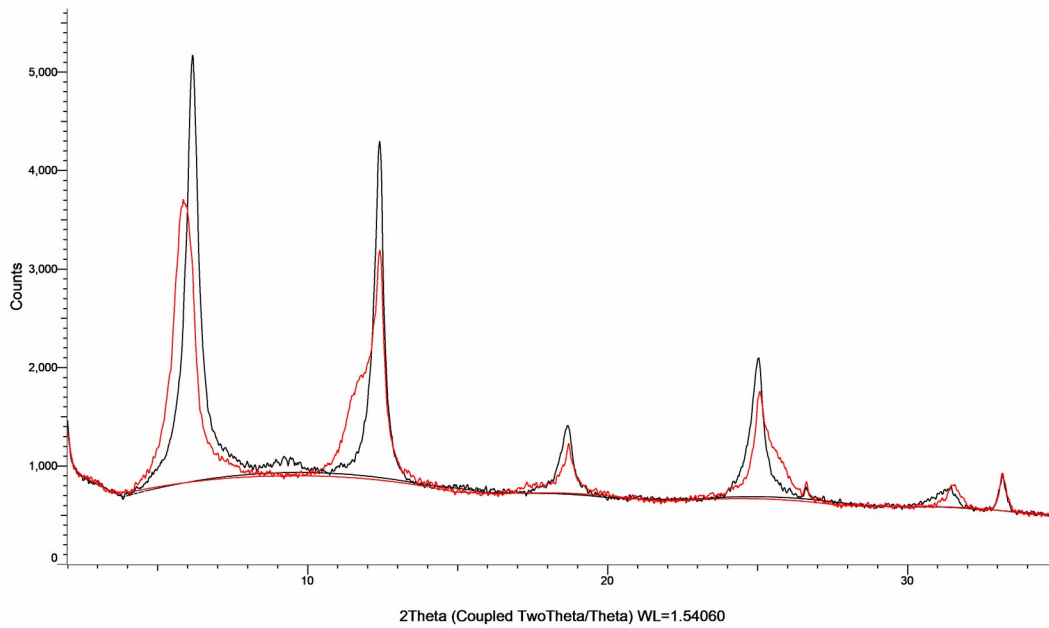
EB2 AD (Coupled TwoTheta/Theta)



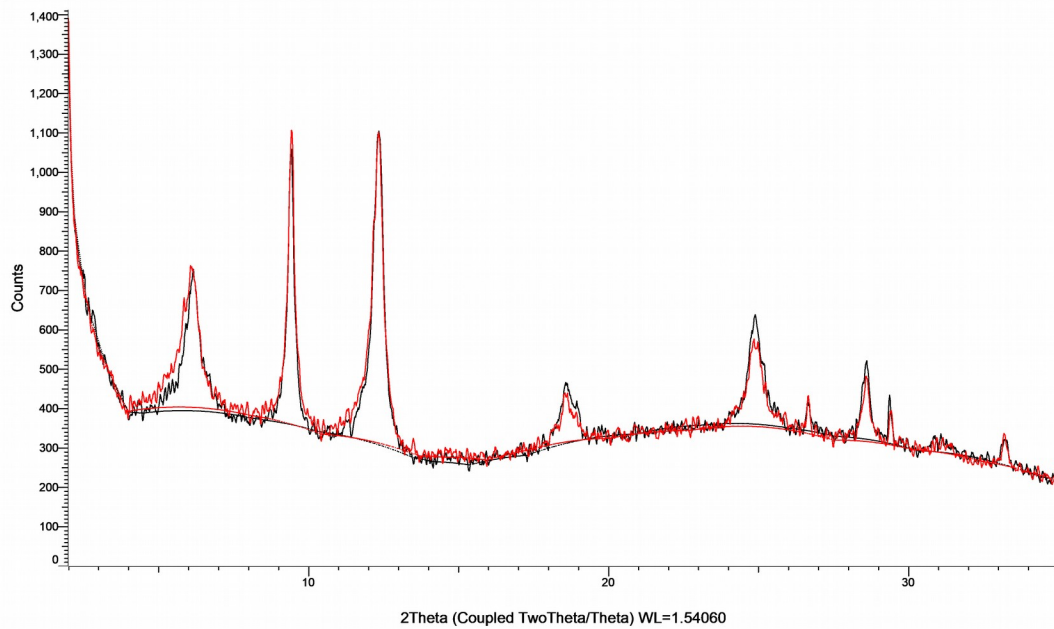
EB3 AD (Coupled TwoTheta/Theta)



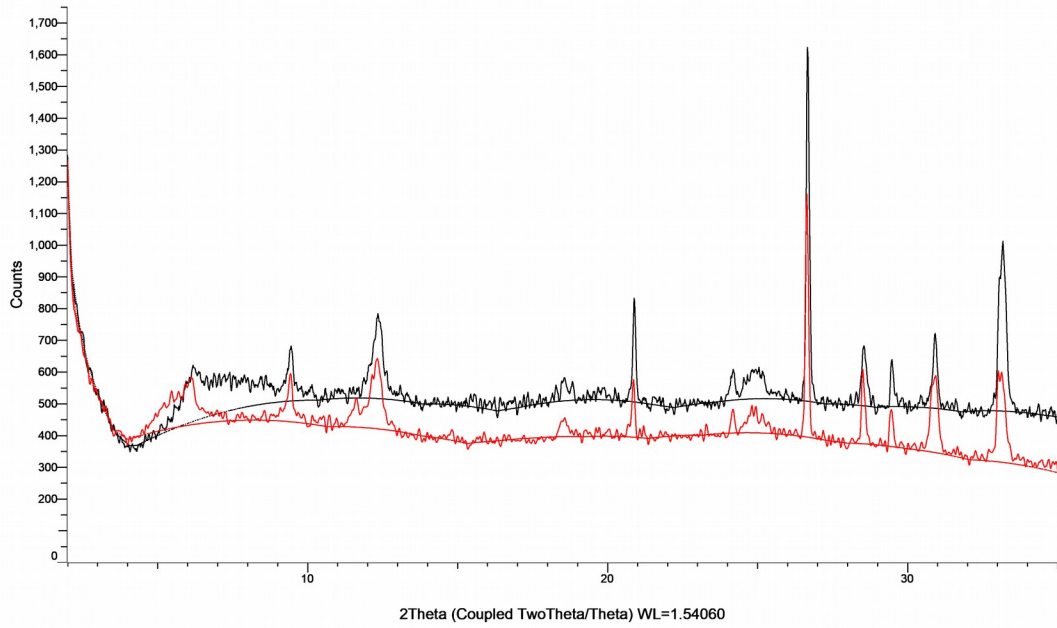
EB4 AD (Coupled TwoTheta/Theta)



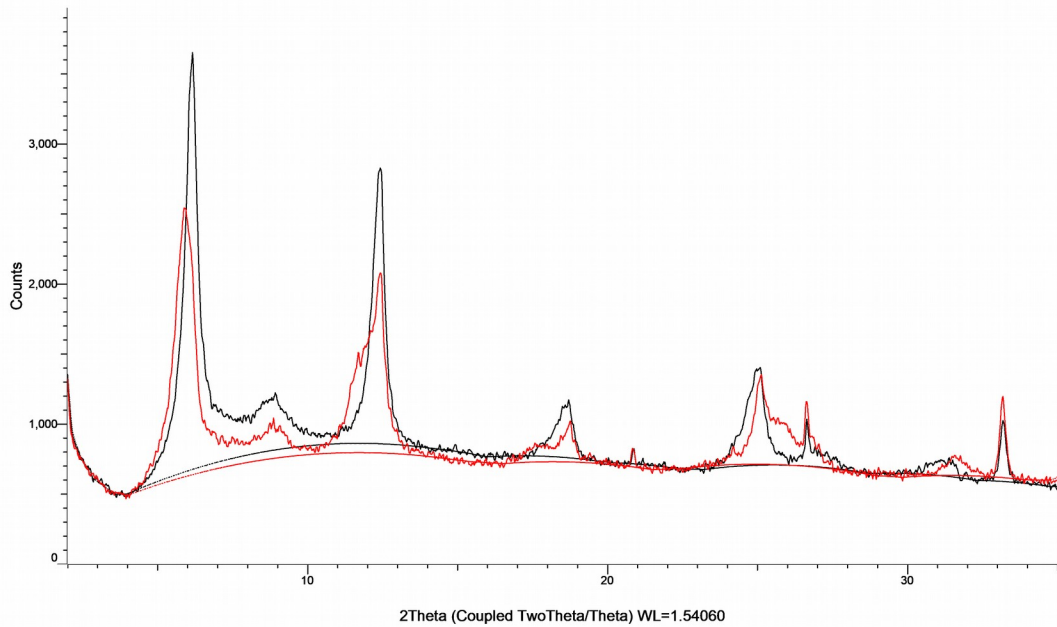
EB5A AD (Coupled TwoTheta/Theta)



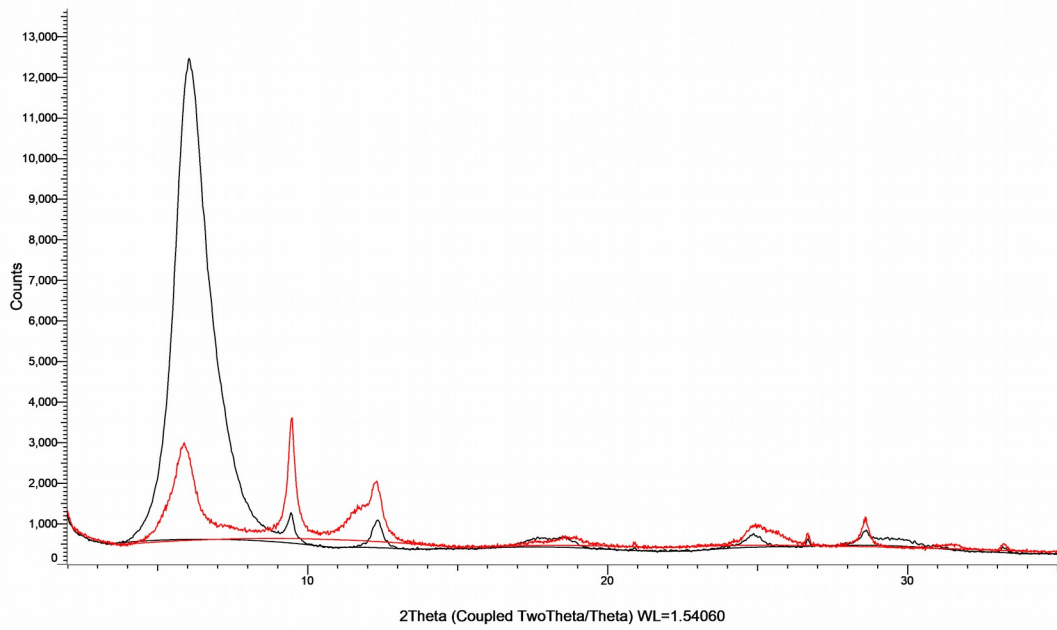
EB5B AD (Coupled TwoTheta/Theta)



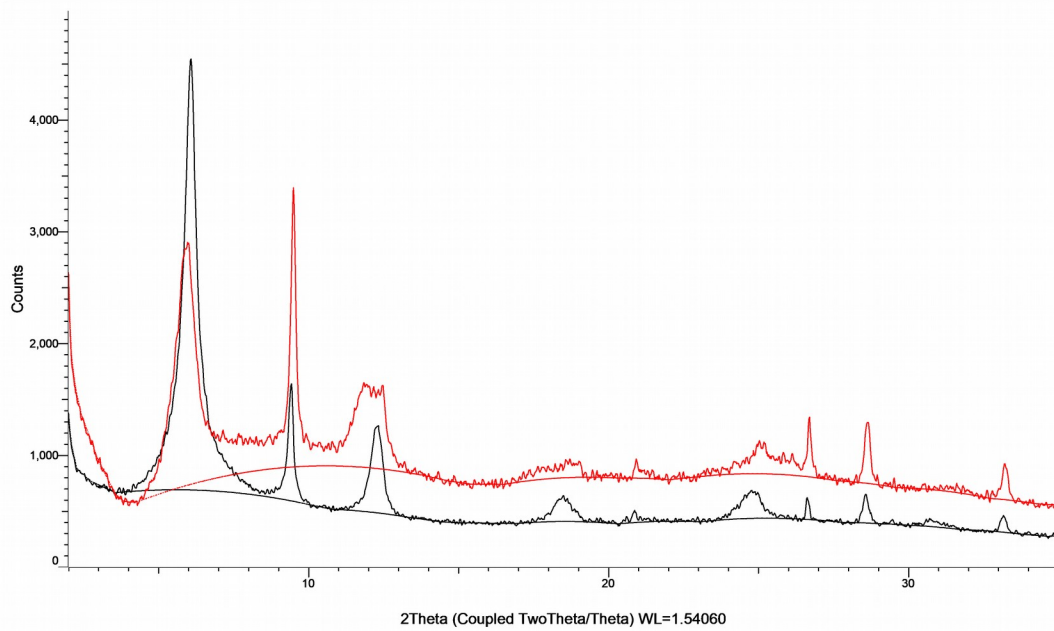
EB6 AD (Coupled TwoTheta/Theta)



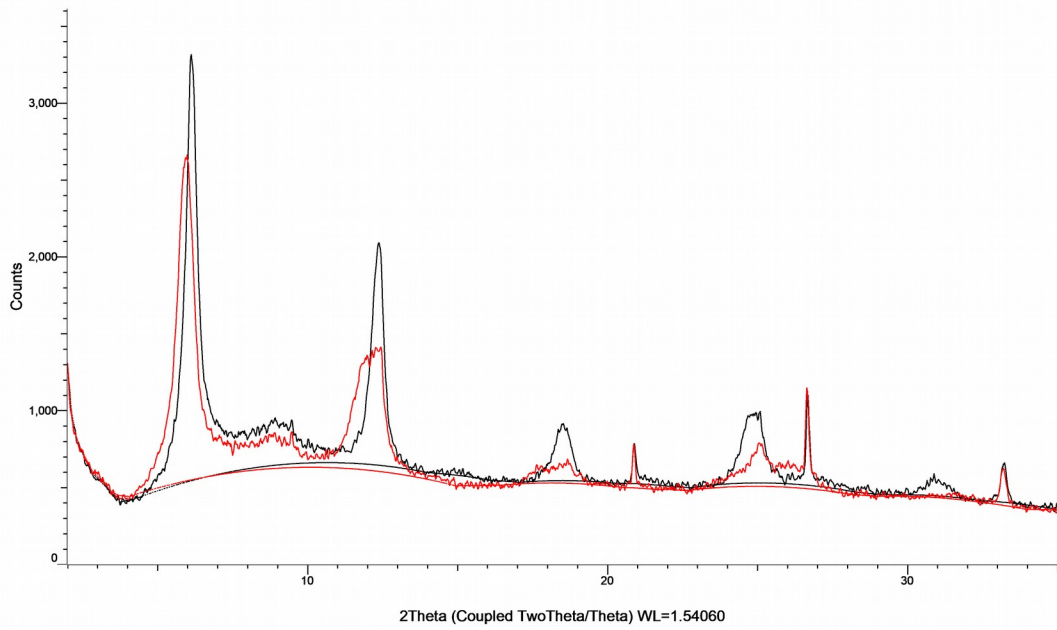
EB7 AD (Coupled TwoTheta/Theta)



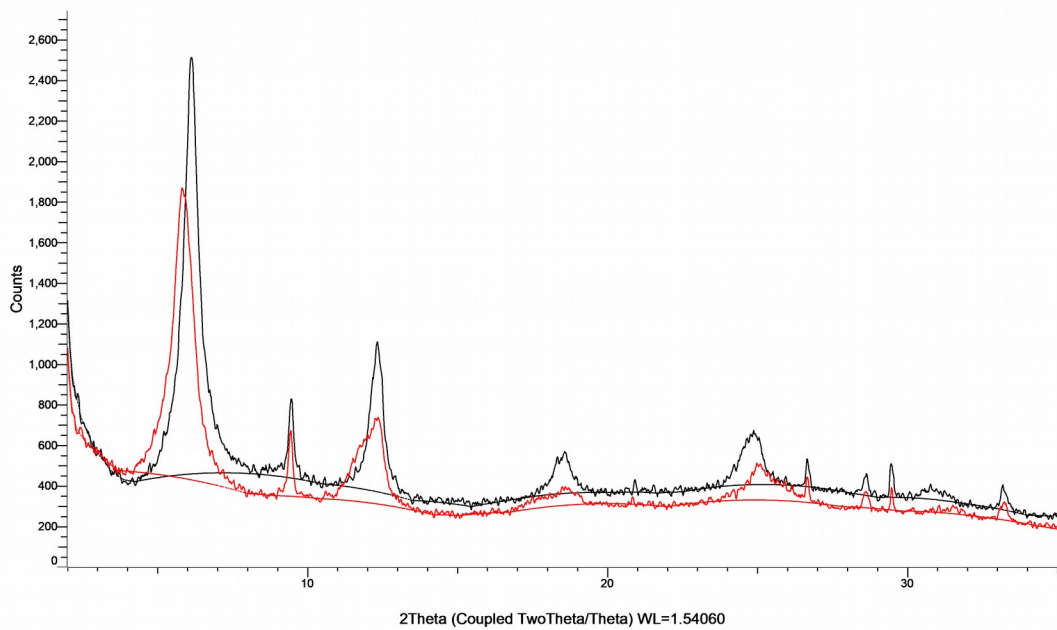
EB12 AD (Coupled TwoTheta/Theta)



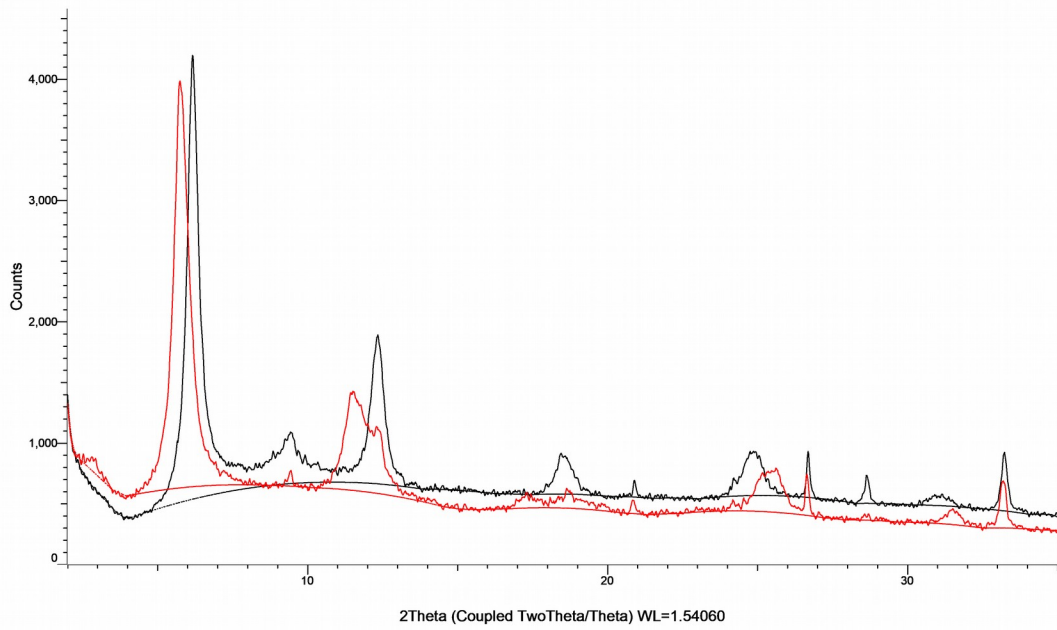
EB13 AD (Coupled TwoTheta/Theta)



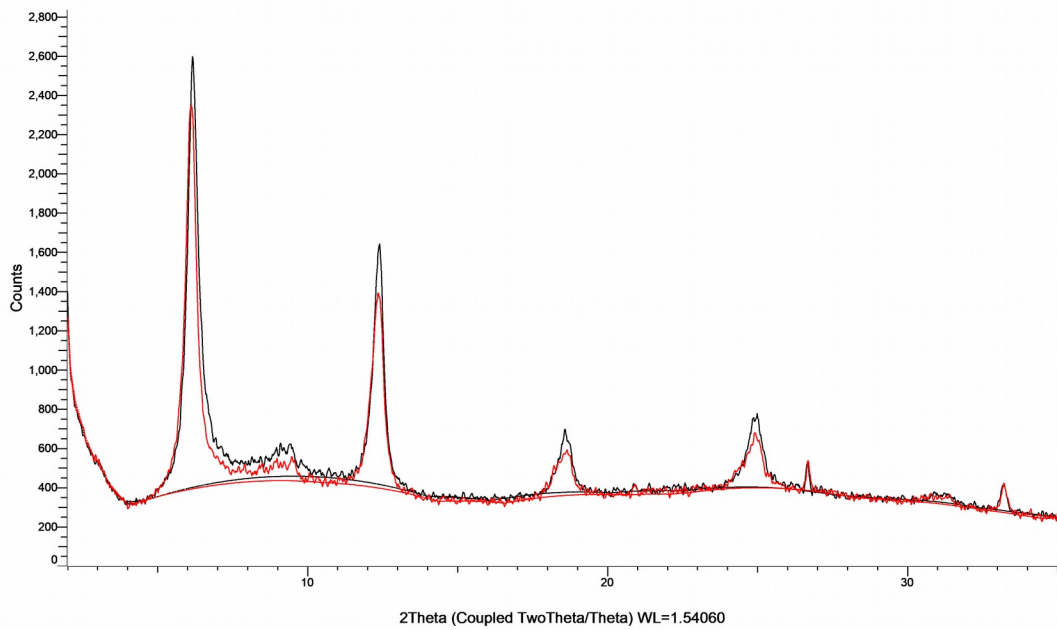
EB14 AD (Coupled TwoTheta/Theta)



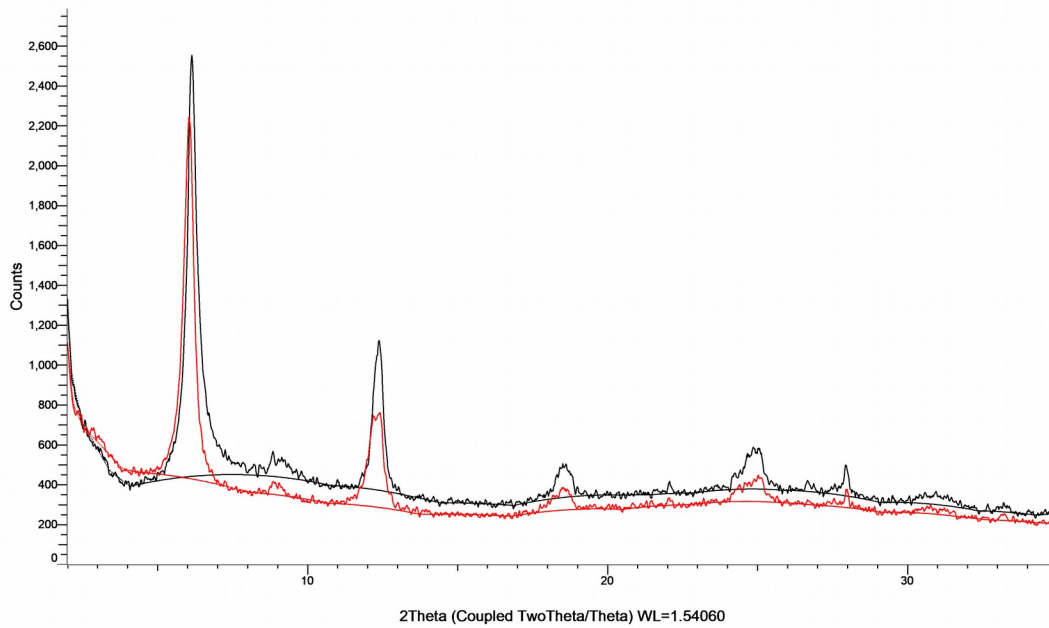
EB17 AD (Coupled TwoTheta/Theta)



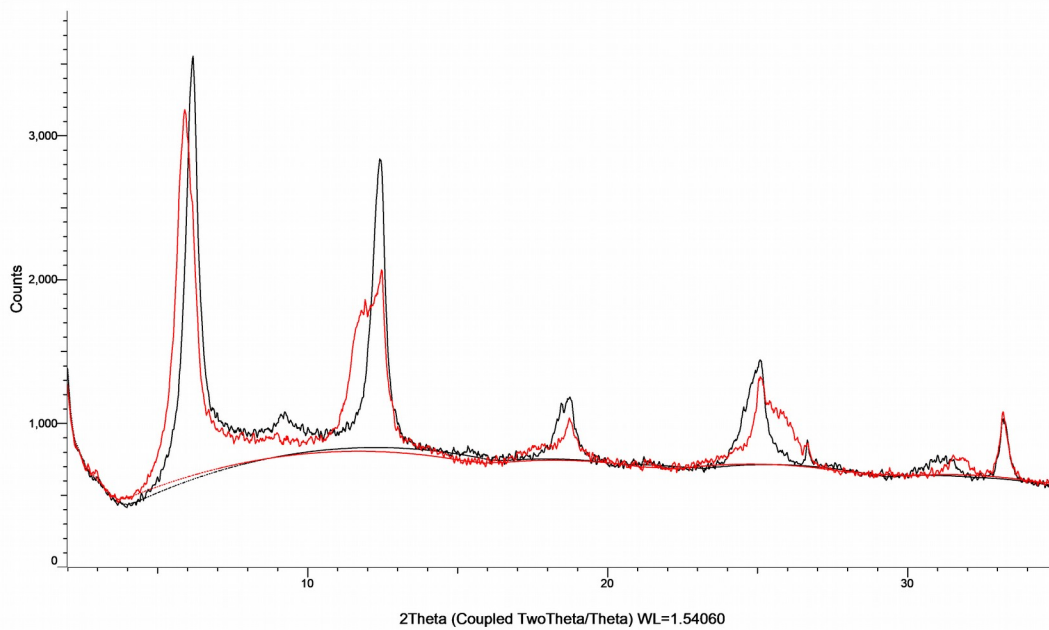
EB18A AD (Coupled TwoTheta/Theta)



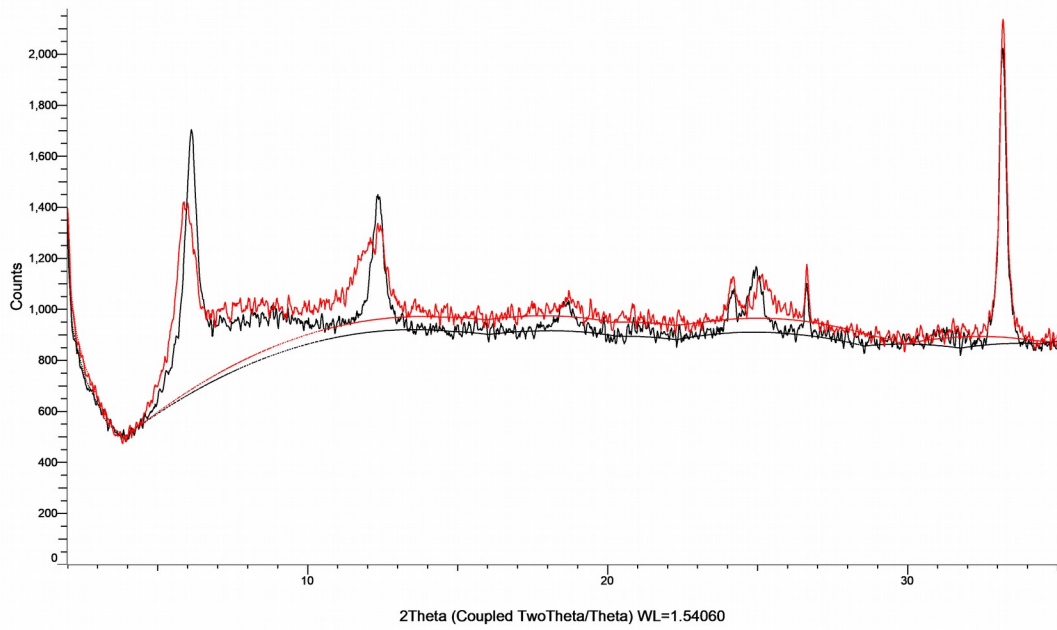
EB18B AD (Coupled TwoTheta/Theta)



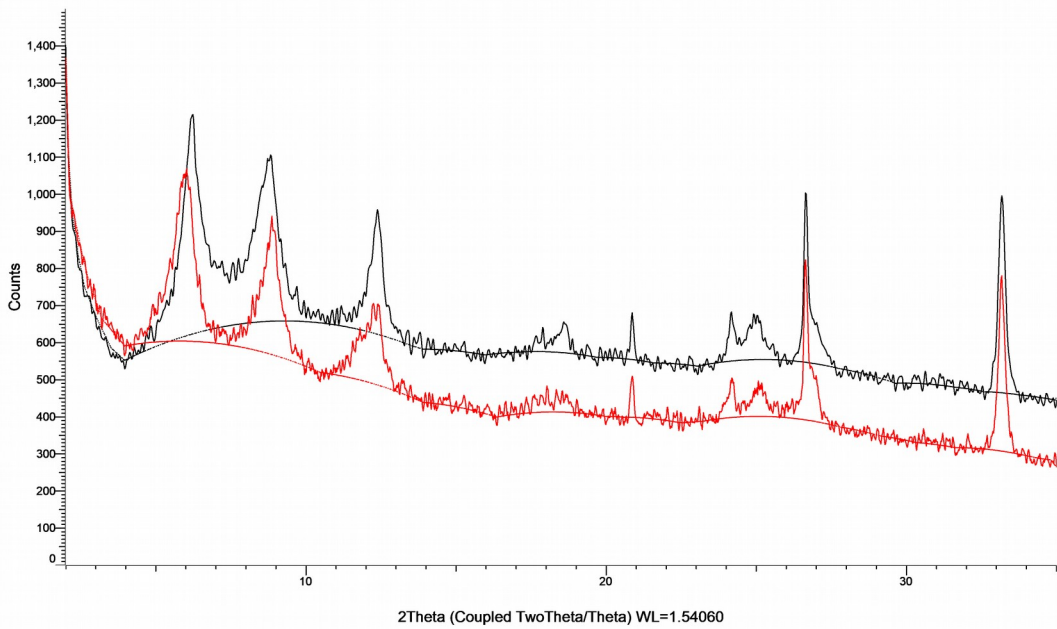
EB19 AD (Coupled TwoTheta/Theta)



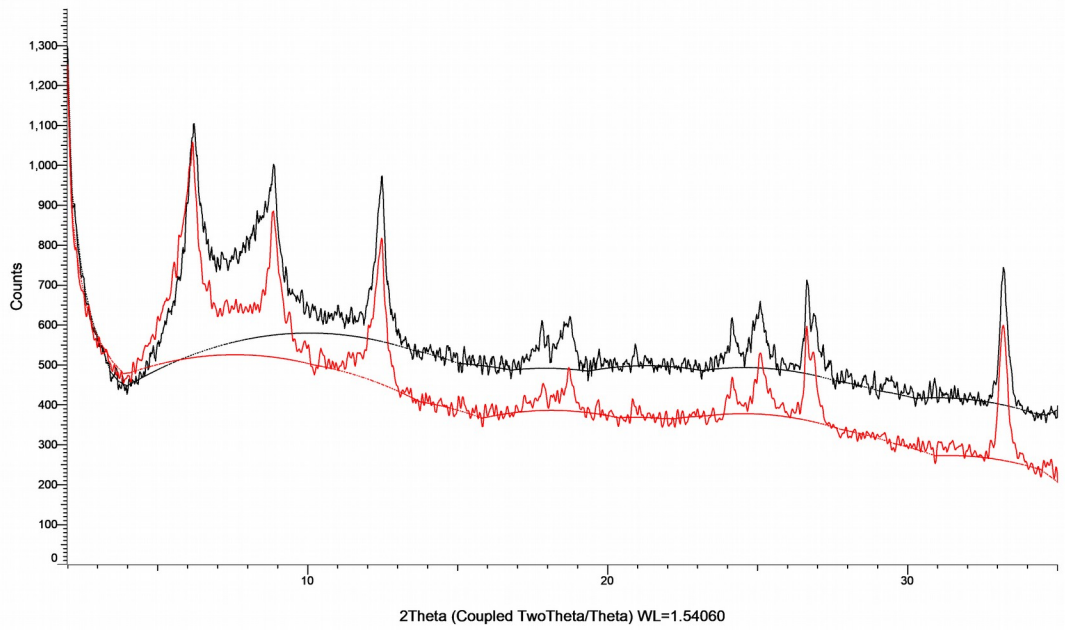
EB20 AD (Coupled TwoTheta/Theta)



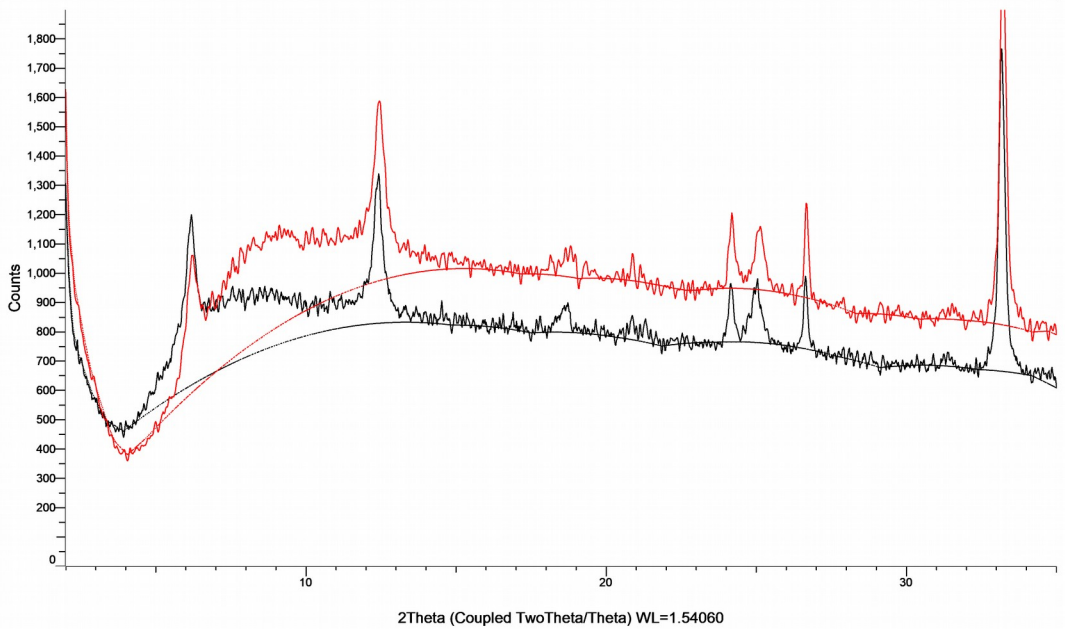
EB21 AD (Coupled TwoTheta/Theta)



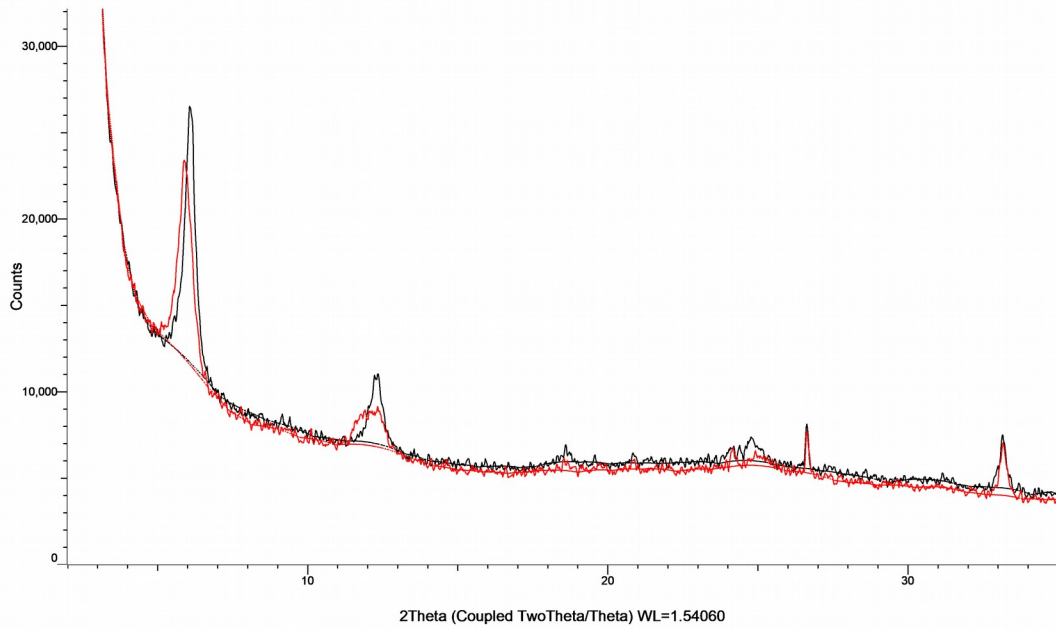
EB22 AD (Coupled TwoTheta/Theta)



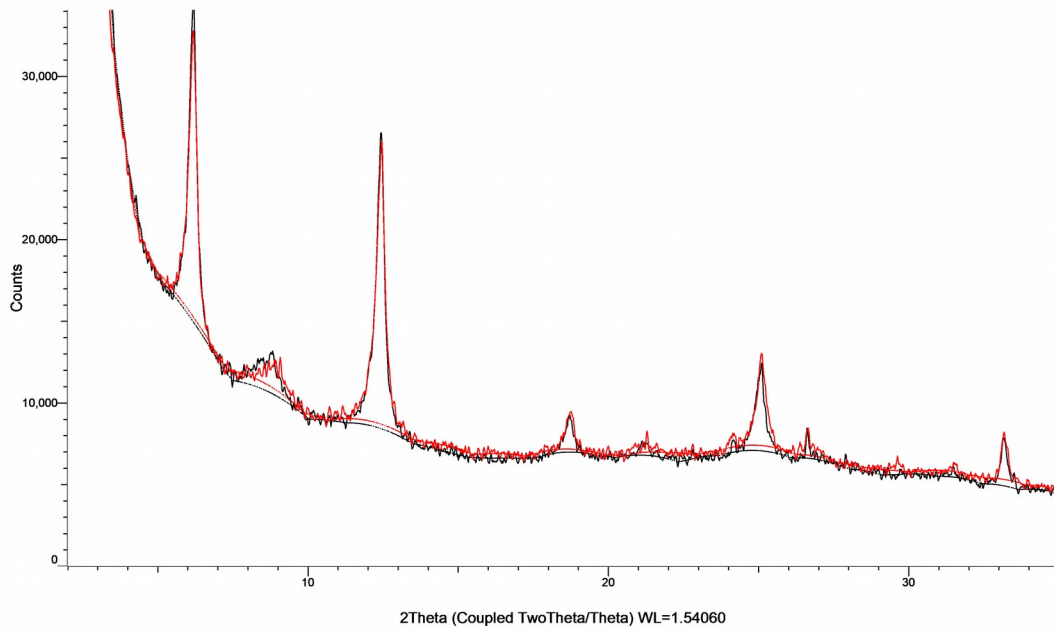
EB23 AD (Coupled TwoTheta/Theta)



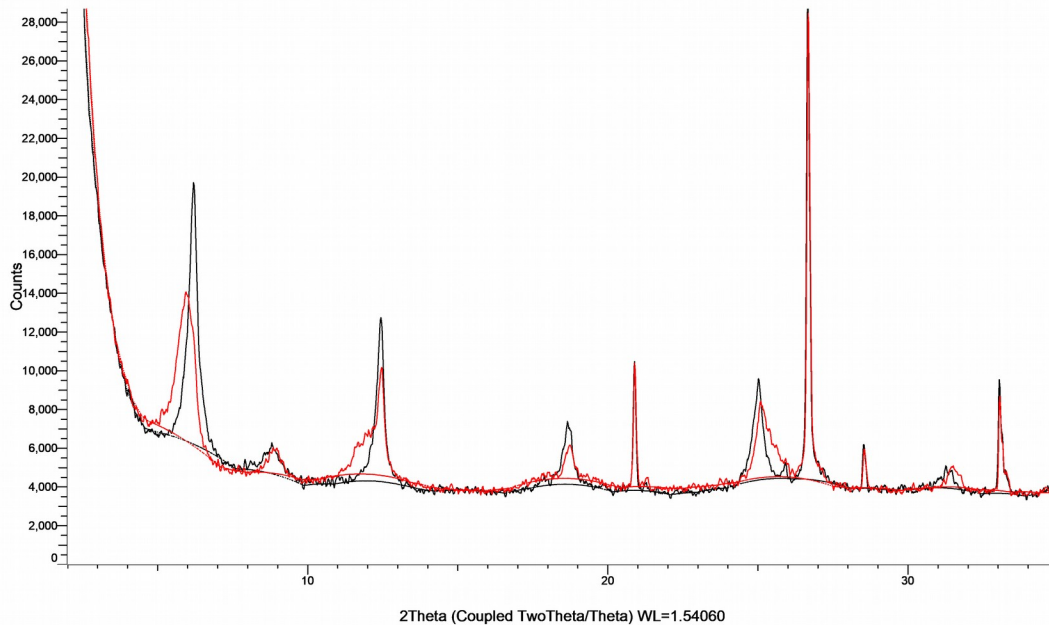
EB24 AD (Coupled TwoTheta/Theta)



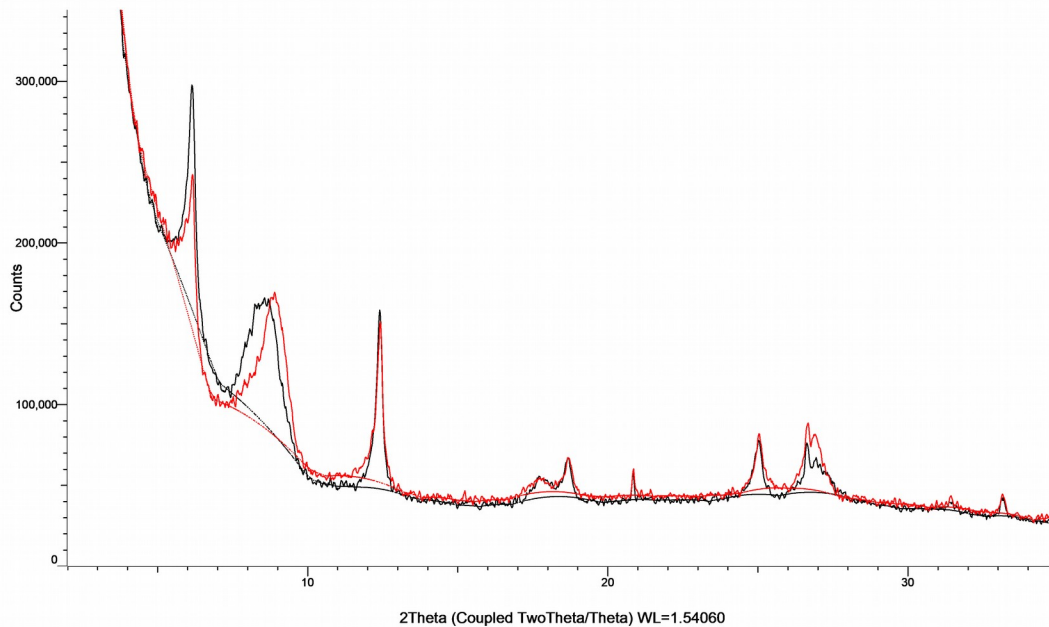
EB25 AD (Coupled TwoTheta/Theta)



EB27A AD (Coupled TwoTheta/Theta)



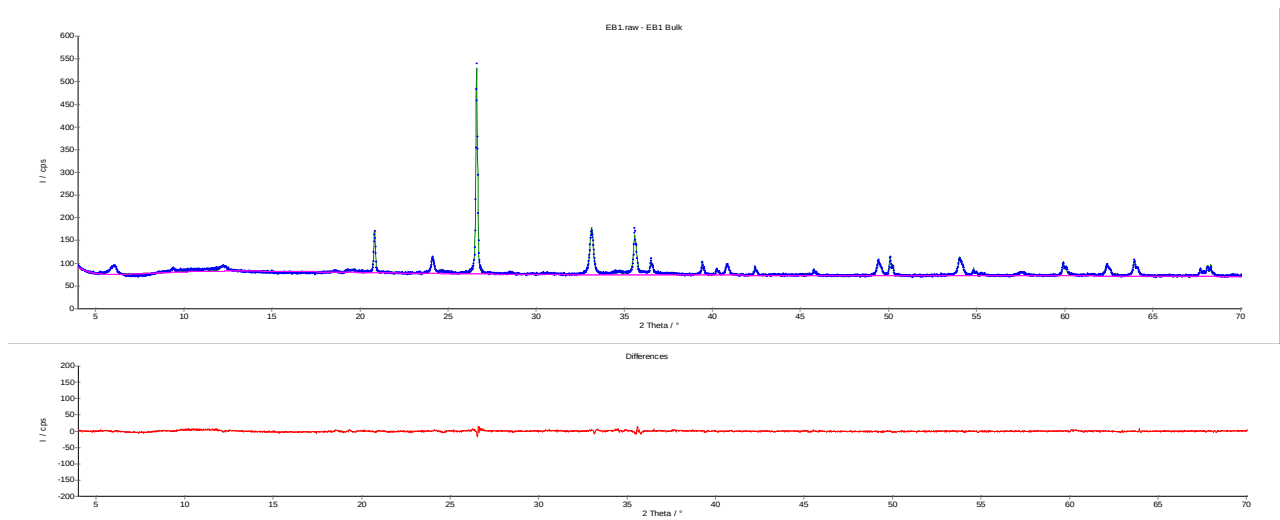
EB27B AD (Coupled TwoTheta/Theta)



Quantitative analyses with AutoQuan software:

EB1	wt(%)
Chlorite	3.89 ±0.90
Chromite Mg	2.04 ±0.81
Hematite	35.90 ±3.30
Lizardite	4.10 ±8.70
Quartz	43.90 ±4.20
Smectite	5.64 ±0.93
Spinel	1.13 ±0.69
Talc	3.40 ±0.75

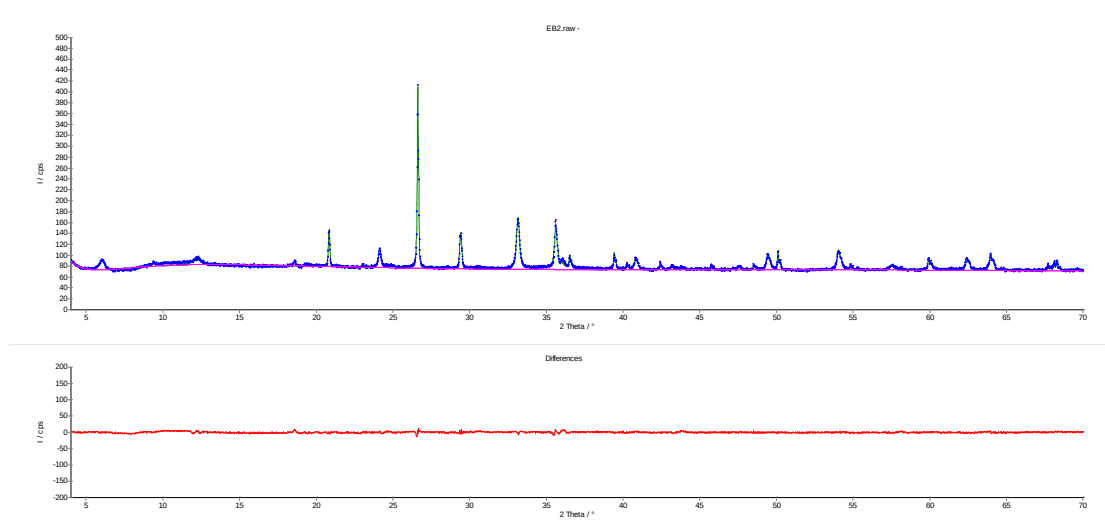
Rwp=2.42% Rexp=1.41%



EB2

Calcite	7.98	±1.02
Chlorite	10.05	±1.41
Chromite	1.19	±0.42
Chromite Mg	4.13	±0.69
Hematite	36.98	±1.29
Lizardite	1.00	±1.47
Quartz	32.39	±1.08
Smectite	2.32	±0.69
Spinel	0.14	±0.72
Talc	1.84	±0.66

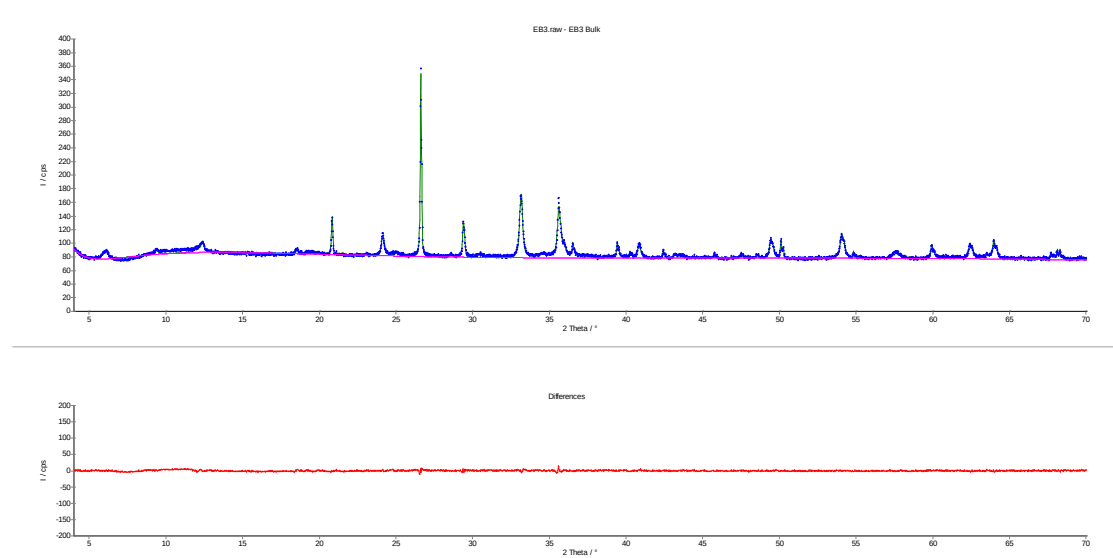
Rwp=2.19% Rexp=1.39%



EB3

Calcite	6.48 ±1.14
Chlorite	12.82 ±1.50
Chromite	1.35 ±0.48
Chromite Mg	5.95 ±1.14
Hematite	39.72 ±1.41
Lizardite	1.12 ±1.50
Quartz	27.33 ±0.96
Smectite	2.30 ±1.14
Talc	2.94 ±0.69

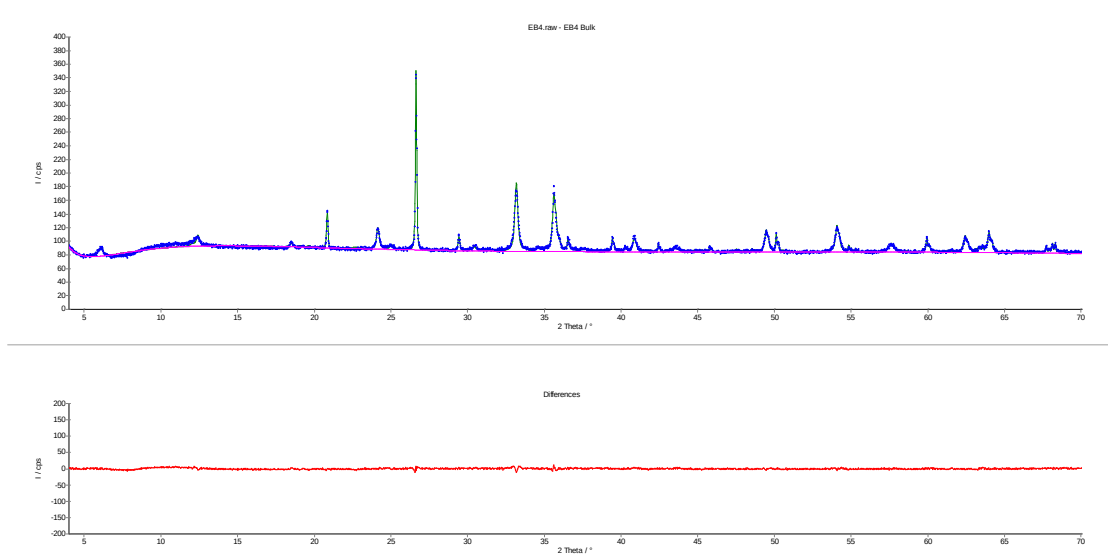
Rwp=2.10% Rexp=1.36%



EB4

Calcite	3.44	±0.72
Chlorite	10.97	±1.59
Chromite Mg	7.52	±1.38
Hematite	46.98	±1.68
Lizardite	0.85	±2.01
Quartz	28.90	±1.08
Smectite	1.36	±0.81

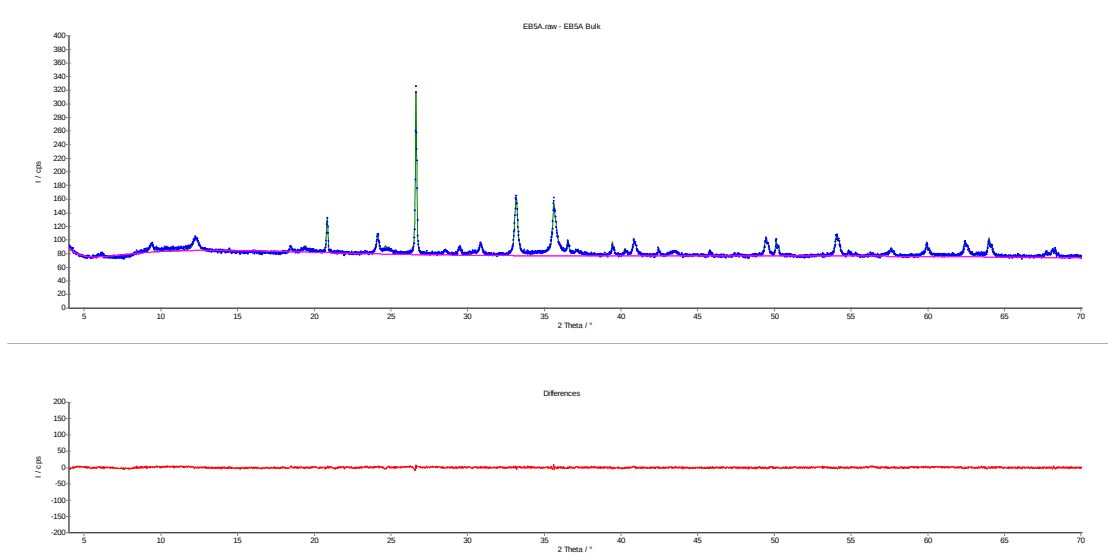
Rwp=2.10% Rexp=1.32%



EB5A

Calcite	5.66	±1.47
Chlorite	12.28	±1.74
Chromite	3.34	±0.63
Dolomite	6.97	±1.02
Hematite	33.99	±1.53
Lizardite	0.90	±2.43
Quartz	23.71	±1.11
Smectite	0.59	±0.92
Talc	13.09	±1.29

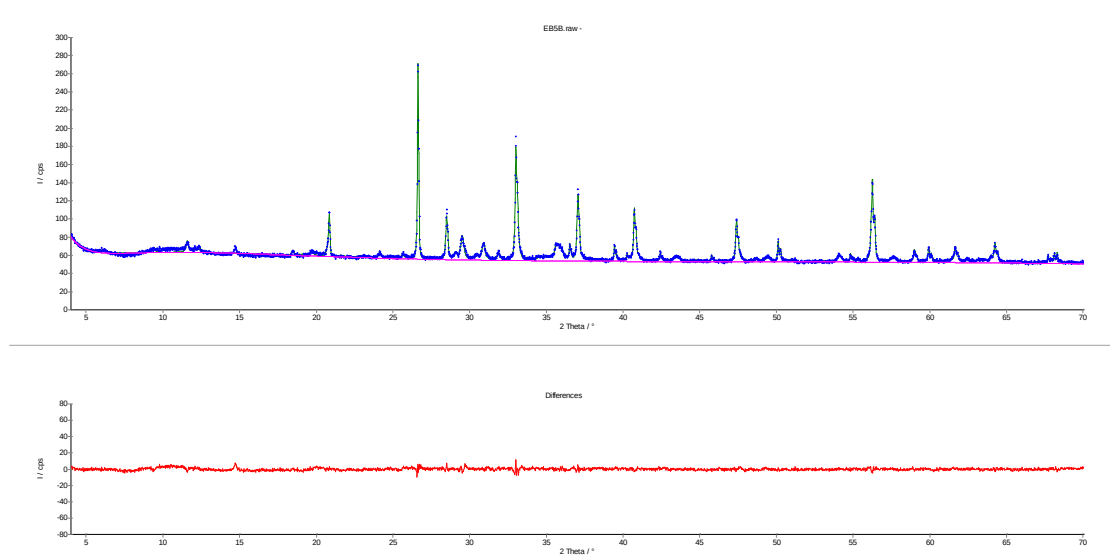
Rwp=2.19% Rexp=1.37%



EB5B

Anhydrite	1.20	±0.48
Calcite	4.24	±1.41
Chlorite	7.16	±1.11
Chromite	4.71	±0.81
Dolomite	3.15	±1.23
Gypsum	6.16	±1.17
Hematite	7.31	±1.05
Lizardite	2.77	±0.93
Pyrite	34.24	±1.17
Quartz	21.15	±0.78
Smectite	1.46	±0.90
Talc	6.45	±1.23

Rwp=2.38% Rexp=1.61%



EB6

Chlorite 10.97 ±1.35

Chromite Mg 3.56 ±0.81

Gypsum 1.55 ±0.57

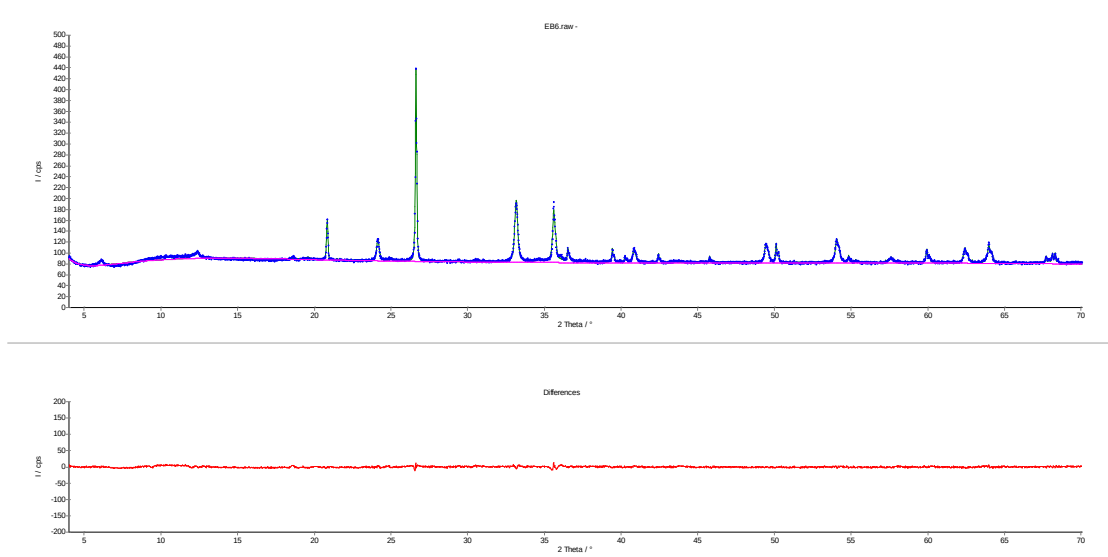
Hematite 45.24 ±1.20

Lizardite 1.70 ±0.51

Quartz 36.37 ±0.96

Smectite 0.62 ±0.30

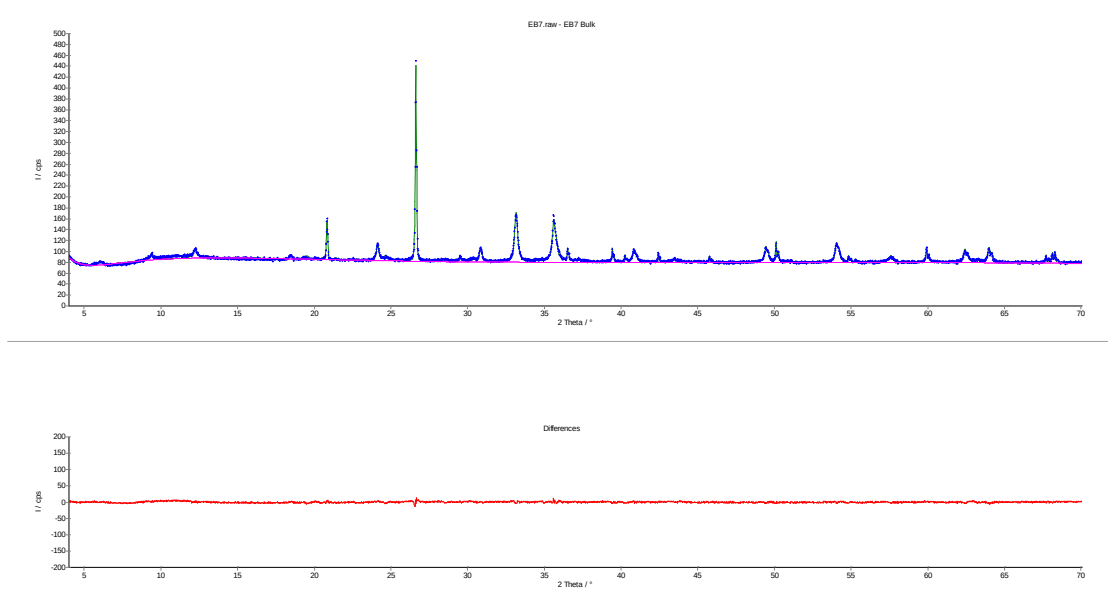
Rwp=2.13% Rexp=1.34%



EB7

Calcite	3.46	±1.05
Chlorite	5.78	±1.80
Chromite	4.40	±0.66
Dolomite	6.52	±1.26
Hematite	37.03	±2.58
Lizardite	0.60	±6.00
Quartz	31.18	±2.25
Smectite	0.69	±0.51
Talc	10.27	±1.41

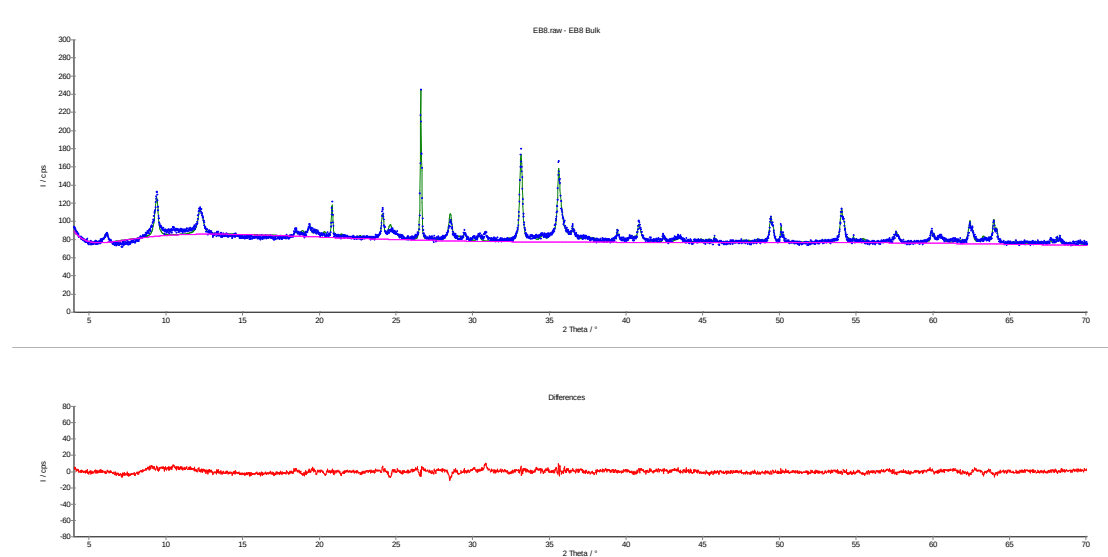
Rwp=2.07% Rexp=1.35%



EB8

Actinolite	6.87 ±0.99
Calcite	3.31 ±1.38
Chlorite	14.49 ±1.83
Chromite Mg	4.04 ±1.08
Dolomite	4.02 ±1.05
Hematite	26.32 ±1.29
Lizardite	1.86 ±1.50
Magnetite	3.09 ±0.78
Quartz	12.75 ±0.63
Smectite	0.49 ±0.33
Talc	22.76 ±1.53

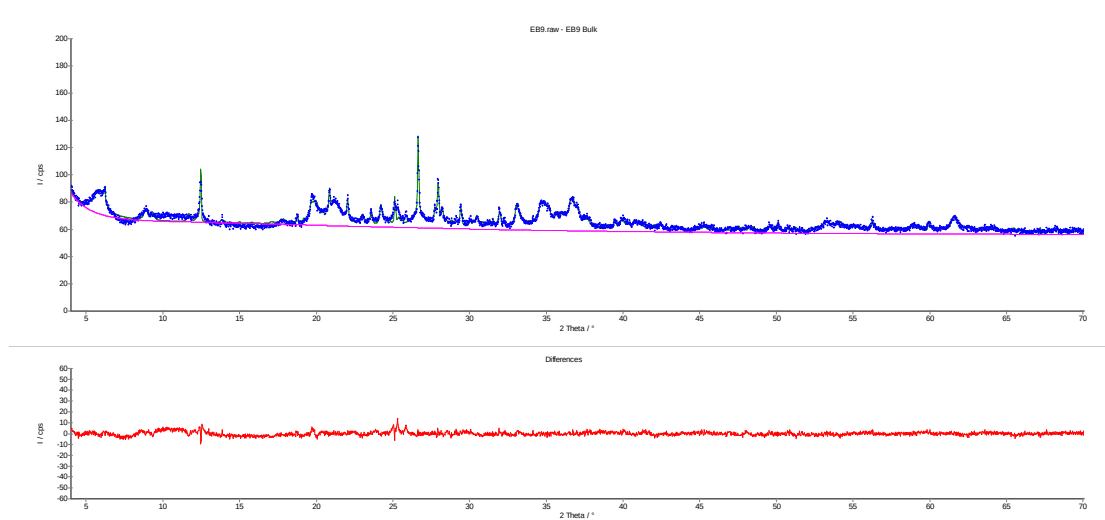
Rwp=2.36% Rexp=1.36%



EB9

Calcite	1.70	±0.48
Chlorite	4.30	±0.96
Goethite	24.70	±2.70
Gypsum	1.40	±3.90
Hematite	1.94	±0.81
Illite	26.15	±2.88
Ilmenite	0.46	±0.29
Lizardite	3.81	±0.87
Monazite	1.70	±0.39
Albite	12.61	±1.05
Pyrite	2.16	±0.60
Quartz	4.09	±0.48
Smectite	9.43	±1.59
Talc	15.54	±1.23

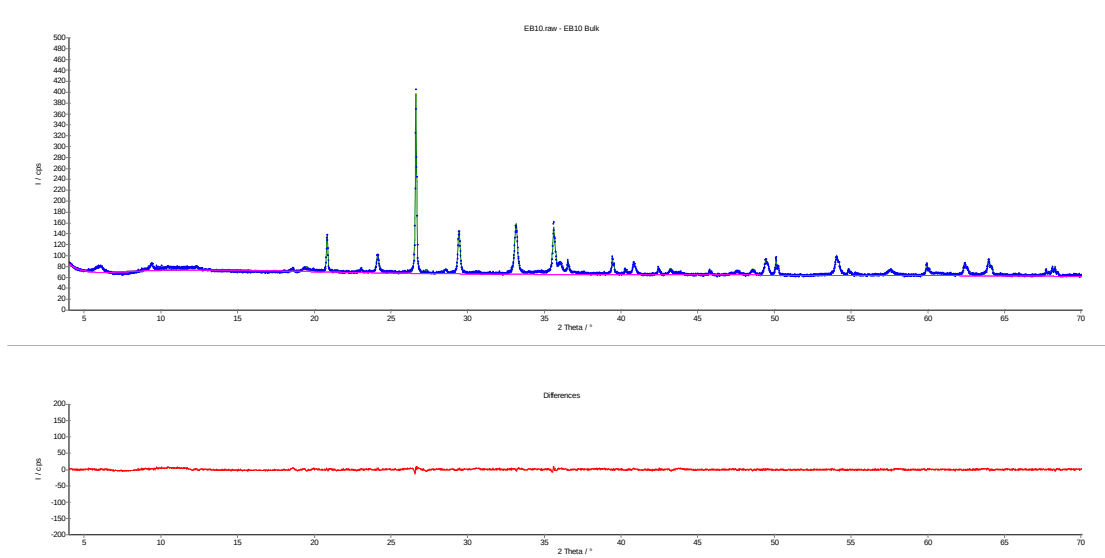
Rwp=2.65% Rexp=1.51%



EB10

Actinolite	1.71 ±0.51
Calcite	11.38 ±0.99
Chlorite	11.27 ±1.44
Chromite Mg	3.18 ±0.66
Hematite	30.96 ±1.02
Lizardite	1.02 ±0.39
Quartz	28.01 ±0.84
Smectite	1.55 ±0.54
Talc	10.93 ±1.11

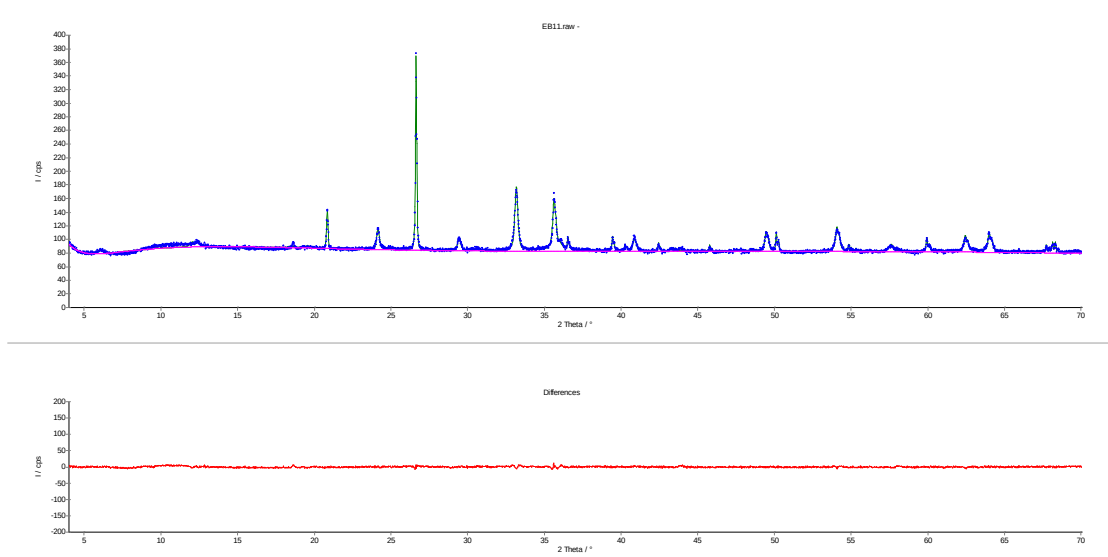
Rwp=2.39% Rexp=1.48%



EB11

Calcite	4.81 ±1.62
Chlorite	9.67 ±1.56
Chromite Mg	4.77 ±0.81
Hematite	46.46 ±1.47
Lizardite	0.66 ±0.51
Magnetite	1.08 ±0.87
Quartz	31.85 ±1.02
Smectite	0.70 ±0.72

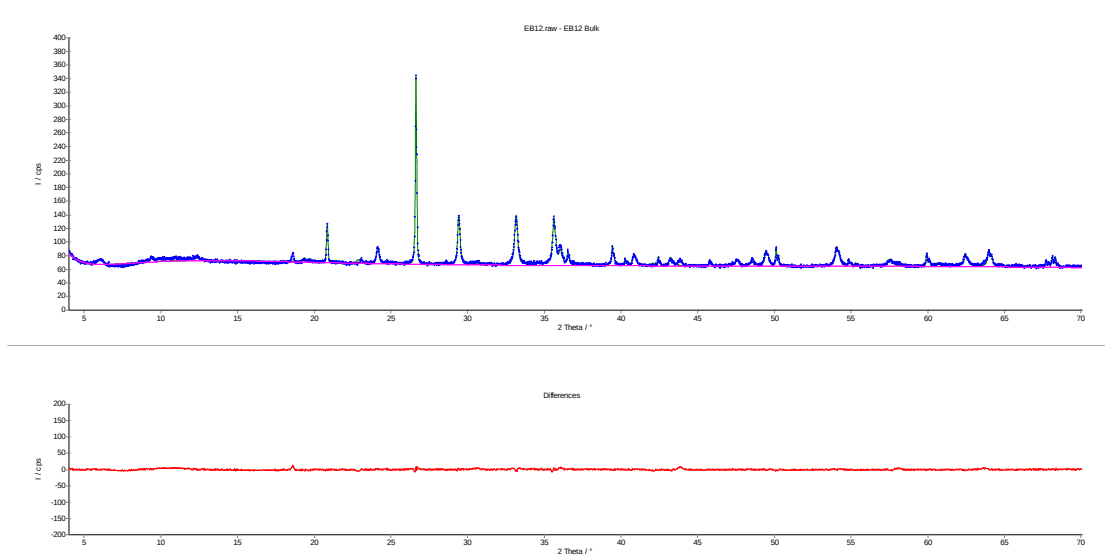
Rwp=2.00% Rexp=1.33%



EB12

Calcite	14.97	±1.20
Chlorite	8.25	±1.26
Chromite Mg	7.16	±0.75
Hematite	32.38	±1.20
Lizardite	2.84	±1.11
Magnetite	1.59	±0.87
Quartz	29.39	±0.87
Smectite	0.97	±0.66
Talc	2.45	±0.66

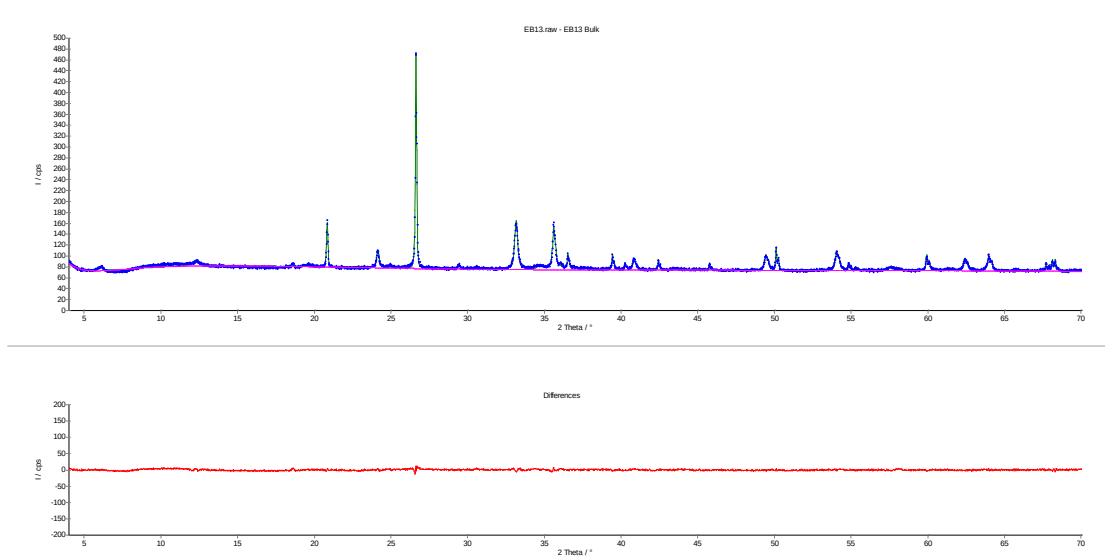
Rwp=2.32% Rexp=1.48%



EB13

Calcite	1.99 ±0.81
Chlorite	12.98 ±1.44
Chromite Mg	2.70 ±0.66
Hematite	39.14 ±1.20
Lizardite	1.26 ±1.47
Quartz	40.65 ±1.20
Smectite	1.10 ±0.81
Spinel	0.17 ±0.45

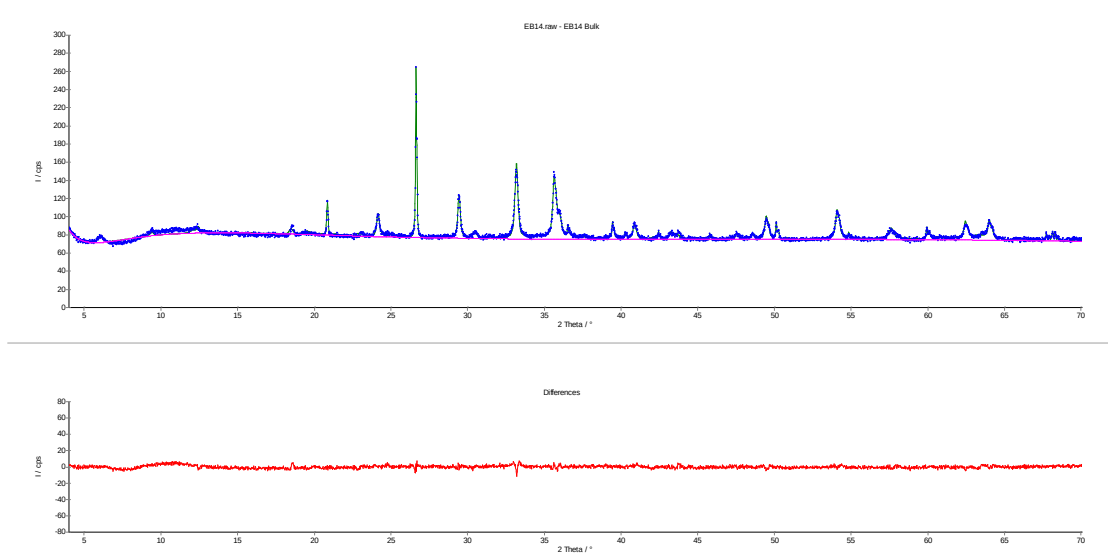
Rwp=2.25% Rexp=1.40%



EB14

Calcite	11.35 ±1.59
Chlorite	3.11 ±1.05
Chromite Mg	9.34 ±1.41
Hematite	42.30 ±1.56
Lizardite	4.83 ±1.35
Quartz	20.91 ±0.84
Smectite	1.46 ±0.63
Talc	6.70 ±1.59

Rwp=2.22% Rexp=1.39%



EB15

Calcite 3.65 ±0.72

Chlorite 10.28 ±1.71

Chromite Mg 7.71 ±0.69

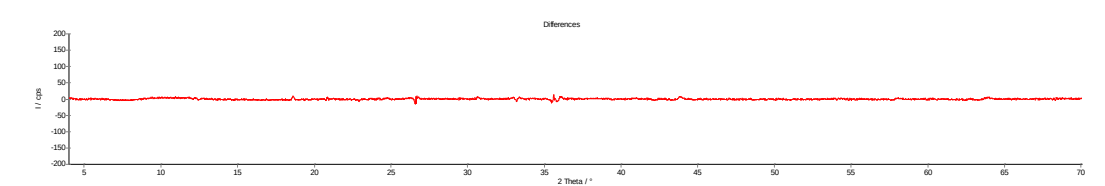
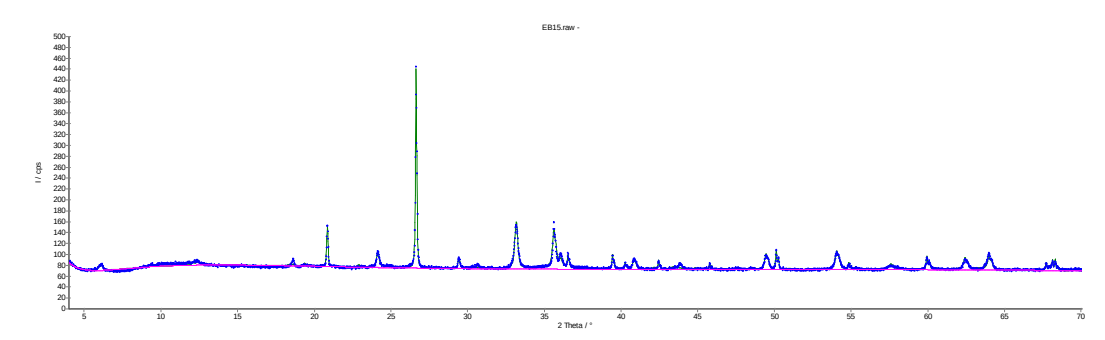
Hematite 37.52 ±1.14

Lizardite 3.16 ±1.14

Quartz 36.75 ±1.11

Smectite 0.94 ±0.48

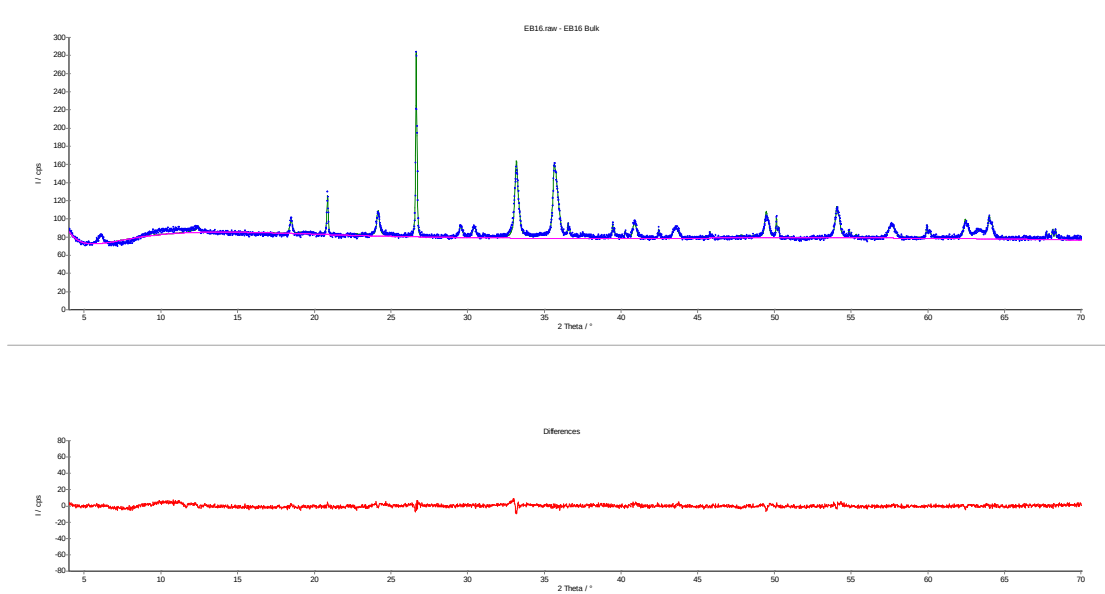
Rwp=2.23% Rexp=1.42%



EB16

Calcite	4.92 ±1.11
Chlorite	7.98 ±1.65
Chromite Mg	16.57 ±1.29
Hematite	44.43 ±1.59
Lizardite	3.26 ±1.35
Quartz	21.81 ±0.78
Smectite	1.02 ±0.63

Rwp=2.24% Rexp=1.36%



EB17

Chlorite 9.43 ±2.01

Chromite 0.87 ±0.45

Hematite 47.01 ±1.62

Lizardite 0.84 ±2.10

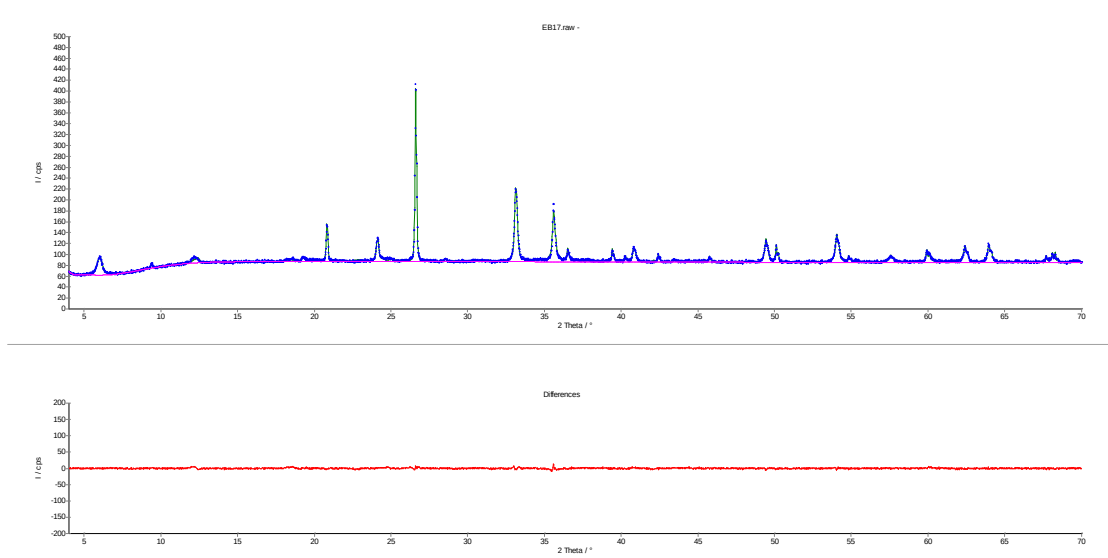
Quartz 32.88 ±1.23

Smectite 4.53 ±0.63

Spinel 0.19 ±0.81

Talc 4.26 ±1.29

Rwp=2.02% Rexp=1.34%



EB18A

Calcite 4.17 ±0.96

Chlorite 13.95 ±1.92

Chromite Mg 2.47 ±1.14

Hematite 42.28 ±1.32

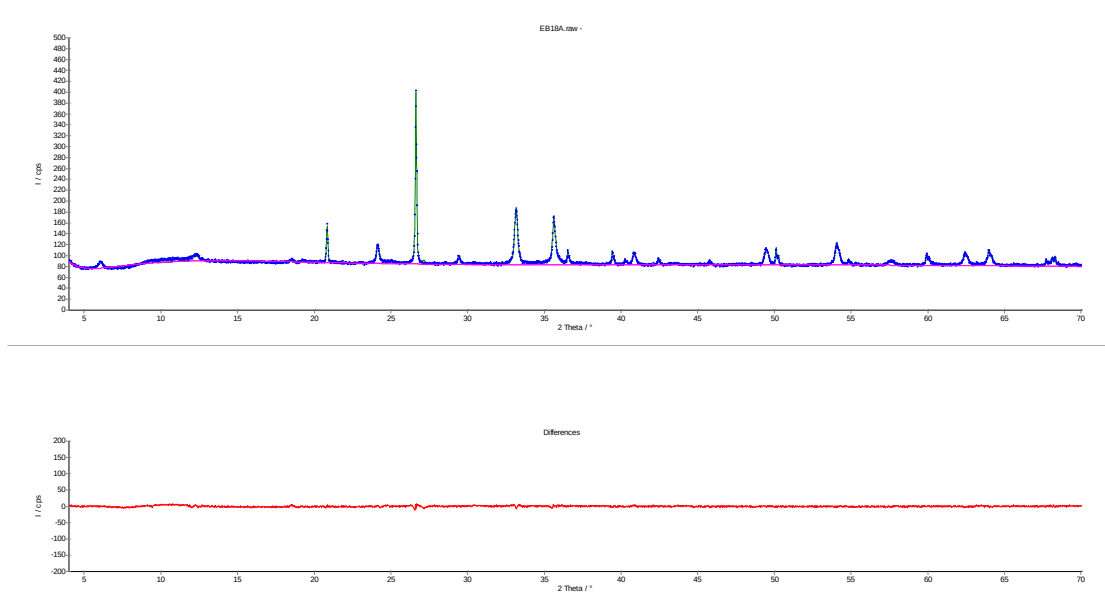
Lizardite 3.98 ±1.17

Quartz 31.82 ±0.99

Smectite 0.83 ±0.45

Spinel 0.50 ±0.78

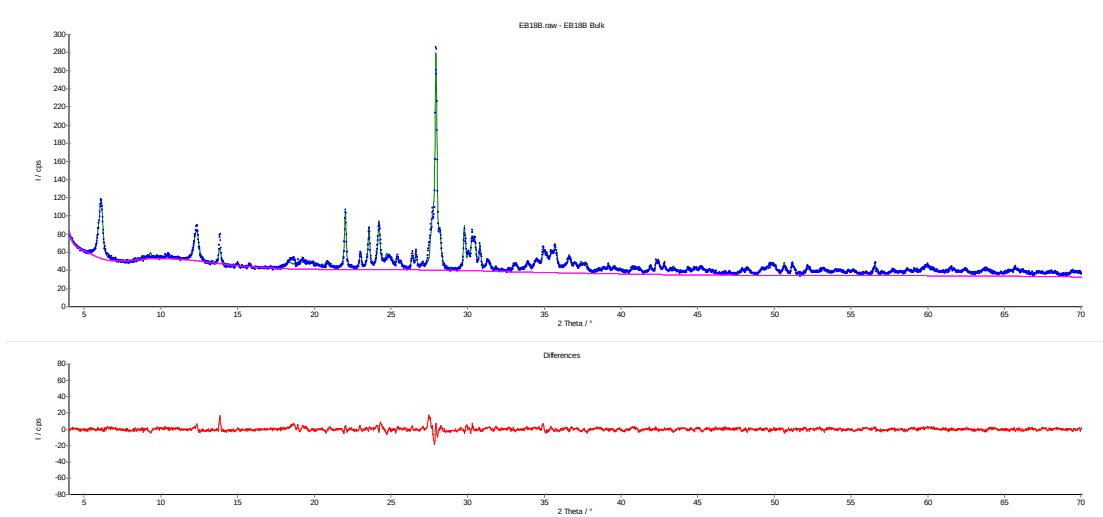
Rwp=2.07% Rexp=1.33%



EB18B

Actinolite	3.80	±0.48
Microcline	6.32	±0.81
Albite	24.76	±1.92
Andesine	8.17	±1.65
Oligoclase	10.75	±2.1
Quartz	0.67	±0.20
Smectite	4.90	±0.33
Titanite	2.96	±0.84
Aegirine	1.52	±0.63
Chlorite	5.34	±1.53
Chlorite2bdis	11.02	±1.32
Chromite	0.13	±0.14
Diopside	9.77	±0.81
Enstatite	0.13	±0.84
Enstatite(Fe)	1.98	±0.69
Hematite	1.28	±0.26
Kaolinite	0.57	±0.29
Lizardite	0.75	±0.99
Mg-chromite	1.13	±0.42

Rwp=3.25% Rexp=1.81%



EB-19

Chlorite 18.11 ±2.55

Chromite 1.83 ±2.01

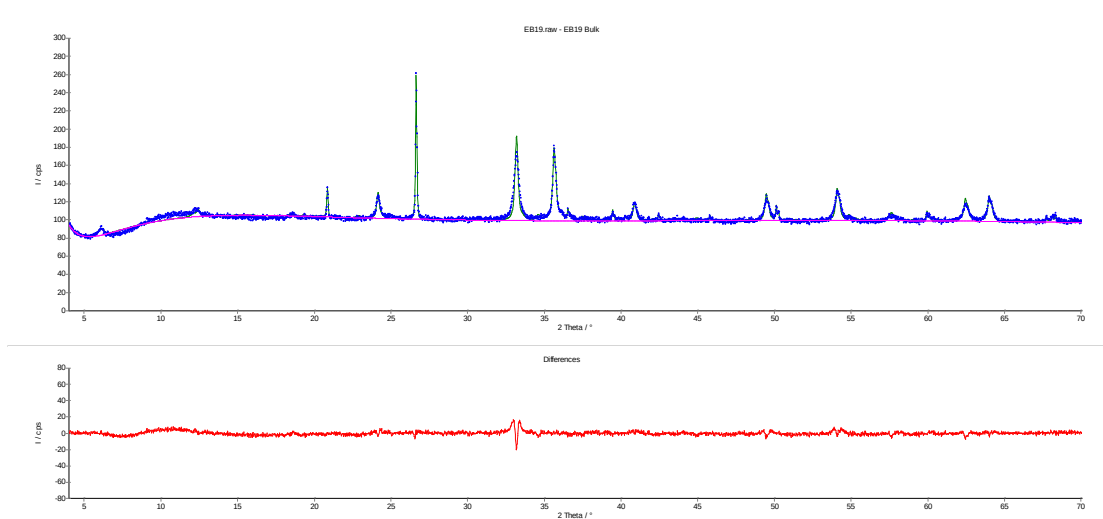
Hematite 50.58 ±2.04

Lizardite 5.86 ±1.77

Quartz 20.70 ±0.96

Smectite 1.17 ±0.60

Rwp=2.20% Rexp=1.23%



EB20

Chlorite 4.60 ±2.07

Chromite 0.89 ±0.45

Hematite 55.09 ±1.56

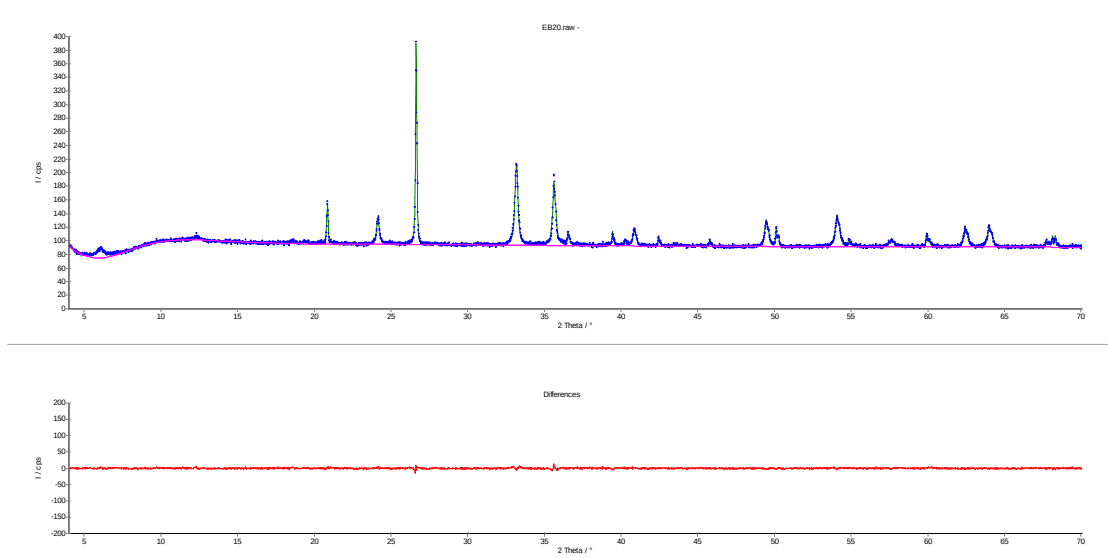
Lizardite 4.14 ±1.14

Quartz 34.14 ±1.14

Smectite 0.90 ±0.51

Spinel 0.24 ±0.87

Rwp=1.95% Rexp=1.28%



EB21

Calcite 1.62 ±0.66

Chlorite 4.50 ±0.99

Chromite Mg 3.19 ±0.93

Hematite 43.35 ±1.23

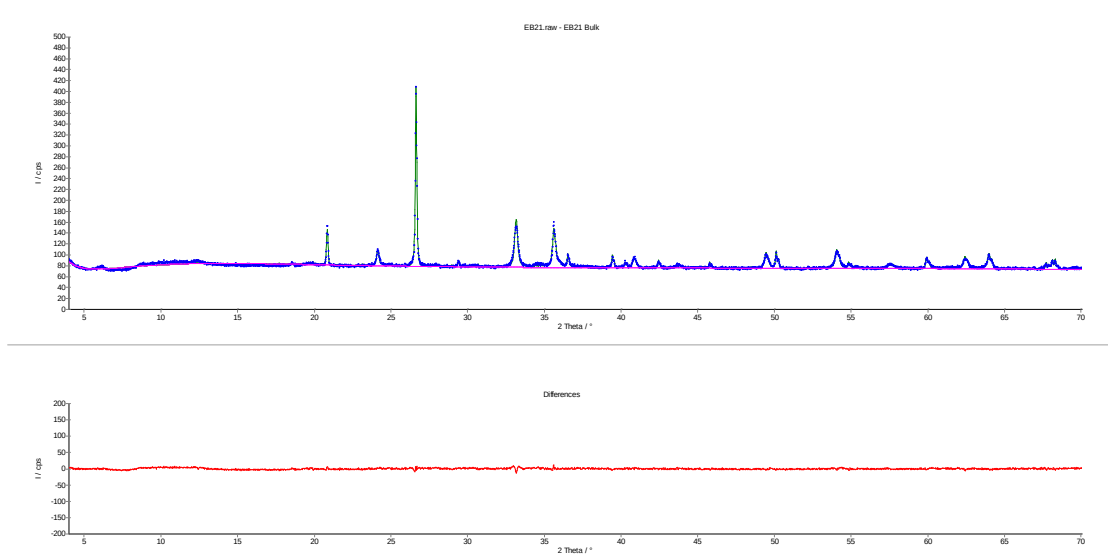
Illite 4.06 ±1.23

Quartz 41.85 ±1.23

Smectite 1.05 ±0.84

Spinel 0.37 ±0.51

Rwp=2.50% Rexp=1.39%



EB22

Calcite 1.58 ±0.75

Chlorite 5.68 ±2.61

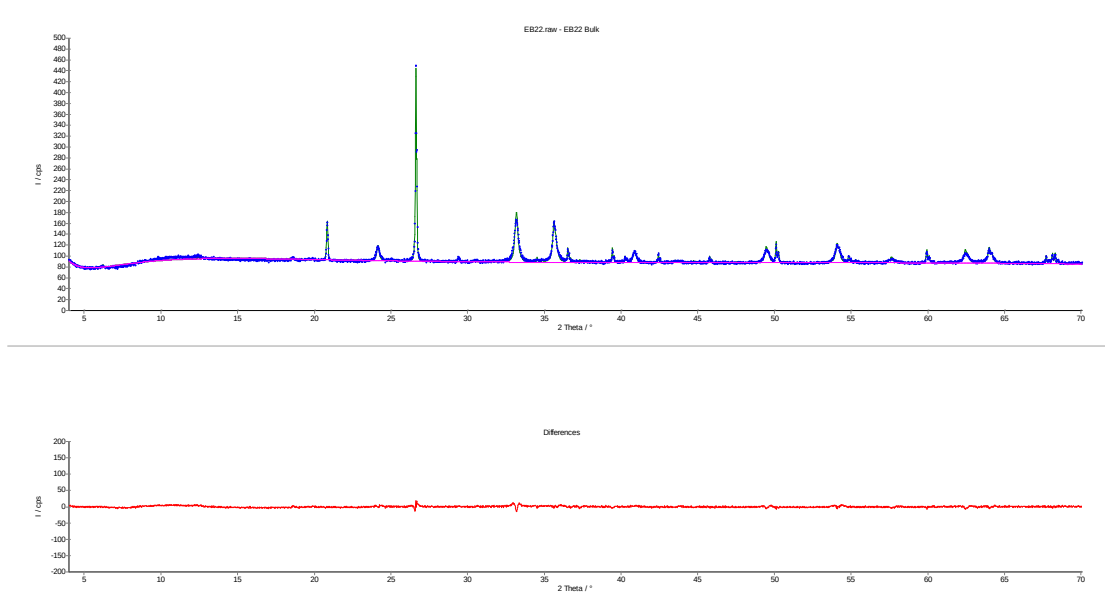
Chromite Mg 5.22 ±1.47

Hematite 48.01 ±1.89

Quartz 39.51 ±1.56

Smectite 0.00 0.00

Rwp=2.26% Rexp=1.30%



EB23

Chlorite 11.83 ±1.53

Chromite Mg 1.42 ±0.75

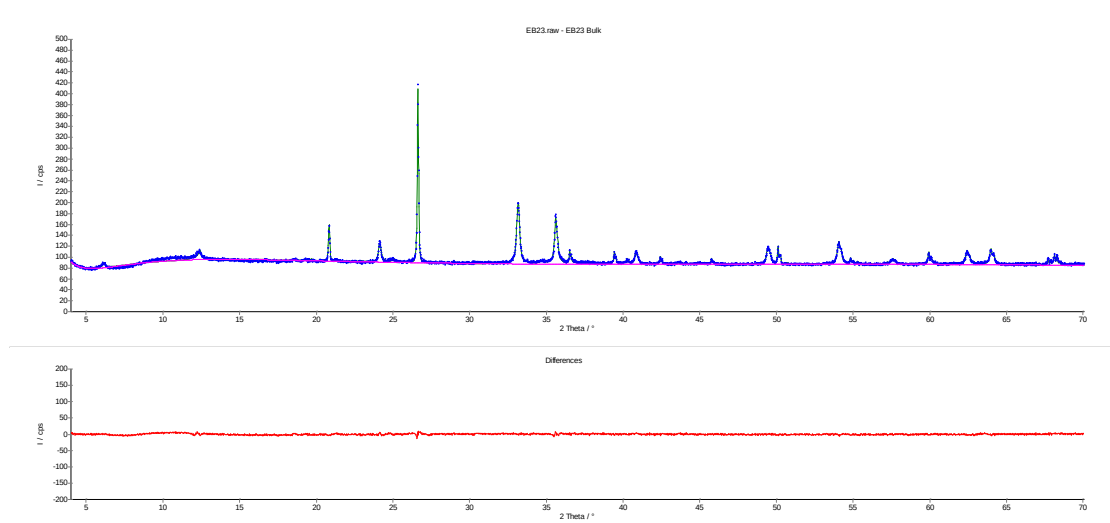
Hematite 46.65 ±1.77

Ilmenite 1.44 ±1.35

Lizardite 4.02 ±1.26

Quartz 34.63 ±1.02

Rwp=2.07% Rexp=1.31%



EB24

Chlorite 10.10 ±1.92

Chromite Mg 3.90 ±1.35

Gypsum 2.01 ±0.78

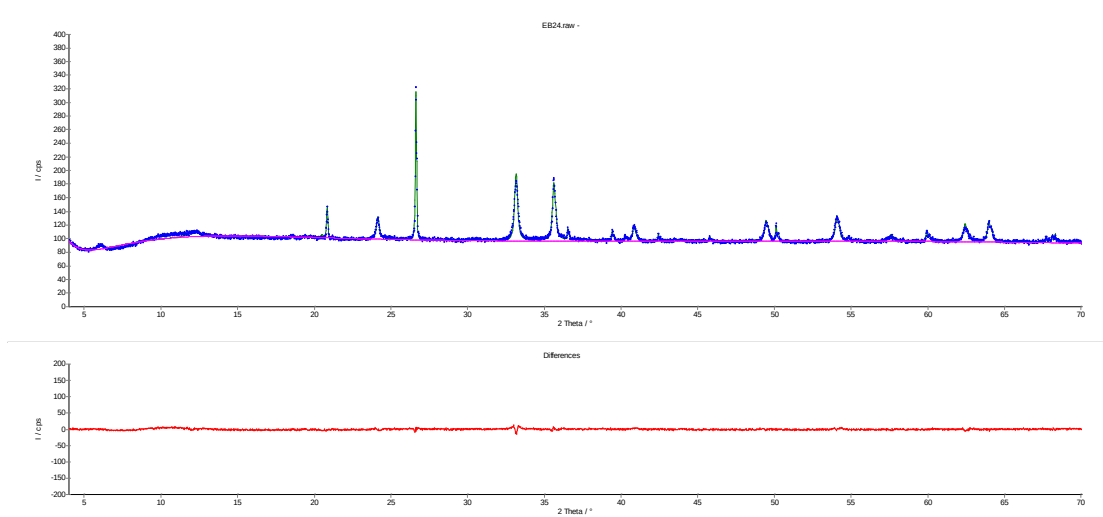
Hematite 53.11 ±1.92

Lizardite 4.67 ±1.68

Quartz 25.58 ±0.99

Smectite 0.63 ±0.48

Rwp=2.06% Rexp=1.24%



EB25

Chlorite 10.83 ±2.01

Chromite Mg 3.65 ±1.17

Hematite 55.47 ±1.74

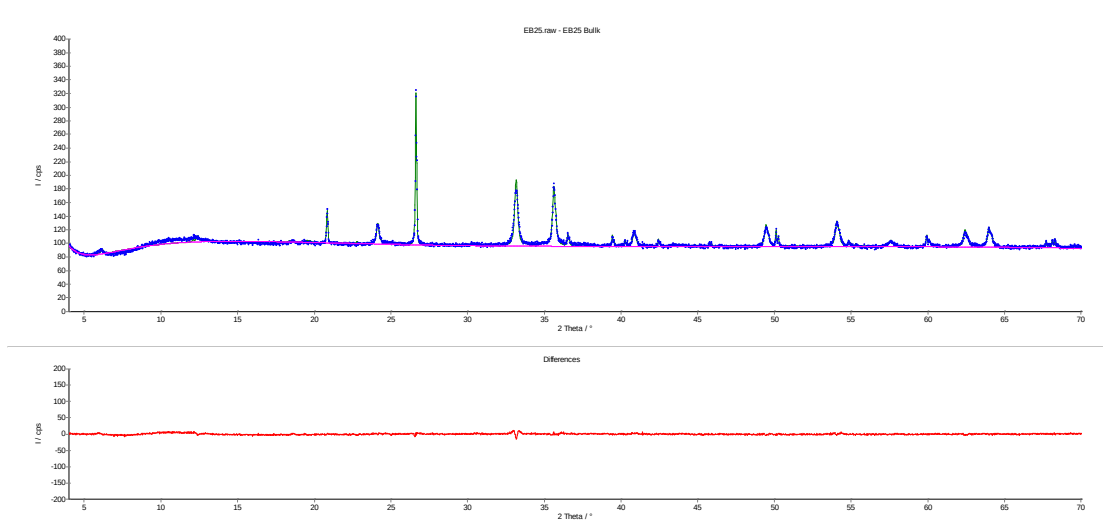
Ilmenite 0.29 ±0.45

Lizardite 1.35 ±0.75

Quartz 27.73 ±1.02

Smectite 0.68 ±0.60

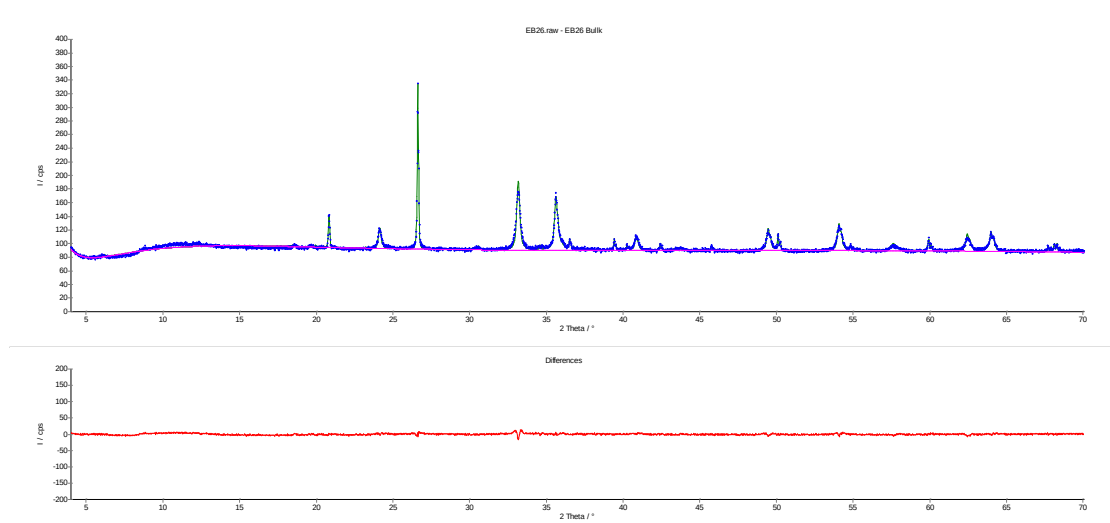
Rwp=2.11% Rexp=1.25%



EB26

Chlorite	3.42	±1.14
Chromite Mg	7.07	±2.04
Hematite	56.43	±1.86
Illite	3.09	±1.53
Quartz	29.80	±1.20
Smectite	0.20	±0.30

Rwp=2.25% Rexp=1.29%



EB27A

Chlorite	20.43	±1.83
Chromite Mg	1.58	±1.08
Gypsum	2.07	±0.54
Hematite	0.82	±0.42
Illite	1.70	±0.66
Kaolinite	5.71	±1.95
Lizardite	3.06	±0.84
Marcasite	3.76	±0.63
Melanterite	10.04	±2.25

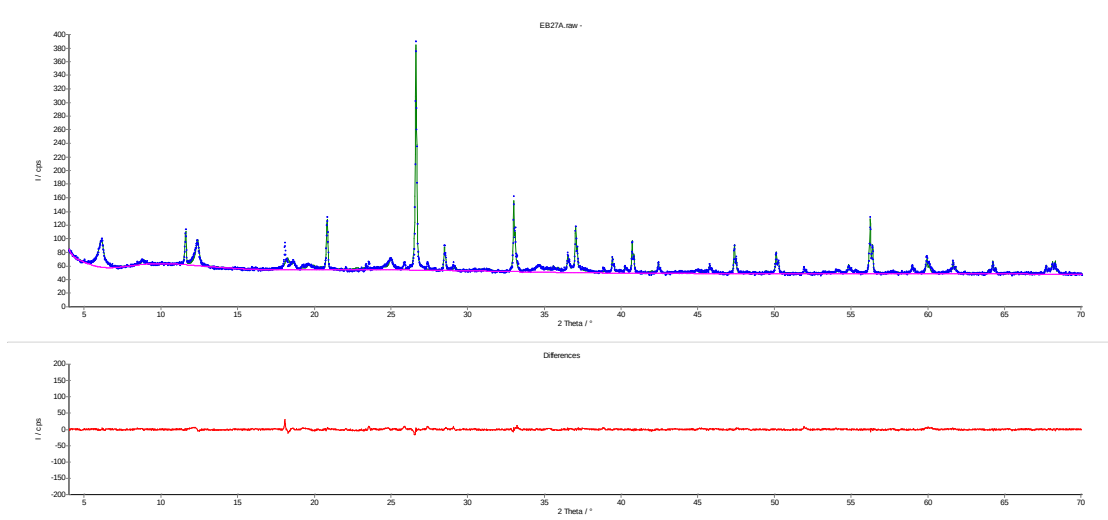
Pyrite 15.52 ±0.87

Quartz 28.68 ±1.17

Smectite 6.50 ±0.81

Sphalerite 0.12 ±0.23

Rwp=2.87% Rexp=1.66%



EB27B

Calcite 1.43 ±0.42

Chlorite 4.52 ±1.38

Clinochlore 15.82 ±2.37

Chromite 1.84 ±0.66

Gibbsite 3.01 ±0.87

Gypsum 1.06 ±0.51

Hematite 14.71 ±1.05

Illite 19.67 ±1.08

Pyrite 2.04 ±0.45

Quartz 24.68 ±0.99

Talc 3.77 ±1.11

Titanite 6.79 ± 1.32

Zircon 0.64 ± 0.39

Rwp=3.03% Rexp=1.60%

